博士論文

Observation of ^{7}Be Solar Neutrinos with KamLAND

(カムランドでの ^{7}Be 太陽ニュートリノ観測)

竹本康浩

平成 25 年

Doctoral Dissertation

Observation of ^{7}Be Solar Neutrinos with KamLAND

by

Takemoto Yasuhiro

in

Physics

in

Graduate School of Science,
Tohoku University

2014

Abstract

This dissertation reports the study of direct measurement of the ^{7}Be solar neutrinos with KamLAND based on the data from 165.4 kton-days exposure or 615.9 days livetime out of the period from April 2009 to June 2011, which was taken with the extremely low background liquid scintillator, specially-purified for this observation.

The event rate of ^{7}Be solar neutrinos measured is [582.2 ± 77.4 (stat.) ± 42.5 (syst.)] and [581.8 ± 72.1 (stat.) ± 53.5 (syst.)] events/kton-days for SFII-SSM-AGSS09 and SFII-SSM-GS98 based energy spectra respectively. The translated flux of ^{7}Be neutrinos under the consideration of 3-generation MSW-LMA neutrino oscillation is (5.83 ± 0.89) and (5.82 ± 0.90) $\times 10^9$ cm^{-2}s^{-1} respectively, and the hypothesis of the null contribution of the ^{7}Be solar neutrinos is rejected at 8.2σ C.L. This result is consistent to the predicted fluxes of SFII-SSM-AGSS09 and SFII-SSM-GS98, (4.56 ± 0.32) and (5.00 ± 0.35) $\times 10^9$ cm^{-2}s^{-1}. It also confirms the previous direct measurement of the Borexino experiment, $(4.75\ ^{+0.26}_{-0.22})\ \times 10^9$ cm^{-2}s^{-1}.

Acknowledgment

Contents

List of Figures

List of Tables

1. Introduction

Solar neutrinos led experiments of and then discovery and precise measurements of neutrino oscillation, via observation of atmospheric neutrinos and reactor neutrinos, by declaring the solar neutrino problem, that is, flux of solar neutrinos observed at underground detectors were significantly smaller than that of solar neutrinos predicted in the standard solar model.

KamLAND, Kamioka Liquid Anti-Neutrino Detector aimed first, precise measurement of neutrino oscillation by using reactor neutrinos whose generation is known with high accuracy, and then test of the standard solar model by using highly sensitive ^{7}Be solar neutrinos owing to their smaller theoretical uncertainty and the 2nd highest flux among solar neutrinos. In 2005 and then in 2009, the standard solar model was updated with newly reported chemical abundance at the solar surface derived from newly employed modeling of solar structure. While the new modeling well reproduces structure of the solar surface, it reduces the temperature of the solar atmosphere then lower metallicity emerged. The resulting new solar model has discrepancy between Helioseismology on its internal structure. Also the resulting new solar abundances make it difficult to reproduce stella evolutionary tracks. This new solar problem is called the solar abundance problem, and ^{7}Be solar neutrinos are also expected to test this discrepancy with it's high intensity.

While neutrino oscillation property was studied and large mixing angle of neutrino oscillation and existence of matter enhanced neutrino oscillation were discovered, KamLAND collaboration started to purify its liquid scintillator, with which low energy ^{7}Be neutrinos can be observed. With two years of overwhelming works for the purification preceded by three years of research and development, background event rate at the center of the detector successfully decreased to a magnitude comparable to the theoretical magnitude of flux of ^{7}Be neutrinos. But later during the period for observation of ^{7}Be neutrinos, KamLAND faced several large convection of the liquid scintillator triggered by destabilization of thermal equilibrium of the detector, which introduced obvious ^{210}Bi background from the KamLAND balloon edge into the center of the detector.

In ^{7}Be solar neutrino analysis, the preceding studies (Keefer, 2009, Nakajima, 2009, Grant, 2011, Xu, 2011) tried to select events in high S/N region from such temporally and spatially variating background, which made mainly three problems; smaller statistics due to smaller fiducial volume, larger uncertainty due to larger fiducial volume surface, uncertain volume selection bias due to using own signal for selection. In this analysis, in order to prevent such problems from invading, a method is considered in which all data is fully utilized inside a certain radius from the KamLAND center regardless of its S/N ratio, at the same time, ability of determination of ^{7}Be solar neutrinos in high S/N ratio region is fully emphasized. The method is summarized as follows,

   1. Making time-space slices from exposure of all observation period and the fiducial

volume

2. Classifying all the slices into several ranks by event rate of neighboring slices inside target energy range

3. Executing simultaneous spectral fit against all data spectra out of all ranks for determination of event rate of ^{7}Be solar neutrinos.

Although the most important background against ^{7}Be solar neutrino is ^{210}Bi, the shape of the beta decay of ^{210}Bi is not accurate since ^{210}Bi decays in forbidden beta decay. Thus the shape factor of ^{210}Bi is defined and calibrated by KamLAND data simultaneously in the fit.

In this thesis, the physical background including neutrinos, solar neutrinos and the standard model are described in Chapter 2. The KamLAND detector and some measured values are described in Chapter 3. Event reconstruction and selection are described in Chapter 4 and 5. Background estimation is described in Chapter 6. Analysis of ^{7}Be solar neutrinos are described in Chapter 7 and the discussed there. Finally, conclusion is summarized in Chapter 8.

2. The Standard Solar Model and Neutrinos

2.1. The Standard Solar Model

The sun is the most familiar star for us, not only due to that it is the closest to us, but also it is a main-sequence star. Hence for understanding stellar evolution, the sun is one of the best sample and on the other hand for understanding the Sun, the other stars are good population. The standard solar model, SSM is the most successful simulation model constructed for study based on the relation from observation data and theoretical models.

2.1.1. Brief Theory of Stellar Evolution

A main-sequence star, as the sun is born in a molecular could, where hydrogen could form molecules in much denser area in a interstellar could. The birth is started with the molecular cloud begins to gather with losing balance between pressure and gravity. The core region starts to getting higher temperature with emission of the kinetic energy of absorbed interstellar materials and of the potential energy with gravitational contraction of the core region itself. With increase of the temperature in the core, hydrogen molecules separate to atoms at around 2×10^3 K, then the atoms ionize and form plasma of hydrogen nuclei and electrons at around 1×10^4 K, followed by ionization of helium at around 2×10^4 K. At this stage, the core has the same composition as usual stars. When the temperature in the core gets around 1×10^7 K, nuclear fusion of hydrogen ignites. Vast energy of fusion substitutes for the energy from gravitational contraction, then the contraction finishes. Now the star belongs to the main sequence. It has taken approximately 1 % of the period the star belongs to the main sequence, and it corresponds to 50 million years for a star having the solar mass.

While a star belongs to the main sequence, the energy emitted from the surface corresponds to the energy generated in nuclear fusion. Type of fusion and the mechanism of heat transport are different among light mass stars like the sun and heavier stars. There are two types of fusion reaction in a star, pp-chain and CNO cycle reactions and they are shown in Figure 2.1. Sensitivity of energy production to temperature of the two reactions is shown in Figure 2.2. The pp-chain is dominant at lower temperature, whose energy production rate is approximately relative to 10^4 MK (10^6 K). While the CNO cycle is dominant at higher temperature, whose energy production rate is approximately relative to 10^{20} MK.

In the core of a low mass star or in an intermediate mass star, temperature is relatively lower, where the pp-chain is favored. Due to the less sensitivity of energy production rate, the fusion reaction occurs outside the core of the star while of course it occurs the
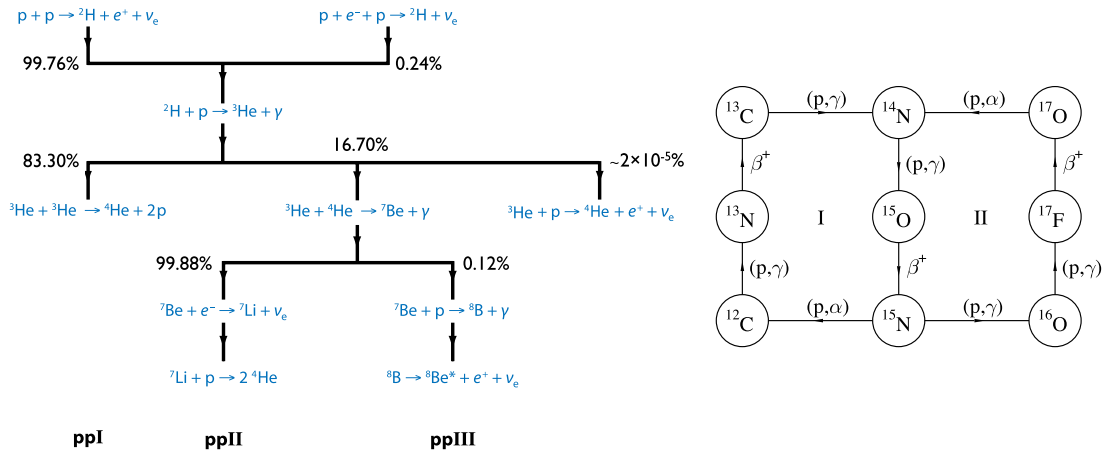
Figure 2.1.: pp-chain and CNO-cycle (Adelberger et al., 2011)
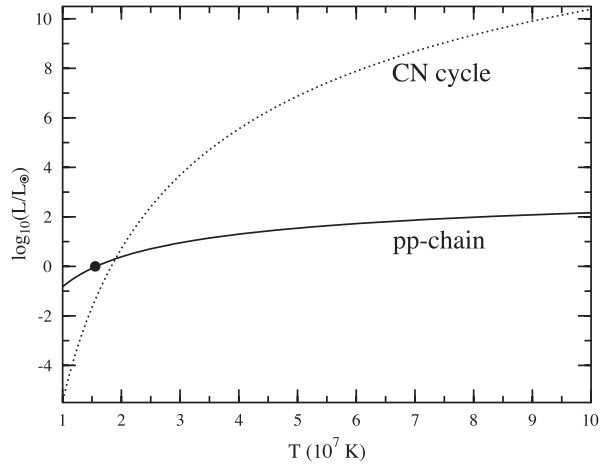
Figure 2.2.: Sensitivity of Energy Production to Temperature (Adelberger et al., 2011).

most frequent in the core. In this case, thermal gradient in the star is low, and the heat transport is mainly done by radiation. As the thermal gradient gets steeper, the more heat is transported by radiation. The transport gets also larger when the mean free path of a photon, which is related to radiative opacities of gas, is larger.

In the core of a massive star, temperature is relatively higher, thus where the CNO cycle is favored. For this case, due to the higher sensitivity of CNO cycle, energy production rate outside the very center of the core quickly reduced, and the thermal gradient gets much steeper. Since the resulting gradient is larger than adiabatic temperature gradient, radiation gets insufficient for thermal transport, instead, convection of clusters of gas with different temperature dominates. This change is Schwarzschild Criterion.

The difference of fusion gradually changes the life of a star.

In a lower mass star, when hydrogen is exhausted at the center of its core, there remains helium core while hydrogen continues to fusion in the outer shell. In this stage, called hydrogen shell burning, the core gets larger, heavier, and hotter then helium starts to burn in the core. Due to the increase of fusion reaction rate, the star expands then it leaves main-sequence and called a giant. Once helium finishes burning, the inner region starts to shrink then as a pulsating star, it evolves the outer region and forms planetary nebula then ends up a white dwarf.

In a larger mass star, hydrogen is exhausted in its core simultaneously due to the convection. Then the remaining helium core starts gravitational contraction. Later the heat re-ignite the hydrogen burning as well as helium burning. After burning heavier metal as carbon, oxygen and etc, iron core is remained. Finally it undergoes an supernova explosion then ends up a neutron star or a black hole.

Such lives of stars or stellar evolution is obvious in a H-R diagram as shown in Figure 2.3. Stellar evolution theory and astronomical observation always corporates such diagrams. The sun is a nominal low mass star and a good model for constructing and validating the evolution theory.
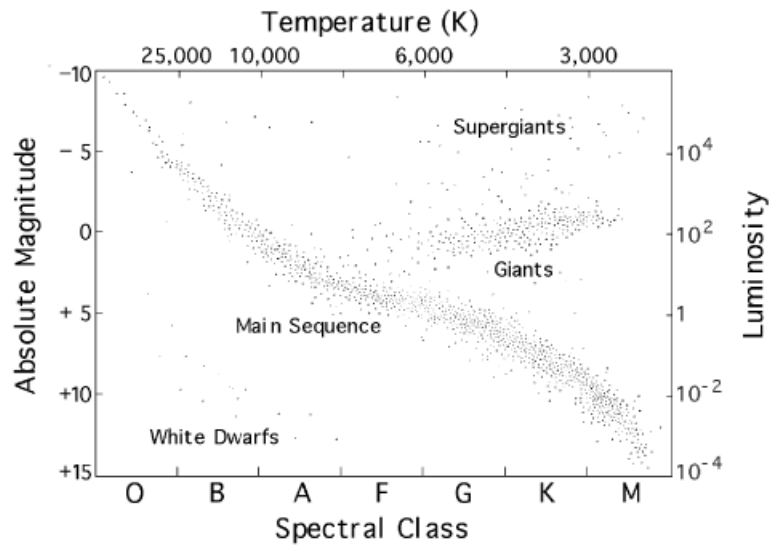
Figure 2.3.: Example HR diagram (NASA). The x axis is effective temperature or spectral type and the y axis is absolute magnitude or luminosity. For about the spectral type, O roughly corresponds to blue, A white, G yellow and M red. Main sequence stars forms band structure from the bottom right to the top left. Darker and colder stars, whose luminosity and temperature are smaller than 2.5 and 8×10^3 K respectively are roughy low mass stars burning pp-chain reaction. They end up white dwarfs via giants.
The sun has its luminosity 1 and temperature 6×10^3 K and a nominal low mass star.

2.1.2. Standard Solar Model

Standard Solar Model (SSM) is the most successful simulation of solar models. It begins with a model assuming the sun in pre-main-sequence, then develops the model by calculating with the following 5 equations and 4 boundary conditions based on the stellar evolution theory, and finally limits the model by the observed values of the current sun.

At first, it is assumed the sun has homogenous abundance distribution when it is born. Then equations of state of the sun at a certain time are as follows (Basu and Antia, 2008),

$$\text{Conservation of Mass} \qquad \frac{dm(r)}{dr} = 4\pi r^2 \rho(r) \qquad (2.1)$$

$$\text{Hydrostatic Equilibrium} \qquad \frac{dP(r)}{dr} = -\frac{Gm(r)\rho(r)}{r^2} \qquad (2.2)$$

$$\text{Conservation of Energy} \qquad \frac{dL(r)}{dm} = \epsilon_{\text{nuclear}} - \epsilon_\nu - \epsilon_{\text{g}} \qquad (2.3)$$

$$\text{Energy Transport} \qquad \frac{dT}{dm} = -\frac{GmT}{4\pi r^4}\nabla \qquad (2.4)$$

$$\text{Abundance Time Evolution} \qquad \frac{dX_i}{dt} = -\frac{m_i}{\rho}\left[\sum_j r_{ji} - \sum_k r_{ik}\right] \qquad (2.5)$$

In (2.1), $m(r)$ and $\rho(r)$ is the mass and density in side a sphere of radius respectively. While radius r does vary according to the evolution of the sun, the sun does not loose $m(r)$ more than 0.01 % during main-sequence. Thus $m(r)$ is usually treated as an independent variable as

$$\frac{dr}{dm} = \frac{1}{4\pi r^2 \rho(r)} \qquad (2.6)$$

Then (2.2) is also re-written as

$$\frac{dP}{dm} = -\frac{Gm}{4\pi r^4}. \qquad (2.7)$$

This equation (2.2 then 2.7) shows the equilibrium between gravity and pressure and has extremely good sensitivity i.e. the sun collapse within an hour when this equation is significantly violated.

In (2.3), $L(r)$ corresponds to the energy crossing the surface of sphere of r, $\epsilon_{\text{nuclear}}$ corresponds to the energy by fusion reaction per unit mass and time, ϵ_ν corresponds to the energy taken out by neutrinos, and ϵ_{g} is the gravitational energy consumed by the expansion of the sun or released by shrink of it.

In (2.4), ∇ is dimensionless temperature gradient, which is expressed as $\nabla = d\ln T/d\ln P$. In radiative zone, where heat transport is done by radiation, ∇ is simply expressed as

$$\nabla = \nabla_{\text{rad}} = \frac{3}{64\pi\sigma G}\frac{\kappa LP}{mT^4}, \qquad (2.8)$$

where σ is the Stefan-Boltzmann constant and κ is the radiative opacity. On the other hand in convection zone, where heat transport is partially done by convection, ∇ equals to the adiabatic temperature gradient. Thus with using the specific entropy s, ∇ is give as

$$\nabla = \nabla_{\mathrm{ad}} = \left(\frac{\partial \ln T}{\partial \ln P} \right)_s .$$ (2.9)

In practical simulation, a free parameter, mixing length parameter α is used based on mixing length theory, which is one of the most common formulations for calculating convection flux, since the time scale of convection is much shorter than that of SSM grid then evaluating the result of the Navier-Stokes equation to be solved is impossible.

While the 4 equations above determine the structure in the sun, the 5th equation (2.5) determine the time evolution of abundance via fusion reaction, convection and diffusion. X_i and m_i is the mass fraction and the mass of any i-th isotope respectively and r_{ji} is the production rate of the isotope from the j-th isotope, r_{ik} is the disintegration rate of the isotope to the k-th isotope.

Practically, structure determination for a certain time is solved at first and abundance is determined next, then another structure is determined at a slightly later time and so.

The 4 boundary conditions are provided as follows,

- Radius : $r_{m=0} = 0$ (2.10)
- Luminosity : $L_{m=0} = 0$ (2.11)

- Pressure : $P_{\mathrm{surface}} = \frac{G m_\odot}{r_s^2} \int_0^{\tau'} \frac{1}{\kappa} dr$ (2.12)

- Temperature : $T^4{}_{\mathrm{surface}} = \frac{L_{\mathrm{surface}}}{4\pi\sigma r^2{}_{\mathrm{surface}}} (3\tau/4 + 1/2)$ (2.13)

The first two conditions are trivial. A simulation at each specified time starts from the surface, then is bounded by the center. The other two conditions on surface are rather complicated. τ is the optical depth defined as

$$\tau(r) = \int_r^\infty \kappa \rho dr',$$ (2.14)

and the surface is defined as $\tau(r_{\mathrm{surface}}) = 2/3$, where the temperature equals the effective temperature. These 2 are given with approximation $m_{\mathrm{surface}} = m_\odot$, $L_{\mathrm{surface}} = L_\odot$ and $r_{\mathrm{surface}} = r_\odot$ and assumption $P(\tau = 0) = 0$.

The are additionally 3 constraints from observation, solar radius $R_\odot$, solar luminosity $L_\odot$ and surface metallicity ratio $(Z/X)_\odot$, while initial amount of helium and metallicity, Y_{INI} and Z_{INI} are freely floated.

Fusion Chain Reaction and Solar Neutrinos

As described in the previous sections, the two types of fusion chain reaction, pp-chain and CNO-cycle occur in the core of the sun. The diagram of the reaction is shown in

Figure 2.1. Overall reaction of the either of the chain reaction is represented as

$$4p \rightarrow {}^4\text{He} + 2e^+ + 2\nu_e + 26.73 \text{ MeV}, \tag{2.15}$$

and produced neutrinos are called the solar neutrinos and they take out the energy of them out from the sun due to their extremely small cross section. The types of solar neutrinos and the energy are summarized in Table 2.1.

Table 2.1.: Solar Neutrino Production Reaction and Energy

ν	Reaction		Max Energy MeV	Mean Energy MeV
pp	$p + p$	$\rightarrow {}^2\text{H} + e^+ + \nu_e$	0.420	0.265
pep	$p + e^- + p$	$\rightarrow {}^2\text{H} + \nu_e$	1.442	-
${}^7\text{Be}$	${}^7\text{Be} + e^-$	$\rightarrow {}^7\text{Li} + \nu_e$	0.862	-
	${}^7\text{Be} + e^-$	$\rightarrow {}^7\text{Li}^* + \nu_e$	0.384	-
${}^8\text{B}$	${}^8\text{B}$	$\rightarrow {}^8\text{Be}^* + e^+ + \nu_e$	14.02	6.710
hep	${}^3\text{He} + p$	$\rightarrow {}^4\text{He} + e^+ + \nu_e$	18.77	9.62
${}^{13}\text{N}$	${}^{13}\text{N}$	$\rightarrow {}^{13}\text{C} + e^+ + \nu_e$	1.199	0.707
${}^{15}\text{O}$	${}^{15}\text{O}$	$\rightarrow {}^{15}\text{N} + e^+ + \nu_e$	1.732	0.997
${}^{17}\text{F}$	${}^{17}\text{F}$	$\rightarrow {}^{17}\text{O} + e^+ + \nu_e$	1.740	0.999

pp-chain reaction starts with the fusion of two protons into a deuterium via β^+ decay of an intermediate diproton. The flux of neutrinos released from this reaction, pp neutrinos, is the largest among solar neutrinos, since pp-chain is dominant in the sun and since most of pp-chain starts from this reaction. pp neutrinos have continuous energy spectrum since the final state of the reaction is three-body system.

Another initiation reaction of pp-chain is much minor, and is the fusion of two protons with one electron capture resulting a deuterium and a neutrino, a pep neutrino. Since the final state of this reaction is two-body system, neutrino energy is monochromatic. In comparison to the reaction for pp neutrinos, the energy is 2×0.511 MeV larger than the maximum energy of pp neutrinos.

Above two reactions are followed by the fusion reaction of ${}^3\text{He}$ generation from a deuterium and a proton.

pp-chain diverges into 4 branch fusion reactions afterwards. The reaction with the largest fraction, 83.3 % is the ppI branch and it does not generate a neutrino.

The second largest branch, and the largest of the rest three, ppII branch holds 16.7 %, where a ${}^7\text{Be}$ neutrino is generated from the electron capture reaction by ${}^7\text{Be}$. According to the different final state of electron capture of ${}^7\text{Be}$, that is the excited and ground state of ${}^7\text{Li}$, ${}^7\text{Be}$ neutrinos have two monochromatic energy.

ppIII, which has the third highest branch, 0.02 %, emits ${}^8\text{B}$ neutrinos from β decay of ${}^8\text{B}$. This neutrino has yet small flux, has much higher energy and is easier for observation, while the uncertainty is relatively higher since the final state, the excited state of ${}^8\text{Be}$ is unstable and thus the maximum energy varies.

The smallest branch ppIV has only 2×10^{-5} % and is not suitable for observation, although this branch emits the highest energy from the reaction with a ^{3}He and a proton.

As described in the precious section, CNO-cycle is much more sensitive to temperature. CNO-cycle I is activated at around 1.3×10^7 K and CNO-cycle II is activated at around 1.6×10^7 K. Energy generation rate of CNO-cycle exceeds that of pp-chain at around 2×10^7 K. In the core of the sun, where the temperature is 1.57×10^7 K, CNO-cycle is subdominant and energy generation fraction is only few %. In the cycle, the total number of C, N, O and F does not change and they pretends as catalysts. When CNO-cycle is steadily processed, ^{14} gradually increases due to the different of rotation direction of CNO-cycle I and II and due to its slowest reaction speed.

Other chain reactions such as triple alpha, CNO-cycle III, VI and Hot CNO-cycles are negligible in the core of the sun.

SFII-SSM

In the analysis of this thesis, the latest SSM, so called SFII-SSM (Serenelli et al., 2011) is employed. The main feature of the latest update from the previous SSM, BPS09 (Serenelli et al., 2009) is the replacement of the recommended values of the nuclear reaction rates in SFII (Adelberger et al., 2011), which is the first systematic evaluation of hydrogen burning reaction since SFI (Adelberger et al., 1998) and NACRE (Angulo et al., 1999).

The input quantities are summarized as follows,

- Age$_\odot$: 4.57×10^9 yr
- Luminosity$_\odot$: 3.8418×10^{33} erg s^{-1}
- Radius$_\odot$: 6.9598×10^{10} cm
- Chemical Composition$_\odot$: Summarized in (Serenelli et al., 2009:Table 1)
                                       $(Z/X)_{\text{Surface}} = 0.229$ (GS98) and 0.0178 (AGSS09)
- S Factor   : SFII in (Adelberger et al., 2011:Table I)
- Radiative Opacity   : Opacity Project (Badnell et al., 2005)

The SSM is simulated with using the two independent and controversial surface abundance analysis GS98 (Grevesse and Sauval, 1998) and AGSS09 (Asplund et al., 2009). The problem emerged with using the AGSS09 is described in the next section.

Detail data calculated in SFII-SSM is presented in (Serenelli, 2013). Radius distribution of temperature, electron density, mass fraction and neutrino production are given there and shown in Figure 2.4. The electron density distribution and the neutrino production density are essential information for generating theoretical neutrino energy spectrum. The calculation of the generation is described in the later section.

Is also gives total neutrino flux for each solar neutrino for each abundance as in Table 2.2. Since AGSS09 yields lower metallicity, metal related neutrinos, ^{7}Be, ^{8}B, ^{13}N, ^{15}O and ^{17}F solar neutrinos significantly reduce, while non-metal neutrinos, pp, pep, hep solar neutrinos increase in order to compensate the reduction. All the metal neutrinos
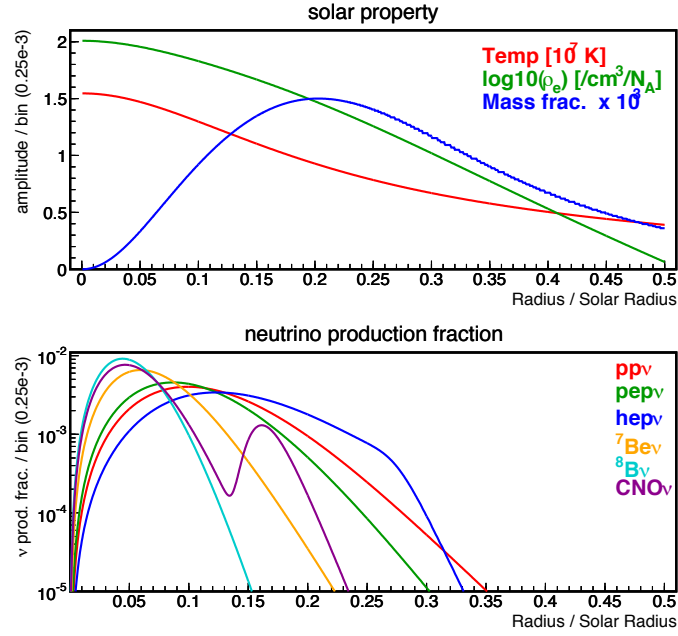
Figure 2.4.: Solar properties and neutrino production

have enough different fluxes among the abundances compared to the uncertainties of the fluxes themselves. And ^{7}Be solar neutrinos hold the largest flux, which is suitable for the observation of the difference among the abundances.

Table 2.2.: Solar Neutrino Fluxes in SFII-SSM in $1/cm^2/s$

ν	GS98	AGSS09	(O)	Diff [%]
pp	5.98 ($\pm$ 0.6 %)	6.03 ($\pm$ 0.6 %)	10	+0.8
pep	1.44 ($\pm$ 1.2 %)	1.47 ($\pm$ 1.2 %)	8	+2.1
hep	8.04 ($\pm$ 30 %)	8.31 ($\pm$ 30 %)	3	+3.4
^{7}Be	5.00 ($\pm$ 7 %)	4.56 ($\pm$ 7 %)	9	-8.8
^{8}B	5.58 ($\pm$ 14 %)	4.59 ($\pm$ 14 %)	6	-18
^{13}N	2.96 ($\pm$ 14 %)	2.17 ($\pm$ 14 %)	8	-27
^{15}O	2.23 ($\pm$ 15 %)	1.56 ($\pm$ 15 %)	8	-30
^{17}F	5.52 ($\pm$ 17 %)	3.40 ($\pm$ 16 %)	6	-38

2.1.3. The New Solar Problem

Chemical Composition

As mentioned in the previous section, the chemical composition of the solar surface is an input parameter and thus a constraining parameter for SSM simulation. Although

mass spectroscopy of meteorites directly and precisely measures the abundance ratio, it is not suitable for reproducing the primordial solar system abundances since the volatile elements are depleted. The ratio of H, He, C, O and N are essential for production of SSM, but they are all volatile and thus we need to rely on the solar photospheric abundance. There have been very widely used solar photospheric abundance profile GS98, which was reported in 1998. The same authors updated the abundance with applying 'better' modeling of the solar atmosphere and reported AGSS09 profile in 2009. The main features introduced for the modeling are as follows,

- 3D and time-dependent hydrodynamical model of the solar atmosphere
- variation from local thermodynamic equilibrium, non-LTE.

The result of introducing such features is remarkable. Figure 2.5 shows a spectral line profile of a typical FeI line, where 3D model shows perfect reproducibility. Figure 2.6
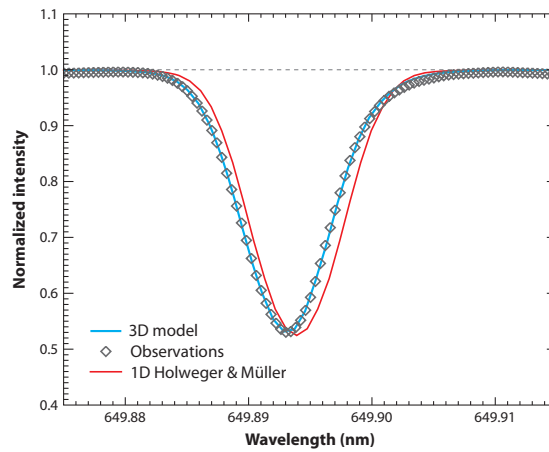
Figure 2.5.: Reproduction of Spectral Line of a typical FeI line. The spectral line profile of 3D model perfectly reproduces that of observation, which was unable with 1D model.

also shows the great reproducibility of the solar surface structure, granule.

While the new model shows remarkable reproducibility, several elements are evaluated significantly differently from the previous abundance, GS98, as in Table 2.3.

Table 2.3.: Relevant Element Abundances

Element	GS98	AGSS09	Meteorites	Element	GS98	AGSS09	Meteorites
Be	1.40	1.38	1.30	N	7.92	7.83	6.26
B	2.55	2.70	2.79	O	8.83	8.69	8.40
C	8.52	8.43	7.39	Z/X	0.0229	0.0178	-
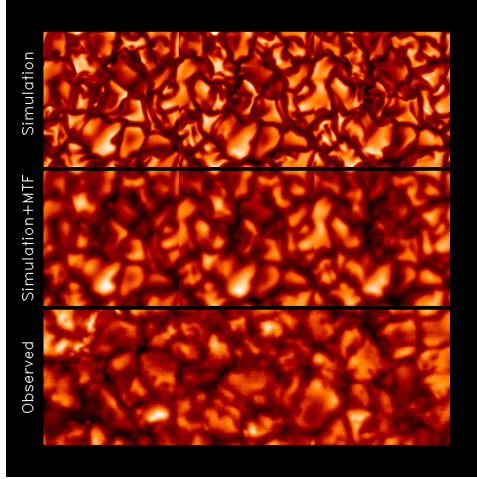
Figure 2.6.: Reproduction of Granulation (Stein) for (Trampedach et al., 2013). The top row is the granulation reproduced by the 3D simulation while the bottom row is the observed granulation in the solar surface. The simulation is smoothed with a modulation transfer function representing the effects of the telescope and atmospheric seeing in the middle row and gets very similar to the observed.

Inconsistencies

The significant decrease of carbon, nitrogen and oxygen has significant effect to the total amount of metal since they are the third largest element only to hydrogen and helium, which has caused several serious inconsistencies between resulting SSM and other observation.

One inconsistency appears in the relation between helioseismology. Table 2.4 shows some values about characteristics of the sun, where R_{CZ} is the radius of the outer edge of convection zone, $\langle \delta c/c \rangle$ and $\langle \delta \rho/\rho \rangle$ are the mean difference of SSM and Helioseismology on the sound speed profile and on the density profile. Notice that only the values for the density profile is taken from BPS09-SSM. For all parameters, SFII-GS98 shows better consistency to Heliosesmology. Figure 2.7 shows the difference of the sound speed profile

Table 2.4.: SFII-SSM and Helioseismology quantities

Parameters	SFII-GS98	SFII-AGSS09	Helioseismology
$(Z/X)_{\text{surface}}$	0.0229	0.0178	—
$R_{\text{CZ}}/R_{\odot}$	0.7124	0.7231	0.713 ± 0.001
Y_{surface}	0.2429	0.2319	0.2485 ± 0.0035
$\langle \delta c/c \rangle$	0.0009	0.0037	—
$\langle \delta \rho/\rho \rangle$	0.011*	0.040*	—

and the density profile between BPS09-SSM and Helioseismology. δ in the y axes of the both graphs mean the difference of SSM and Helioseismology. Readers may only review GS98 and AGSS09 in the graphs. For both sound speed and density, difference in AGSS09 gets larger.
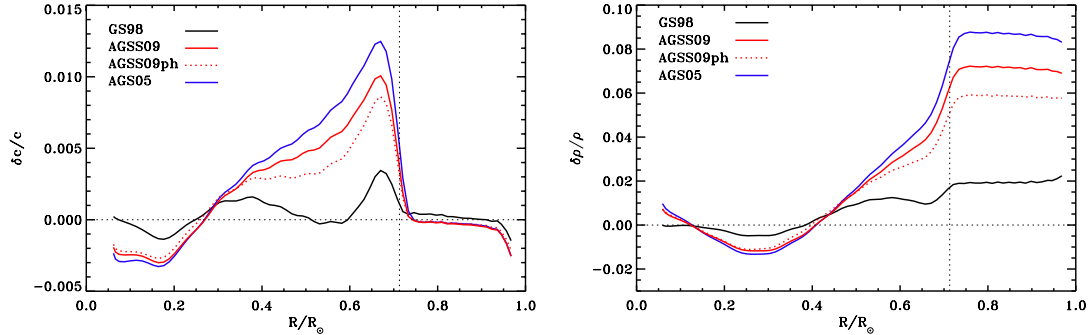
Figure 2.7.: Difference of SSM and Helioseismology on Sound Speed Profile and Density Profile. BPS09-SSM is shown. BPS09-GS98 is much consistent to Helioseismology than BPS09-AGSS09.

Another consistency appears in stellar evolution plot (VandenBerg et.al., 2008). The isochronous curves are computed for the heavier and the lighter metallicities based on the earlier abundance report (Asplund et al., 2005) and the plot is shown in Figure 2.8. There is so called turn-off structure from 0.5 to 0.6 and 3 to 4 of x and y coordinates, which is the boundary of main sequence stars and giant stars, and this structure is dependent to the age of a galaxy. The solid lines based on the lighter metallicities cannot reproduce the turn-off structure of M67 even testing with different ages.

This problem that a better modeling of the solar atmosphere causes inconsistencies between other physics is called 'Solar Abundance Problem'. There could be improvements for atmospheric modeling, abundance inference and SSM construction. For example 3D atmospheric model may need consideration of temperature upshift in the chromosphere. Thus currently there is no condition, which effectively discriminates the difference. Solar neutrino observation, which is the direct measurement of abundances, could be the key to solve the problem.

2.2. Neutrino Physics

2.2.1. Neutrino

Neutrinos are 3-generation electrically neutral lepton particles as in the bottom row in Table 2.5. Although they are massless particles in the standard model of particles, as described elsewhere, observed neutrino oscillation yields the finite mass of the neutrino and then requires the extension of the model.
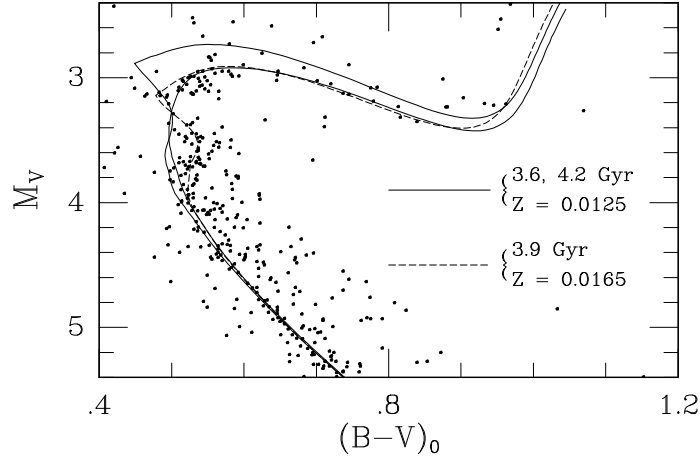
Figure 2.8.: Comparison of HR diagram in M67 and isochronous curve for different abundance

Table 2.5.: Quarks and Leptons

	charge	1st gen.	2nd gen.	3rd gen
Quarks	2/3	u	c	t
	-1/3	d	s	b
Lepton	-1	e	μ	τ
	0	ν_e	ν_μ	ν_τ

2.2.2. Neutrino Mixing

Neutrino oscillation as a mixing of eigenstates predicted and formulated in (Pontecorvo, 1957) then in (Maki et al., 1962).

Today, the mixing is enhanced that of 3 generation. The neutrino flavor eigenstate is related to the neutrino mass eigenstate by

$$|\nu_l\rangle = \sum_{i=1}^{3} U_{li} |\nu_i\rangle, \quad l = e, \mu, \tau, \quad i = 1, 2, 3, \tag{2.16}$$

where U is the Pontecorvo-Maki-Nakagawa-Sakata (PMNS) unitary mixing matrix. The PMNS matrix is broken down as

$$U_{\text{PMNS}} = U_{23} D U_{31} D^* U_{12}, \tag{2.17}$$

where D includes the Dirac CP-violating phase δ as

$$D = \begin{pmatrix} 1 & 0 & 0 \\ 0 & 1 & 0 \\ 0 & 0 & e^{i\delta} \end{pmatrix}, \tag{2.18}$$

14

and where U_{23}, U_{31} and U_{12} are following rotation matrices

$$U_{23} = \begin{pmatrix} 1 & 0 & 0 \\ 0 & c_{23} & s_{23} \\ 0 & -s_{23} & c_{23} \end{pmatrix}, \quad U_{31} = \begin{pmatrix} c_{13} & 0 & s_{13} \\ 0 & 1 & 0 \\ -s_{13} & 0 & c_{13} \end{pmatrix}, \quad U_{12} = \begin{pmatrix} c_{12} & s_{12} & 0 \\ -s_{12} & c_{12} & 0 \\ 0 & 0 & 1 \end{pmatrix},$$

(2.19)

where $s_{ij} = \sin\theta_{ij}$ and $c_{ij} = \cos\theta_{ij}$.

When the neutrino is a Majorana fermion, the unitary matrix U, U_{PMNS} is extended as,

$$U_{\mathrm{Majorana}} = U_{\mathrm{PMNS}}M,$$

(2.20)

where M includes the two Majorana phases α_1 and α_2 as

$$M = \begin{pmatrix} e^{i\alpha_1/2} & 0 & 0 \\ 0 & e^{i\alpha_2/2} & 0 \\ 0 & 0 & 1 \end{pmatrix}.$$

(2.21)

2.2.3. Neutrino Oscillation in Vacuum

The time development of neutrino wave function in their mass eigenstate are given by the Schrödinger equation and solved as

$$\frac{d}{dt}\left|\nu_j(t)\right\rangle = \frac{1}{i\hbar}\hat{H}\left|\nu_j(t)\right\rangle$$

(2.22)

$$\left|\nu_j(t)\right\rangle = e^{-iE_jt/\hbar}\left|\nu_j(0)\right\rangle.$$

(2.23)

Thus the time development of the flavor eigenstate is expressed as

$$\left|\nu_l(t)\right\rangle = \sum_j^3 U_{lj}e^{-iE_jt/\hbar}\left|\nu_j(0)\right\rangle.$$

(2.24)

The probability of neutrino transition from $\left|\nu_{l=a}(0)\right\rangle$ to $\left|\nu_{l=b}(t)\right\rangle$ is

$$P(\nu_a \rightarrow \nu_b) = |\langle\nu_a(0)|\nu_b(t)\rangle|^2$$

(2.25)

$$= \left|\sum_j^3 U_{aj}^* U_{bj}e^{-iE_jt/\hbar}\right|^2$$

(2.26)

$$= \sum_j^3\sum_k^3 U_{aj}U_{bj}^* U_{ak}^* U_{bk}e^{-i(E_k-E_j)t/\hbar}.$$

(2.27)

With applying Unitary condition

$$\delta_{ab} = \left|\sum_j^3 U_{al}U_{bj}^*\right|^2 = \sum_j^3 |U_{aj}|^2 |U_{bj}|^2 + \sum_{j\neq k}^3 U_{aj}U_{bj}^* U_{ak}^* U_{bk},$$

(2.28)

the probability is written as

$$P(\nu_a \to \nu_b) = \delta_{ab} + \sum_{j \neq k}^{3} U_{aj} U_{bj}^* U_{ak}^* U_{bk} (e^{-i(E_k - E_j)t/\hbar} - 1) \tag{2.29}$$

$$= \delta_{ab} - 4 \sum_{j > k} \mathrm{Re}(U_{aj} U_{bj}^* U_{ak}^* U_{bk}) \sin^2 \left(\frac{\Delta m_{kj}^2 c^4 t}{4 E_\nu \hbar} \right) \tag{2.30}$$

$$+ 2 \sum_{j > k} \mathrm{Im}(U_{aj} U_{bj}^* U_{ak}^* U_{bk}) \sin \left(\frac{\Delta m_{kj}^2 c^4 t}{2 E_\nu \hbar} \right), \tag{2.31}$$

where relativistic neutrino assumption,

$$\Delta E_{ij} = \frac{\Delta m_{ij}^2 c^4}{2 E_\nu} \tag{2.32}$$

$$(\Delta E_{ij} = E_i - E_j, \quad \Delta m_{ij}^2 = m_i^2 - m_j^2) \tag{2.33}$$

is used.

From (2.31), the survival probability of a electron neutrino ν_e is

$$P(\nu_e \to \nu_e) = 1 - 4 \sum_{j > k} |U_{ej}|^2 |U_{ek}|^2 \sin^2 \left(\frac{\Delta m_{kj}^2 c^4 t}{4 E_\nu \hbar} \right) \tag{2.34}$$

Using $\left| \Delta m_{32}^2 \right| \simeq \left| \Delta m_{31}^2 \right|$ and unitary condition, the probability is

$$P(\nu_e \to \nu_e) = 1 - 4 |U_{e3}|^2 (1 - |U_{e3}|^2) \sin^2 \left(\frac{\Delta m_{32}^2 c^4 t}{4 E_\nu \hbar} \right) - 4 |U_{e1}|^2 |U_{e2}|^2 \sin^2 \left(\frac{\Delta m_{21}^2 c^4 t}{4 E_\nu \hbar} \right) \tag{2.35}$$

$$= 1 - \sin^2 2\theta_{13} \sin^2 \left(\frac{\Delta m_{32}^2 c^4 t}{4 E_\nu \hbar} \right) - \cos^4 \theta_{13} \sin^2 2\theta_{12} \sin^2 \left(\frac{\Delta m_{21}^2 c^4 t}{4 E_\nu \hbar} \right) \tag{2.36}$$

In the phase term, time t is usually converted to range L ($L = ct$) in order to compare the term with an experimental result, and is expressed as

$$\frac{\Delta m_{kj}^2 c^4 t}{2 E_\nu \hbar} = 1.267 \frac{\Delta m_{kj}^2 c^4 L}{E_\nu} \frac{[\mathrm{eV}^2][\mathrm{m}]}{[\mathrm{MeV}]}. \tag{2.37}$$

2.2.4. Neutrino Oscillation in Matter

The time development of neutrino wave function in their flavor eigenstate in vacuum is given from the last section as

$$\frac{d}{dt} \begin{pmatrix} \nu_e(t) \\ \nu_\mu(t) \\ \nu_\tau(t) \end{pmatrix} = \frac{1}{i\hbar} U \begin{pmatrix} E_1 & 0 & 0 \\ 0 & E_2 & 0 \\ 0 & 0 & E_3 \end{pmatrix} U^\dagger \begin{pmatrix} \nu_e(t) \\ \nu_\mu(t) \\ \nu_\tau(t) \end{pmatrix} = \frac{1}{i\hbar} H_{\mathrm{vac}} \begin{pmatrix} \nu_e(t) \\ \nu_\mu(t) \\ \nu_\tau(t) \end{pmatrix} \tag{2.38}$$

16

When neutrinos propagate in matter, neutrinos feel potential of electrons, protons and neutrons. The neutral current by electrons and nucleons works equally to all generations of neutrinos, while the charged weak current by electrons affects only to electron neutrinos.Thus, the effective Hamiltonian in the matter is written with additional energy terms as

$$
H_{\text{matter}} = H_{\text{vac}} + \begin{pmatrix} V^{\text{ch}} + V^{\text{n}} & 0 & 0 \\ 0 & V^{\text{n}} & 0 \\ 0 & 0 & V^{\text{n}} \end{pmatrix} = H_{\text{vac}} + \frac{V^{\text{ch}} + 2V^{\text{n}}}{2} I + \frac{V^{\text{ch}}}{2} \begin{pmatrix} 1 & 0 & 0 \\ 0 & -1 & 0 \\ 0 & 0 & -1 \end{pmatrix},
$$
(2.39)

where V^{n} and V^{ch} are the extra energy terms for the neutral current and charged current, where $V^{\text{ch}} = \sqrt{2} G_F n_{\text{e}}$, with the Fermi coupling constant G_F and electron density n_{e}. The second term can be omitted on considering oscillation pattern.

For simplicity, two generation case will be considered. For this case, the Hamiltonian is expressed with omitting unnecessary phase terms as,

$$
H_{\text{matter}} = -\left(\frac{\Delta m_{12}^2 c^4}{4E_\nu} \cos 2\theta_{12} - \frac{V^{\text{ch}}}{2} \right) \begin{pmatrix} 1 & 0 \\ 0 & -1 \end{pmatrix} + \frac{\Delta m_{12}^2 c^4}{4E_\nu} \sin 2\theta_{12} \begin{pmatrix} 0 & 1 \\ 1 & 0 \end{pmatrix}.
$$
(2.40)

The Hamiltonian is diagonalized by new mass eigenstates ν_{1M} and ν_{2M} with new mixing matrix,

$$
\begin{pmatrix} \nu_e(t) \\ \nu_\mu(t) \end{pmatrix} = \begin{pmatrix} \cos\theta_{12M} & \sin\theta_{12M} \\ -\sin\theta_{12M} & \cos\theta_{12M} \end{pmatrix} \begin{pmatrix} \nu_{1M}(t) \\ \nu_{2M}(t) \end{pmatrix},
$$
(2.41)

where

$$
\begin{aligned}
\sin 2\theta_{12M} &= \frac{B}{\sqrt{A^2 + B^2}} \\
\cos 2\theta_{12M} &= \frac{A}{\sqrt{A^2 + B^2}} \\
A &= \frac{\Delta m_{12}^2 c^4}{4E_\nu} \cos 2\theta_{12} - \frac{V^{\text{ch}}}{2} \\
B &= \frac{\Delta m_{12}^2 c^4}{4E_\nu} \sin 2\theta_{12}
\end{aligned}
$$
(2.42)

The mass difference in matter is given as the eigenvalues of the Hamiltonian by

$$
\frac{\Delta m_{12M}^2 c^4}{4E_\nu} = \sqrt{A^2 + B^2}.
$$
(2.43)

resonance neutrino oscillation

The neutrino mixing gets maximum when $\theta_M = \pi/4$, which is given from (2.42) as

$$
A = 0 \iff \frac{\Delta m_{12}^2 c^4}{4E_\nu} \cos 2\theta_{12} = \frac{V^{\text{ch}}}{2},
$$
(2.44)

then, the mass difference is

$$\Delta m_{12M}^2|_{\text{resonance}} = \Delta m_{12}^2 \sin 2\theta_{12} \tag{2.45}$$

From (2.44), the electron density which gives this condition is

$$n_{\text{e}}^{\text{resonance}} = \frac{\Delta m_{12}^2 c^4 \cos 2\theta_{12}}{2\sqrt{2} G_F E_\nu}, \tag{2.46}$$

and which is called the resonant density.

survival probability in matter

Inside the Sun, the electron density is position dependent and V^{ch} varies as a neutrino flies, that is, θ_M also is variable. Then, (2.41) is

$$\begin{pmatrix} \nu_e(t) \\ \nu_\mu(t) \end{pmatrix} = \begin{pmatrix} \cos\theta_M(t) & \sin\theta_M(t) \\ -\sin\theta_M(t) & \cos\theta_M(t) \end{pmatrix} \begin{pmatrix} \nu_{1M}(t) \\ \nu_{2M}(t) \end{pmatrix} \equiv U_M(\theta_M(t)) \begin{pmatrix} \nu_{1M}(t) \\ \nu_{2M}(t) \end{pmatrix} \tag{2.47}$$

Thus,

$$\frac{d}{dt} \begin{pmatrix} \nu_e(t) \\ \nu_\mu(t) \end{pmatrix} = \dot{U_M}(\theta_M) \begin{pmatrix} \nu_{1M}(t) \\ \nu_{2M}(t) \end{pmatrix} + U_M(\theta_M) \begin{pmatrix} \dot{\nu_{1M}}(t) \\ \dot{\nu_{2M}}(t) \end{pmatrix}. \tag{2.48}$$

Then the time development equation of mass eigenstates is as,

$$\frac{d}{dt} \begin{pmatrix} \nu_{1M}(t) \\ \nu_{2M}(t) \end{pmatrix} = \frac{1}{i\hbar} U_M^\dagger H_M U_M \begin{pmatrix} \nu_{1M}(t) \\ \nu_{2M}(t) \end{pmatrix} - U_M^\dagger \dot{U_M} \begin{pmatrix} \nu_{1M}(t) \\ \nu_{2M}(t) \end{pmatrix}, \tag{2.49}$$

which can be simplified with again omitting the common phase term,

$$\frac{d}{dt} \begin{pmatrix} \nu_{1M}(t) \\ \nu_{2M}(t) \end{pmatrix} = \frac{1}{i\hbar} \left[-\frac{\Delta m_M^2 c^4}{4E_\nu} \begin{pmatrix} 1 & 0 \\ 0 & -1 \end{pmatrix} - i\dot{\theta_M}(t) \begin{pmatrix} 0 & 1 \\ -1 & 0 \end{pmatrix} \right] \begin{pmatrix} \nu_{1M}(t) \\ \nu_{2M}(t) \end{pmatrix}. \tag{2.50}$$

In this equation, if the diagonal elements are much larger than the off diagonal elements, the mass eigenstates are approximately the same as energy eigenstates, then ν_{jM} do not mix. This is called the *adiabatic transition approximation*. This condition is,

$$\Delta m_M^2 c^4 \gg 4E_\nu \dot{\theta_M}(t). \tag{2.51}$$

Then we define the adiabaricity parameter, Q as,

$$Q \equiv \frac{\Delta m_M^2 c^4}{4E_\nu \dot{\theta_M}} \tag{2.52}$$

The minimum of Q is at the resonant point, thus the most strict condition is

$$Q|_{\text{resonance}} = \frac{\Delta m^2 c^4 \sin^2 2\theta}{2E_\nu \cos 2\theta \left| \frac{d\log n_{\text{e}}(r)}{dr} |_{\text{resonance}} \right|} \gg 1. \tag{2.53}$$

Survival probability of electron neutrinos in matter are classified into four cases (Gonzalez-Garcia, 2003) with electron density at neutrino production point, $n_{\text{e}0}$, as,

1. $n_{\mathrm{e0}} \ll \frac{\sqrt{2}\Delta m^2 c^4}{4E_\nu G_F} \cos 2\theta$ $(A \sim \frac{\Delta m^2 c^4}{4E_\nu} \cos 2\theta)$:
   matter effects are negligible and the probability is the same as that in vacuum;

$$P(\nu_e \to \nu_e)^{2\nu}_{\mathrm{matter}} = 1 - \frac{1}{2}\sin^2 2\theta.$$

2. $n_{\mathrm{e0}} \leq \frac{\sqrt{2}\Delta m^2 c^4}{4E_\nu G_F} \cos 2\theta$:
   neutrino mixing is affected by the matter in the sun, but neutrino does not pass through the resonance point, then the probability is described with an adiabatic propagation;

$$P(\nu_e \to \nu_e)^{2\nu}_{\mathrm{matter}} = \frac{1}{2}(1 + \cos 2\theta_M \cos 2\theta)$$

.

3. $n_{\mathrm{e0}} > \frac{\sqrt{2}\Delta m^2 c^4}{4E_\nu G_F} \cos 2\theta \cap Q \gg 1$: a neutrino pass trough resonant point on its way out and the probability is described with an adiabatic propagation;

$$P(\nu_e \to \nu_e)^{2\nu}_{\mathrm{matter}} = \frac{1}{2}(1 + \cos 2\theta_{M0} \cos 2\theta)$$

, where θ_{M0} is the mixing angle at the production point.

4. $n_{\mathrm{e0}} > \frac{\sqrt{2}\Delta m^2 c^4}{4E_\nu G_F} \cos 2\theta \cap Q \ll 1$ a neutrino pass trough resonant point on its way out and the probability is described with an non-adiabatic propagation involving the state jump between ν_i and ν_j;

$$P(\nu_e \to \nu_e)^{2\nu}_{\mathrm{matter}} = \frac{1}{2}[1 + (1 - 2P_{\mathrm{LZ}}) \cos 2\theta_M \cos 2\theta]$$

, where P_{LZ} is the Landau-Zener probability.

The survival probability in matter in three generation neutrino case is given (Shi and Schramm, 1992) as

$$P(\nu_e \to \nu_e)^{3\nu}_{\mathrm{matter}} = P(\nu_e \to \nu_e)^{2\nu}_{\mathrm{matter}} \cos^4 \theta_{13} + \sin^4 \theta_{13} \tag{2.54}$$

with replacing θ_M, θ and n_e by θ_{12M}, θ_{12} and $n_e \cos^2 \theta_{13}$.

The n_{e} distribution in the sun in the latest solar model (Serenelli et al., 2011) is shown in Figure 2.9 with resonant densities for specified energies of neutrinos.

Even though resonance does not occur when the energy of a neutrino is smaller than 1.82 MeV even at the center of the sun, for ^{7}Be solar neutrinos, having either of 0.862 MeV or 0.384 MeV, the density is not negligible. This condition corresponds to 2. of the listed 4 cases above. Thus for ^{7}Be solar neutrinos, the survival probability of ^{7}Be solar neutrinos is expressed as,

$$P(\nu_e \to \nu_e)^{3\nu}_{\mathrm{Sun}} = \left[\frac{1}{2}(1 + \cos 2\theta_{12M} \cos 2\theta_{12})\right] \cos^4 \theta_{13} + \sin^4 \theta_{13}. \tag{2.55}$$
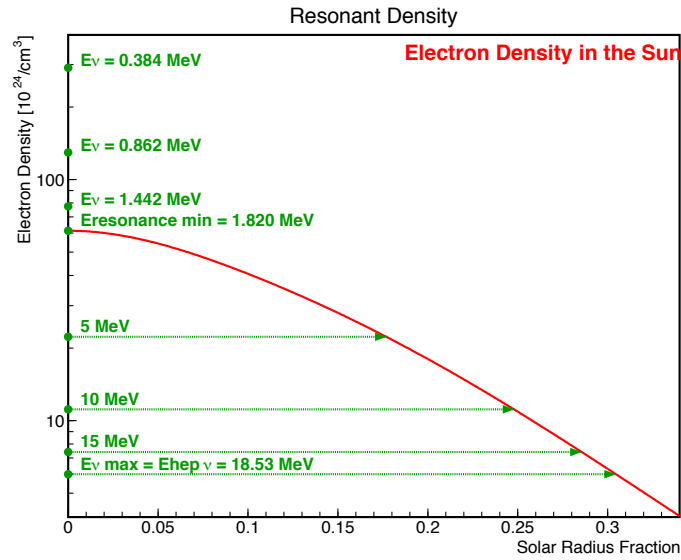
Figure 2.9.: Electron density in the sun and resonant density.
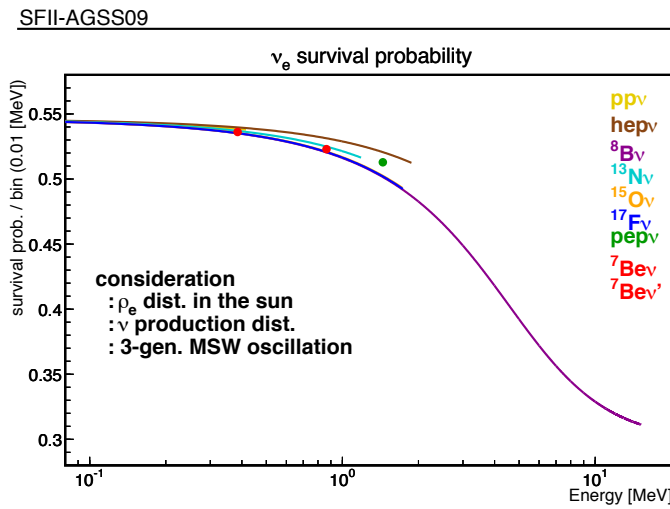
Figure 2.10.: Survival Probability distribution of solar neutrinos

By applying this formula to the n_e distribution in the sun and the radius distribution of solar neutrino production given from (Serenelli et al., 2011) as in 2.4, the energy distribution of the survival probability of solar neutrinos is calculated and shown in Figure 2.10. In the Figure, the distribution is drawn from the minimum to the maximum energy of each type of solar neutrinos. Different shapes among neutrinos reflect the different position dependence of production.

20

2.2.5. Neutrino Oscillation Parameters

The recommended oscillation parameters today in (Beringer et al. and Particle Data Group, 2013) is summarized in Table 2.6. In this analysis, Δm_{12}^2, θ_{12} and θ_{13} are only used, while the values for the former two are used from the table, and for θ_{13}, $\sin^2(2\theta_{13}) = 0.089 \pm 0.011$ from Daya Bay experiment (An et al. and Daya Bay Collaboration, 2013) is used.

Table 2.6.: Neutrino oscillation parameters

Parameter	Value	Unit
Δm_{12}^2	$7.50\,^{+0.19}_{-0.20}$	$10^{-5}\mathrm{eV}^2$
Δm_{23}^2	$2.32\,^{+0.12}_{-0.08}$	$10^{-3}\mathrm{eV}^2$
θ_{12} $(\sin^2(2\theta_{12}))$	$0.857\,^{+0.023}_{-0.025}$	
θ_{23} $(\sin^2(2\theta_{23}))$	> 0.95	
θ_{13} $(\sin^2(2\theta_{13}))$	0.095 ± 0.010	

2.3. Neutrino Detection by Neutrino-Electron Elastic Scattering

2.3.1. Neutrino-Electron Elastic Scattering

An active neutrino scatters an electron by elastic scattering as,

$$\nu + \mathrm{e}^- \rightarrow \nu + \mathrm{e}^-, \tag{2.56}$$

where ν includes ν_e, ν_μ and ν_τ. The law of conservation of mechanical energy and momentum gives the kinematic energy of a scattered electron as

$$T_\mathrm{e} = \frac{2m_\mathrm{e}c^2 E_\nu^2 \cos^2\theta}{(E_\nu + m_\mathrm{e}c^2)^2 - E_\nu^2 \cos^2\theta}, \tag{2.57}$$

where m_e is the mass of an electron, E_ν is the energy of a neutrino and θ is the scatter angle of the electron direction from the initial neutrino direction. The energy peaks when $\theta = 0$ as

$$T_\mathrm{e}^{\mathrm{max}} = \frac{2E_\nu^2}{2E_\nu + m_\mathrm{e}c^2}. \tag{2.58}$$

$T_\mathrm{e}^{\mathrm{max}}$, the maximum recoil electron energy for ^{7}Be solar neutrino is 0.665 and 0.231 MeV for 0.862 and 0.384 MeV of the two branches of the neutrino respectively.

2.3.2. Cross Section of Neutrino-Electron Elastic Scattering

The elastic scattering of either type of active neutrinos ($\nu_{e,\mu,\tau}$) and electrons has cross sections of

$$\frac{d\sigma}{dT_e} = \frac{2G_F^2 m_e(\hbar c)^2}{\pi}\left[g_L^2 + g_R^2\left(1 - \frac{T_e}{E_\nu}\right)^2 - g_L g_R \frac{m_e T_e}{E_\nu^2}\right], \tag{2.59}$$

where E_ν is the initial energy of neutrinos and T_e is the kinetic energy of recoil electrons. In the standard model, the coupling constants g_L and g_R are g_L are,

$$g_R = \sin^2\theta_W \tag{2.60}$$

$$g_L = \sin^2\theta_W \pm \frac{1}{2} \quad (\text{+ for } \nu_e \text{ and - for } \nu_{\mu,\tau}) \tag{2.61}$$

corresponding to usual vector and axial vector coupling constants as $g_V = g_R + g_L$ and $g_A = g_R - g_R$. θ_W is the Weinberg angle and evaluated as $\sin^2\theta_W = 0.23116 \pm 0.00012$ (Beringer et al. and Particle Data Group, 2013). The total cross section σ is calculated by integrating (2.62) over T_e from 0 to $T_{\max}$ in (2.58).

2.3.3. Radiative Correction on Cross Section

The radiative corrections to the cross section are calculated by (Bahcall et al., 1995). The correction reduces the cross section of the higher energy solar neutrinos e.g. ^{8}B solar neutrinos by 4 % or more, while that of ^{7}Be solar neutrinos by less than 1 %. According to the literature, the cross section is modified as

$$\begin{aligned}
\frac{d\sigma}{dT_e} = \frac{2G_F^2 m_e(\hbar c)^2}{\pi} \Bigg\{ & g_L^2(T_e)\left[1 + \frac{\alpha}{\pi}f_-\left(\frac{T_e}{E_\nu}\right)\right] \\
& + g_R^2(T_e)\left(1 - \frac{T_e}{E_\nu}\right)^2\left[1 + \frac{\alpha}{\pi}f_+\left(\frac{T_e}{E_\nu}\right)\right] \\
& - g_L(T_e)g_R(T_e)\frac{m_e T_e}{E_\nu^2}\left[1 + \frac{\alpha}{\pi}f_\pm\left(\frac{T_e}{E_\nu}\right)\right] \Bigg\},
\end{aligned} \tag{2.62}$$

where g_L and g_R is now function of T_e for taking electroweak and QCD effects into account, while f_-, f_+ and $f_\pm$ describe QED effects among virtual and real photons. The total uncertainty on the cross section for ^{7}Be solar neutrino is also calculated there to be 1.0 % and this is added as the systematic uncertainty for the event rate of ^{7}Be solar neutrinos.

Finally, SFII-SSM energy spectra of solar neutrinos are shown in Figure 2.11.
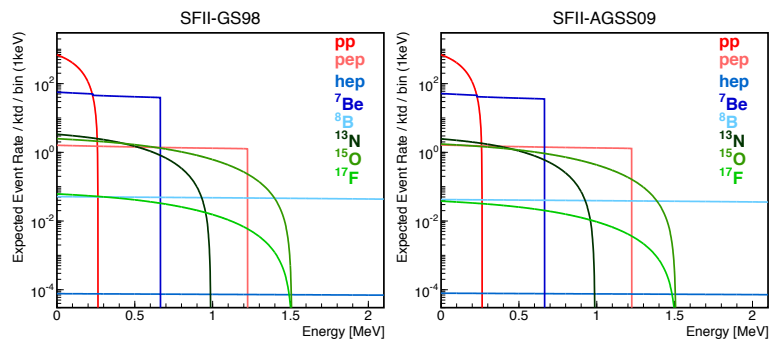
Figure 2.11.: Solar Neutrino Energy Spectra in KamLAND.

2.3.4. Neutrino Experiments

Neutrinos was first predicted in 1930 by W. Pauli in order to conserve energy in a β decay, and was named by E. Fermi in 1934. It has been clear that detection of neutrinos is difficult since it was already discussed that a neutrino is electrically neutral and is almost massless, and that the reactivity is at most 1/10 of that of a γ.

The first neutrino observation was done in 1953 by C. Cowan and F. Reines in Hanford reactor. The inverse β decay of

$$\bar{\nu}_e + p \rightarrow n + e^+, \tag{2.63}$$

in a liquid scintillation detector was observed.

In 1955 R. Davis.Jr discovered that a neutrino and an anti-neutrino is a different particle with a radiochemical method,

$$^{37}Cl + \nu_e \rightarrow {}^{37}Ar + e^-, \tag{2.64}$$

in Brookhaven reactor.

In 1962, L. M. Lederman, M. Schwartz and J. Steinberger discovered that there is a different flavor of neutrinos, μ neutrinos, with using a proton accelerator in Brookhaven national laboratory, and attested existence of generation for neutrinos as well as for quarks, which was already discussed. The last neutrinos in the 3-generation, τ neutrinos was first observed recently in 2000.

In the following description, what is mentioned as SSM is SSM-BPS08-GS98 (Pena-Garay and Serenelli, 2008).

Homestake Experiment

On the other hand from experiments using reactors or accelerators, a neutrino observation experiment using the sun as a neutrino source was performed by Davis mentioned above for a long period from 1967 to 1994 in Homestake mine. The experiments used the same radiochemical method far underground in order to reduce the background events against solar neutrinos generated by cosmic rays.

The neutrino targets was 615 tons of C_2Cl_2 and ^{37}Ar generate in (2.64) was purged by He gas bubbling every several months and trapped by an activated charcoal filter. The number of ^{37}Ar and thus the number of neutrino reaction was measured by the inverse reaction of (2.64) with a proportional counter. The energy threshold of the reaction is 0.814 MeV and is sensitive to ^8B and ^7Be solar neutrinos. The number of observed neutrinos and of SSM expectation in the unit SNU (the Solar Neutrino Unit; 10^{-36} events/s/number of target atoms) is as follows,

Homestake : 2.56 ± 0.16 (stat.) ± 0.16 (syst.)
SSM   : $8.46 \, ^{+0.87}_{-0.88}$.

The ratio of the observed to the expected is only 30 %, and this inconsistency questioned both the SSM and the theory of neutrinos and is called the 'Solar Neutrino Problem'.

GALLEX, GNO experiment and SAGE

While Homestake experiment utilized ^{37}Cl as a neutrino target, three neutrino experiments utilized ^{71}Ga as a target. The detection and counting method is almost the same as what is done for ^{37}Cl, that is, the detection by a radiochemical method,

$$^{71}\mathrm{Ga} + \nu_e \rightarrow\, ^{71}\mathrm{Ge} + e^-, \tag{2.65}$$

underground, and counting of ^{71}Ga by a proportional counter after purged. The major superiority of this reaction is the lower energy threshold, 0.2332 MeV, which opens the energy window for pp neutrinos which have the largest fluxes.

GALLEX (GALLium EXperiment) was done underground in Gran Sasso d'Italia, using 12 tons of ^{71}Ga in 101 tons of $\mathrm{GaCl_3}$–HCl solvent as a neutrino target, which was succeeded by GNO (Gallium Neutrino Observatory) experiment with the update of DAQ electronics.

SAGE (Soviet American Gallium Experiment) was done in Baksan Neutrino Observatory in Andyrchi mountain, using 30 tons of liquid metal Ga (later enhanced to 60 tons).

The number of observed neutrinos and of SSM expectation in the unit SNU is as follows,

$$
\begin{aligned}
\text{GALLEX} \quad &: 77.5 \pm 6.5 \text{ (stat.) } ^{+4.3}_{-4.7} \text{ (syst.)} \\
\text{GNO} \quad &: 62.9\, ^{+5.5}_{-5.3} \text{ (stat.) } \pm 2.5 \text{(syst.)} \\
\text{GALLEX + GNO} \quad &: 69.3 \pm 5.5 \\
\text{SAGE} \quad &: 67.2\, ^{+7.2}_{-7.0} \text{ (stat.) } ^{+3.5}_{-3.0} \text{ (syst.)} \\
\text{SSM} \quad &: 127.9\, ^{+8.1}_{-8.2}
\end{aligned}
$$

The observed numbers are consistent within their uncertainty and still $\sim$50% of the expected. Although the ratio is larger than that in ^{37}Cl, the large deficit confirmed the solar neutrino problem.

Kamiokande and Super-Kamiokande experiments

The existence of the problem was confirmed rather earlier in 1989 by Kamiokande II experiment. Kamiokande existed at 1000 m underneath the mount top of Ikenoyama in Gifu prefecture, Japan, which was experimentally succeeded by Super-Kamiokande (SK) and physically succeeded by KamLAND.

The detector contained 2 kton of pure water inside a cylindrical stainless steel tank of 13.1 m height and 7.2 m radius. Detection method there is electron scattering by neutrinos. A scattered electron runs faster than the speed of light in the water then emits Cherenkov light, which are then detected by photo multipliers. Neutrino observation by real time measurement of Cherenkov light is a strong method which gives much information; the direction, energy, time and flux of a neutrino.

Since electron scattering occurs between electrons and all types of active neutrinos, ν_e, ν_μ and ν_τ, Kamiokande has sensitivity to all those neutrinos, while it is 6 times more sensitive to ν_e than the others due to the different cross section.

The energy threshold of Kamiokande is 9.3 MeV at the beginning and later lowered to 7.5 MeV, which enables detection of ^{8}B solar neutrinos. The ratio of the observed neutrino flux to the SSM expectation is

$$Ratio_{\text{observed}} = 0.46 \pm 0.05(\text{stat.}) \pm 0.06(\text{syst.}),$$

and showed evidence of the solar neutrino problem.

The subsequent experiment, Super Kamiokande has been running since 1996 with enhanced amount of water, 50 ktons and with enhanced number of photomultipliers in a cylindrical stainless steel tank of 40 m both in height and diameter. The observation period are separated into three according to the change of available number of photomultipliers ant the upgrade of electronics, which are called SKI (Hosaka et al., 2006), SKII (Cravens et al., 2008) and SKIII (Abe et al., 2011). The observed ^{8}B neutrino fluxes for each period and SSM prediction are as follows with unit $\times 10^6 \text{cm}^{-2}\text{s}^{-1}$,

$$\phi_{\text{SKI}} = (2.35 \pm 0.02(\text{stat.}) \pm 0.08(\text{syst.}))$$
$$\phi_{\text{SKII}} = (2.38 \pm 0.05(\text{stat.})^{+0.16}_{-0.15}(\text{syst.}))$$
$$\phi_{\text{SKIII}} = (2.32 \pm 0.04(\text{stat.}) \pm 0.05(\text{syst.}))$$
$$\phi_{\text{SSM}} = (5.94 \pm 0.65).$$

These fluxes corresponds to the observed ratio of

$$Ratio_{\text{SKI}} = 0.396 \pm 0.045,$$

which also confirms the solar neutrino problem.

SNO experiment

Another neutrino observation experiment with Cherenkov light is SNO (Sudbury Neutrino Observatory) experiment. The superiority in this experiment utilization of D_2O. Neutrinos interact D_2O by electron scattering (ES) as in Super-Kamiokande, and also by charged current (CC) interaction and neutral current interaction (NC). These interactions are denoted as follows,

$$\text{ES}: \quad \nu_x + e^- \rightarrow \nu_x + e^- \tag{2.66}$$
$$\text{CC}: \quad \nu_e + d \rightarrow 2p + e^- \tag{2.67}$$
$$\text{NC}: \quad \nu_x + d \rightarrow \nu_x + p + n \tag{2.68}$$

NC is sensitive to all neutrinos as ES, but its superiority is based on the equality of cross section among all active neutrinos.

NC interaction does not emit an electron, then the interaction is detected by a neutron. SNO experiment utilized 3 different methods to detect neutrons, first with pure D_2O, later with D_2O + NaCl, and finally with D_2O + ^{3}He proportional counter (NC detector,

or NCD). The 3rd phase, so called NDC phase yielded following neutrino fluxes for each interaction,

$$\phi_{\mathrm{ES}} = 1.77^{+0.24}_{-0.21}(\mathrm{stat.})^{+0.09}_{-0.10}(\mathrm{syst.}) \tag{2.69}$$

$$\phi_{\mathrm{CC}} = 1.67^{+0.05}_{-0.04}(\mathrm{stat.})^{+0.07}_{-0.08}(\mathrm{syst.}) \tag{2.70}$$

$$\phi_{\mathrm{NC}} = 5.54^{+0.33}_{-0.31}(\mathrm{stat.})^{+0.36}_{-0.34}(\mathrm{syst.}), \tag{2.71}$$

in $\times 10^6 \mathrm{cm}^{-2}\mathrm{s}^{-1}$, which correspond to the detection ratio as follows,

$$R_{\mathrm{ES}} = 0.298 \pm 0.053 \tag{2.72}$$

$$R_{\mathrm{CC}} = 0.281 \pm 0.034 \tag{2.73}$$

$$R_{\mathrm{NC}} = 0.933 \pm 0.130. \tag{2.74}$$

ES or CC interaction yielded 30 % flux of SSM prediction, while NC interaction yielded consistent flux. This is the most obvious evidence that the total flux of active neutrinos conserve and that the solar neutrino problem is solved. From the all three phases, ^{8}B solar neutrino flux observed in SNO is reported as

$$\phi_{^8\mathrm{B}} = 5.25 \pm 0.16(\mathrm{stat.})^{+0.11}_{-0.13}(\mathrm{syst.}), \tag{2.75}$$

which corresponds to the detection ratio of

$$R_{^8\mathrm{B}} = 0.884 \pm 0.103. \tag{2.76}$$

Borexino experiment

The concept of Borexino experiment is vary similar to that of KamLAND and thus the detector and physics target is also quite similar. The detecter schematic of Borexino is shown in Figure 2.12.

The major differences lie between two experiment are the depth, detector size and composition of liquid scintillator. Borexino is located in a mountain in Italy, Gran Sasso, at a depth of 3,800 m.w.e, while KamLAND is located in a mountain in Japan, Ikenoyama at a depth of 2,700 m.w.e. Difference of the depth gives 1/8 smaller flux of cosmic muon for Borexino. Borexino contains 278 tons of liquid scintillator while KamLAND contains 4 times larger 1000 tons of liquid scintillator. The liquid scintillator of Borexino contains 100 % pseudocumene (1,2,4-trimethylbenzene) and 1.5 g/L PPO (2,5-diphenyloxazole), while KamLAND uses the 80 % normal paraffin (n-Dodecane), 20 % pseudocumene and 1.36 g/L PPO. The superiority of pseudocumene on pulse shape discrimination allows Borexino to analytically separate a radioactive background ^{210}Po. Both of the liquid scintillator was purified via water extraction, distillation and nitrogen purge.

Borexino started observation in 2007, reported first result in 2008. It reported the final results of its Phase-I period (Bellini et al. and Borexino Collaboration, 2013). Observed period was from May 16, 2007 to May 8, 2010, corresponding to 740.7 live days an 153.6 ton-yr (56.1 kton-days). The interaction rate is

$$R^{^7\mathrm{Be}} = (46.0 \pm 1.5(\mathrm{stat.})^{+1.5}_{-1.6}(\mathrm{syst.})) \text{ cpd}/100 \text{ t}, \tag{2.77}$$
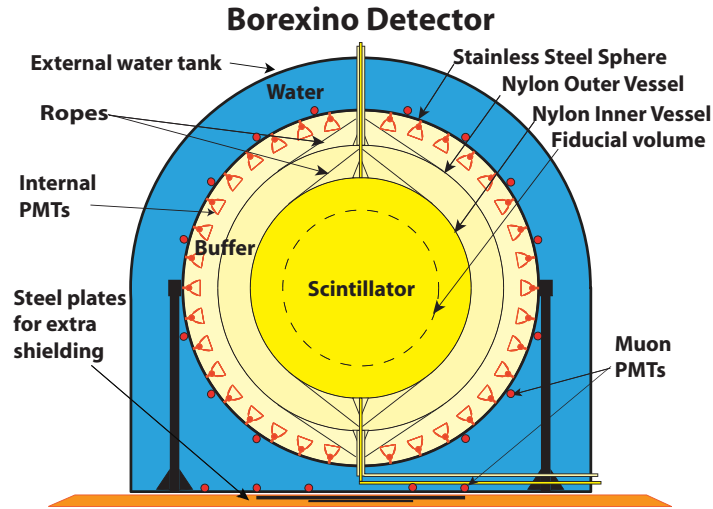
Figure 2.12.: Borexino Detector

and the total uncertainty is 4.6 %.

Under assumption of the MSW-LMA scenario, the measured event rate corresponds to ^{7}Be solar neutrino flux as

$$\Phi_{^7\mathrm{Be}} = (4.75^{+0.26}_{-0.22}) \times 10^9 \mathrm{cm}^{-2}\mathrm{s}^{-1}. \tag{2.78}$$

Figure 2.13 shows comparison of SSM predictions and experimental solar neutrino flux for ^{7}Be and ^{8}B. In the figure SHP11SSM corresponds to SFII-SSM and x and y axes are the ^{8}B and ^{7}Be solar neutrino flux ratio to SFII-SSM-GS98 model flux. The allowed region are evaluated with solar neutrino data from Homestake, GALLEX/GNO, SAGE, SNO, SK and Borexino as well as reactor anti-neutrino data from KamLAND, and it is located very middle of the two SSM predictions and still chemical abundance issue is controversial.
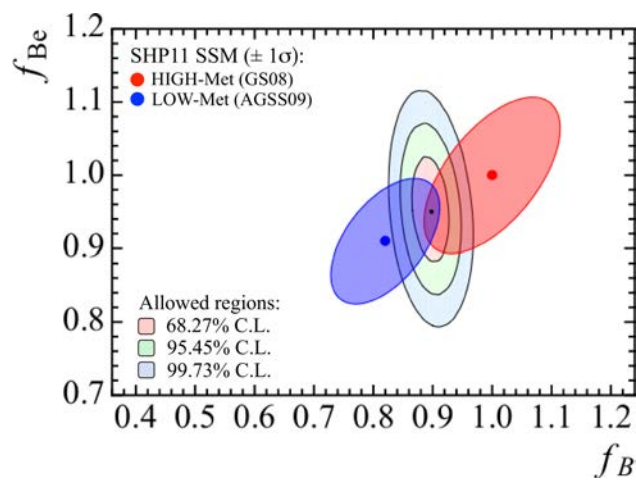
Figure 2.13.: Comparison of SSM prediction with Borexino plus ^{8}B solar experiments plus KamLAND

3. The Detector

The detector KamLAND (**Kam**ioka **L**iquid scintillator **A**nti-**N**eutrino **D**tector) is constructed for a primary observation target of reactor antineutrinos for the measurement of neutrino oscillation. Other main detection targets are as follows,

- Geo-neutrinos for the study of geophysics $(\bar{\nu}_e)$

- ^{8}B and then ^{7}Be solar neutrinos for the study of neutrino oscillation and the study of the sun (ν_e).

All of these physics targets are enabled with large statistics and low energy sensitivity given from the vast amount of the liquid scintillator.

3.1. Detection Method

3.1.1. Detection of Anti-neutrinos

Anti-neutrino detection utilizes the inverse β decay as follows,

$$\bar{\nu}_e + p \rightarrow e^+ + n \tag{3.1}$$

This reaction is followed by the two independent cascade reactions as follows and is tagged effectively by delayed coincidence method with information of energy, time interval and spatial distance.

- Prompt event
  Scintillation by at least 2γ of 511 keV for each from the annihilation of the positron and an electron in the liquid scintillator.

- Delayed event
  Scintillation by 2.2 MeV γ emitted from capture of the neutron by a hydrogen nucleus in the liquid scintillator, which occurs approximately 210 us of time constant.

This reaction has energy threshold due to the difference of energy among the initial and final state and is given as

$$E_{th} = (m_n + m_e) - (m_p) = 1.805 \text{ MeV}. \tag{3.2}$$

This reaction is visualized as in Figure 3.1.

The energy conservation law gives following relation

$$E_{\bar{\nu}_e} + m_p = (T_{e^+} + m_e) + (T_n + m_n), \tag{3.3}$$
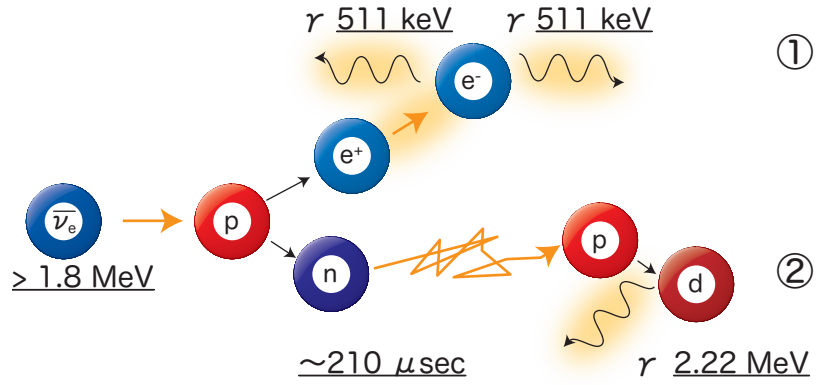
Figure 3.1.: Delayed Coincidence Events of Inverse β decay of $\bar{\nu}_e$

and the visible energy seen in KamLAND is given as

$$E_{\text{visible}} = T_{e^+} + 2m_e \tag{3.4}$$
$$\simeq E_{\bar{\nu}_e} - 0.78 \text{ MeV}, \tag{3.5}$$

where $T_n \simeq 0$ is used.

3.1.2. Detection of Neutrinos

The interaction of neutrinos is visualize in Figure 3.2. The reaction and the calculation
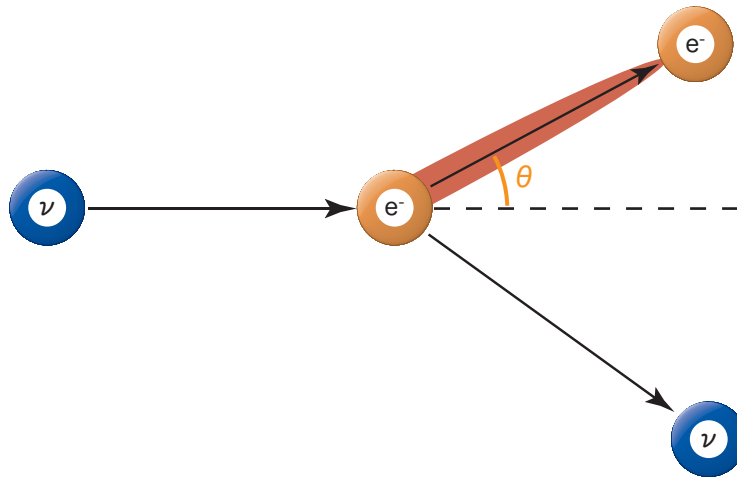
Figure 3.2.: Elastic Scattering of electron by ν_e

is described in the previous chapter. Events which are not able to be tagged by delayed coincidence method are called single events and all of them can be background sources for the solar neutrino analysis.

31
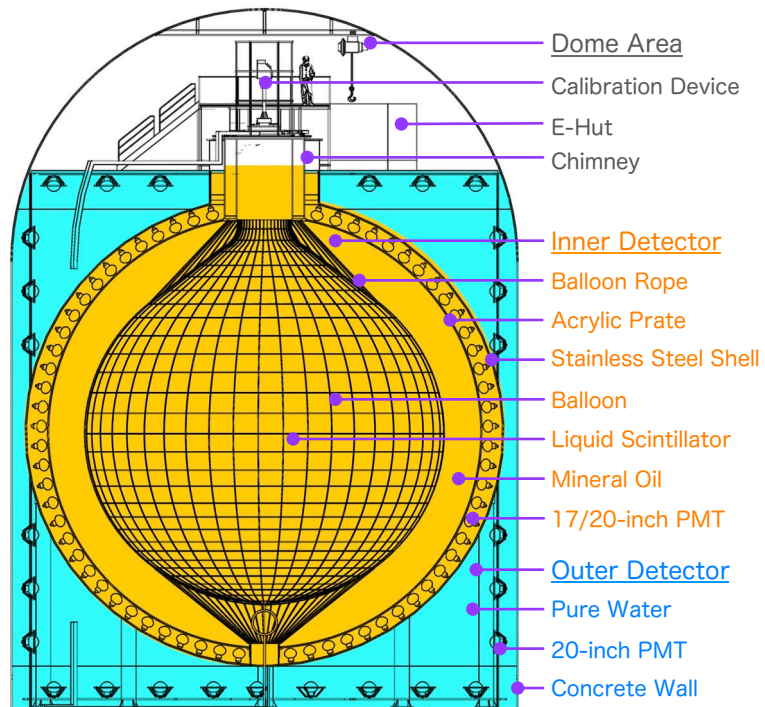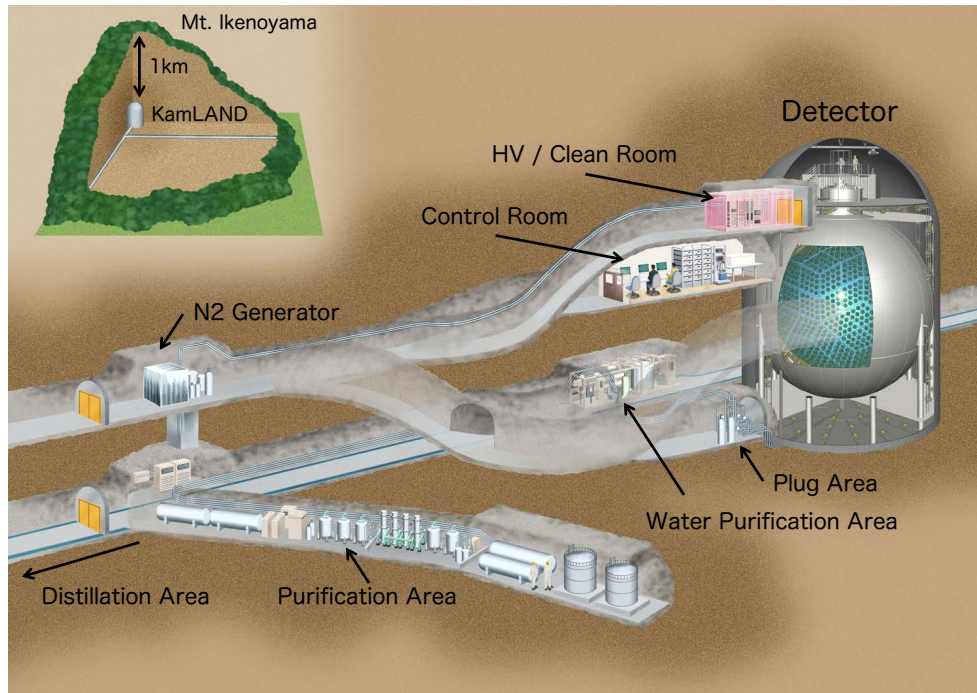
3.2. KamLAND

Figure 3.3.: KamLAND Detector Schematic View

The detector KamLAND is located 1000 m below the mount top of Ikeno-yama in Gifu prefecture, Japan. It was constructed in the cavity where the detector of KAMIOKANDE used to be, with extending the cavity 4m lower after the former was removed for the upgrade into Super Kamiokande. The construction was started in 1997, and the data acquisition has been done since 2002. The overburden of 2700 meter water equivalent rocks reduce the intensity of a serious background source, high energy cosmic muons 10^{-5} from that at the ground level.

The so called KamLAND area in the mount is shown in Figure 3.3. There are 4 access tunnels to KamLAND and many facilities, such as the liquid scintillator purification system, the water purification system, the pure nitrogen generator, the radon free air generator, the monitoring and "control" room and the clean room are located.

3.2.1. Detector Components

The schematic of KamLAND is shown in Figure 3.3 The detector consists of a mainly 3-layer structure, from the center, a liquid scintillator (LS) detector, a buffer oil (BO) region and a water Cherenkov detector. The liquid scintillator detector and the buffer oil is also called Inner Detector (ID) and the other is called Outer Detector (OD).

The 1000 ton of LS is contained in 6.5 m radius transparent balloon. The balloon has a thickness of 135 um, consists of 5 layers of EVOH/Nylon/Nylon/Nylon/EVOH films. The structure is determined with consideration of mechanical strength of Nylon films and gas tightness and chemical tolerance of EVOH films and total thickness. A set of 44 longitudinal and 30 latitudinal Kevlar ropes support the balloon from outside.

The balloon is surrounded by 1400 ton of mineral oil (MO) inside a 9 m radius spherical stainless steel shell (SSS). The MO is called BO since it helps to shield the LS from external γ particles. It consists of 53 % of dodecane and 47 % of isoparaffin and gives buoyancy for the LS and the balloon. The density difference of the BO and LS is precisely controlled, less than 0.01 % or less than 100 kgf/cm^2 in total of the balloon surface, in order not to let the balloon shrink or not to let it inflated and burst. On the inner surface of the 9 m SSS, 1325 17-inch PMTs and 554 20-inch PMTs are settled, giving 22 % and 12 % of photo coverage for each. Acrylic prates are located just in front of the PMTs at 8.3 m radius in order to reduce eternal γ particles. The refractive index of the prates is chosen close to that of the LS and the MO.

Outside the SSS is meant to be a water Cherenkov detector and 3200 ton of pure water is contained inside a concrete wall. 225 20-inch PMTs monitor Cherenkov light emitted mostly by high energy sources, such as cosmic muons, which induces a very large amount of background events. The detector provides a external γ particle shield for the ID. The detector is provided approximately 10 m^3/hr of purified water, which also works as coolant of the ID. The temperature of ID is monitored at various position at 0.1 °C sensitivity and the amount of water supplied to the detector is control not to break the equilibrium.

Above the detector, a space, so called Dome Area is located and some facilities, including a electronics hut are located. At the center of the detector, which corresponds to the place just above the center of the ID, calibration control devices are located. A

calibration source could be introduced into the ID by these devices through a vertical and cylindrical access hole, Chimney. The Chimney also supports the balloon ropes, and it also gives LS and MO circulation lines from/to the ID and from/to the purification system. The shortage of shielding by the OD at the Chimney is compensated by 16 8-inch PMTs and 6 5-inch PMTs.

3.2.2. Liquid scintillator

The KamLAND contains 1000 ton of ultra-pure liquid scintillator (LS) in the inner detector, which has huge number of electrons ($\sim 3 \times 10^{29}$) for targets of elastic scattering with neutrinos. The composition of the LS was determined to meet requirements of high light yield, high optical transparency, low radioactive contamination, high flash point, long term stability. The composition and the specification differs between before and after the 2nd purification, which is described later. The values at initial evaluation refer to (Tajima, 2003).

The LS is composed of 80.2 % of normal paraffin (n-Dodecane, $C_{12}H_{26}$), 19.8 % of pseudocumene (1,2,4-Trimethylbenzene, C_9H_{12}) and 1.36 g/L of PPO (2,5-Diphenyloxazole, $C_{15}H_{11}NO$). PPO is added in order to obtain a high light yield and the amount of it in the LS was initially 1.52 g/L and was modified and measured during the 2nd purification with gas chromatography to be 1.36 ± 0.03 g/L.

The attenuation length of the LS was initially measured with a dye laser calibration to be approximately 10 m at 400 nm wavelength. The light output was also measured as 8.3×10^3 photons/MeV, which corresponds to 49 % of that of anthracene. The light yield for events at the center of the detector was initially measured approximately 300 p.e./MeV by using only the 17-inch PMTs, and approximately 500 p.e./MeV by using the 17-inch and 20-inch PMTs. After the 2nd purification, the light yield degraded to approximately 200 and 450 p.e./MeV respectively.

Liquid Scintillator Purification

The liquid scintillator was initially purified for KamLAND, which made it possible to measure higher energy neutrinos, such as ^8B solar neutrinos, reactor anti-neutrinos, and geo neutrinos. The purification method employed here was water extraction of metal elements followed by nitrogen purging, and the processing system is called 'the 1st purification system'.

Figure 3.4 is a typical lower energy data before ^7Be solar neutrino phase in KamLAND. In order to measure ^7Be solar neutrinos, much more dominant backgrounds, ^{210}Bi and ^{210}Po, which are daughter radioactive isotopes of $^{226}Ra/^{222}Rn$, ^{85}Kr a noble gas isotope, and ^{40}K a metal isotope had to be predominantly reduced in advance. Various laboratory studies discovered that distillation of LS followed by nitrogen purging was the most effective method to accomplish this. A mass processing facility was constructed and is called 'the 2nd purification system'.

The KamLAND LS was purified in two periods, from Mar.12, 2007 to Aug.1, 2007 and from Jun. 16, 2008 to Feb. 6, 2009 with both the 1st and 2nd purification system.
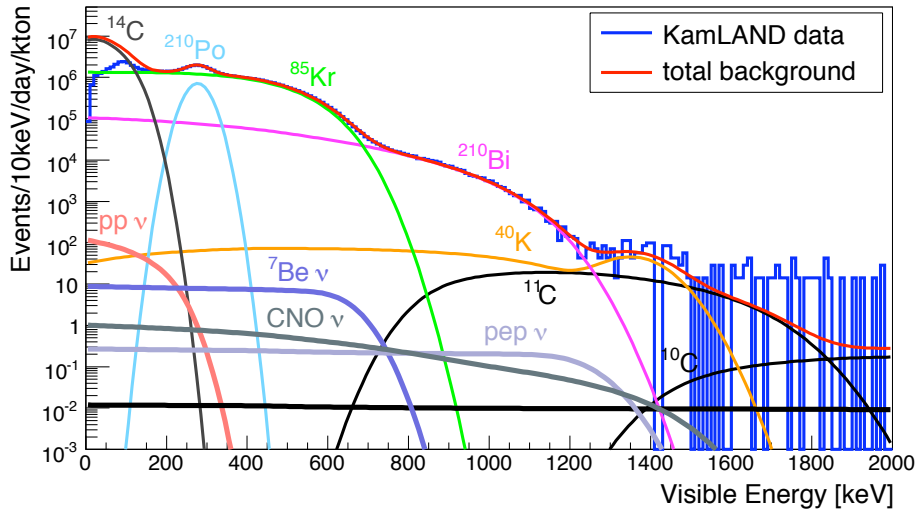
Figure 3.4.: Event Rate distribution before 2nd Purification (Nakajima, 2009).

The total amount of liquid scintillator purified was 4855 m^3, which is approximately 4.1 times of the amount of KamLAND LS.

1st Purification; Water Extraction and Nitrogen Purge

The 1st purification system is connected to KamLAND in order to thoroughly circulate and purify the oil in the detector. It provides two lines for each of LS and MO. Figure 3.5 shows the schematics of the flow of the purification.
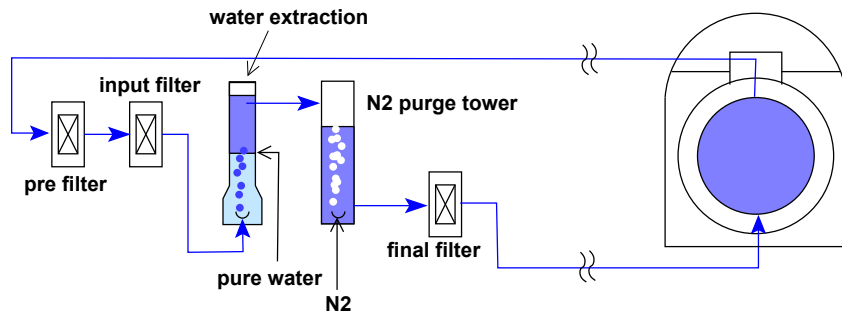
Figure 3.5.: 1st Purification; Water Extraction with Nitrogen Purge. (Tajima, 2003)

The oil coming from the detector or the newly fed goes through the pre and input filters and particle impurities are removed in advance. During water extraction, the oil goes through pure water. Metal elements such as U, Th and K are captured by the polarized water molecules and removed from the oil. In the next step, nitrogen purges water and O$_2$ which worsen the data quality via degrading light yield, transparency

and quench. It also purges radioactive noble gasses ^{222}Rn, ^{85}Kr, ^{39}Ar which are the background sources of ^{7}Be solar neutrinos.

2nd Purification; Distillation and Nitrogen Purge

A schematic of the 2nd purification system is shown in Figure 3.6. This system is only dedicated for the LS. The LS coming from the detector or from the 1st purification sys-
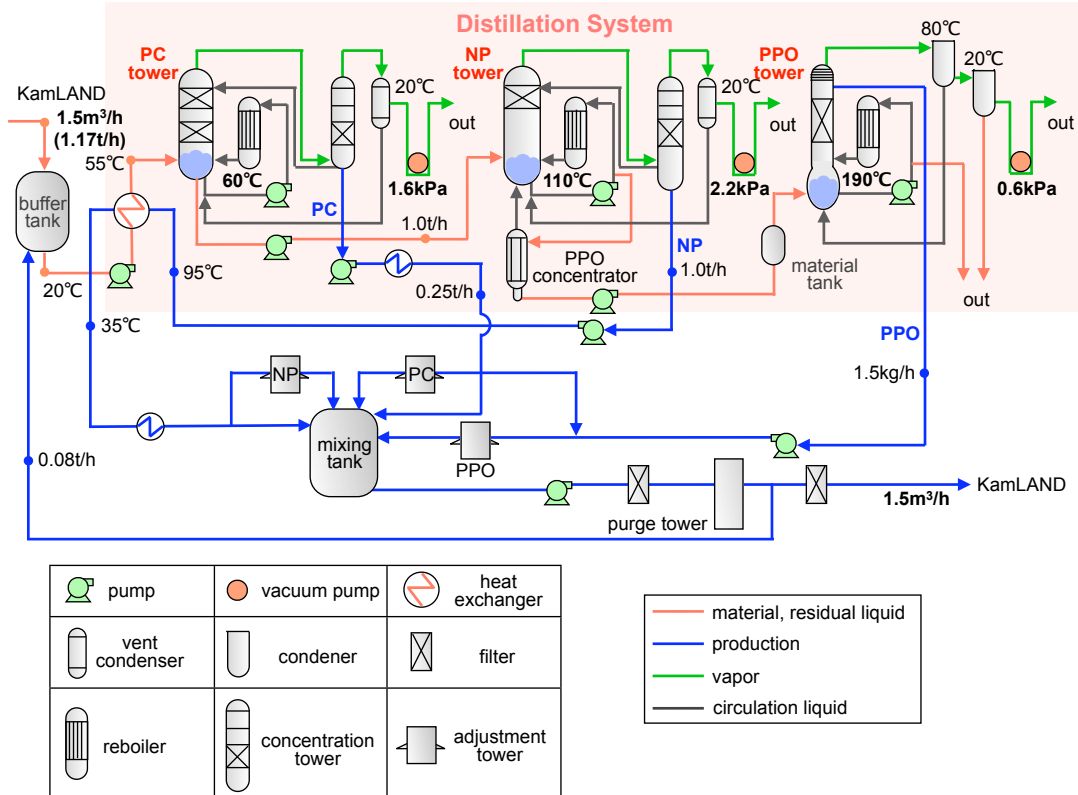
Figure 3.6.: 2nd Purification; Distillation with Nitrogen Purge. (Nakajima, 2009)

tem is fed to the buffer tank for distillation. The main component of liquid scintillator, pseudocumene (PC), normal paraffin (NP) and PPO are extracted by fractional distillation method in the three distillation towers controlled in different temperatures and pressures considering difference on boiling points. Those parameters are summarized in Table 3.1. The pure products of PC, NP and PPO are mixed in the mixing tank with the accuracy of 10^{-3} g/cm^3.

After the mixing, nitrogen purges radioactive noble gasses ^{222}Rn, ^{85}Kr, ^{39}Ar in the purge tower. On nitrogen purge in the 1st purification, nitrogen was reused and the gasses to be removed from the oil highly condensed in the nitrogen, which limited the purification quality. In the 2nd purification, a high purity nitrogen generator was constructed and at most 40 m^3/hour of fresh nitrogen was sent to the purge tower and also to the distillation towers for sealing.

Table 3.1.: Distillation Control Parameters

Component	Boiling Point [°C]	Tower	Pressure [kPa]	Temperature [°C]
Pseudocumene	169	PC	1.6	60
Dodecane	216	NP	2.2	110
PPO	360	PPO	0.6	190

The total distillation speed of the LS is 1.5m^3/hour, which requires a month for distillation of whole LS of KamLAND. During the whole distillation works, the stability of density, transparency and light yield of the LS and the concentration of ^{222}Rn and the daughter isotopes as well as of ^{85}Kr in the LS were continuously monitored by either of independent measurement apparatuses or KamLAND itself.

3.2.3. Data Acquisition

Photomultiplier Tubes

In KamLAND, a one MeV low energy event corresponds to approximately 200 photo electrons for 17-inch PMTs, including the reduction efficiency by the light attenuation of the liquid scintillator, the photo coverage and the quantum efficiency of PMT surfaces. Since KamLAND uses 1879 PMTs for the ID, the number of photo electron detected by a PMT is at most one, thus the resolution of time and voltage or electric current down to one photo electron is required.

The 17-inch PMTs were newly developed for KamLAND based on the former Hamamatsu 20-inch PMTs (R3600). Figure 3.7 shows the mechanical difference of the PMTs. Although the size of the PMT is still, it is called 17-inch PMT since the edge region is
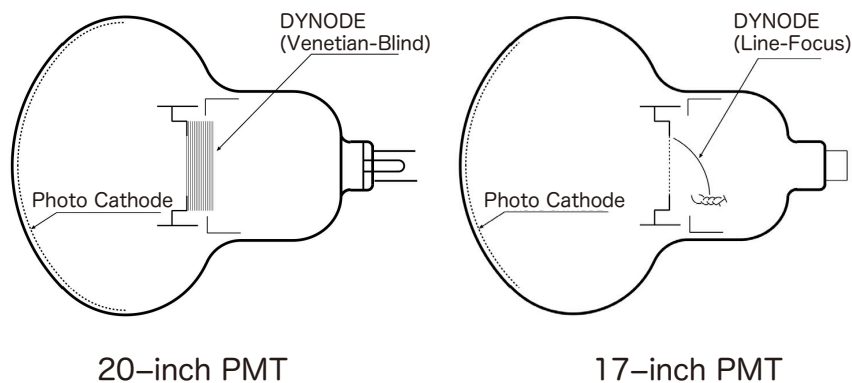
Figure 3.7.: Schematic of 20-inch and 17-inch PMTs

not used and masked physically by black plastic plates, in order to eliminate the contribution of worse time and energy response of the region. With this mask, the region photo-electrons fly in the PMT is narrowed and a line focus type dynodes of better time and energy resolution are used instead of the former Venetian blind type dynodes. With this upgrade, the transit time spread (TTS) is significantly improved from 5.4 ns to 3.1 ns (FWHM). The peak-to-valley ratio is also significantly improved from 1.7 to 3.4.

In KamLAND, a set of compensating coils surround the detector in the cavity in order to cancel the Earth's magnetic field, $\sim 5 \times 10^{-5}$ T. The magnetic field is suppressed well below $\sim 5 \times 10^{-4}$ T, with which the effect on photo electron trajectory inside PMT is less than 20 %.

Figure 3.8 shows the quantum efficiency of KamLAND PMT as a function of the wavelength. A typical value of the quantum efficiency is approximately 20 % at 350 to 400 nm, where PPO light emission peaks.
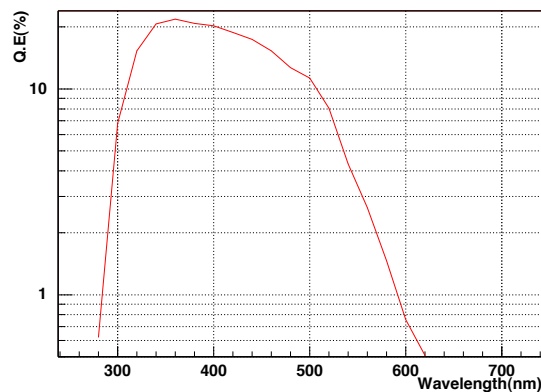
Figure 3.8.: Quantum Efficiency of PMTs

Front-End Electronics

As mentioned, typical PMT signal for a neutrino event is one photo electron signal. Given 5×10^6 gain of PMTs, a photo electron makes 0.8 pC charge output which corresponds to 40 mV×ns when the signal is accepted by 50 Ω termination resistance. Then a typical one photo electron signal has 2.2 mV height and 30 to 40 ns width. A front-end electronics (FEE) hence requires at least a couple of 0.1 mV height resolution. On the other hand, the highest energy event in KamLAND, cosmic muons deposit more than 10,000 photo electrons only in one PMT or more than 1000 photo electrons for all PMTs. For this case, the signal height reaches a few Volts and width a few hundred nano seconds. Considering these two typical types of signals, a FEE needs to manage over 10^4 magnitude of dynamic range.

In KamLAND, event rate of sub MeV events is a few tens Hz for each PMT. On the other hand a FEE needs to record various signals of various time constant. One important signal is delayed coincidence signal of an anti-neutrino event, in which the

delayed event is detected 210 us time constant. A proton decay makes signals 5 events with 2.2 us half-life. A supernova at the center of our galaxy generates 1 kHz high energy neutrinos for a few seconds.

KamLAND FEE, KamFEE diagram is shown in Figure 3.9 and requirements above are satisfied in the scheme in the diagram.
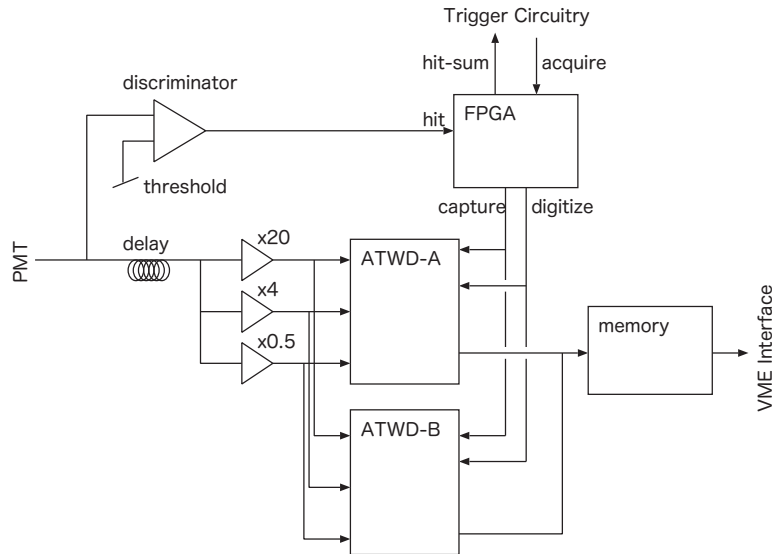
Figure 3.9.: KamLAND Front-End Electronics Diagram

A discriminator introduced in parallel discriminates an input pulse and generates fast 'Hit' and the online FPGA issues 'capture' to an Analog Transient Waveform Digitizer, ATWD chip. The input pulse is divided into 3 different gain, ×20 (High gain), ×4 (Middle gain), ×0.5 (Low gain). The 3 pulses arrive at the ATWD chip a bit later than 'capture' due to the online delay. The ATWD samples waveform of three inputs on its capacitor arrays cyclically and when 'capture' order comes, it stops sampling then holds the current waveform where the input pulse is always included. With this scheme, wide dynamic range and short interval event handling is satisfied.

The online FPGA issues 'Hit-sum' to the trigger circuitry as well as 'capture' to an ATWD. The trigger circuitry issues back 'acquire' to the FPGA when it discriminates total 'Hit-sum' in a specified time window, and decides to acquire an event including the pulse. Then the FPGA issues 'digitize' to the ATWD, and finally the ATWD starts to digitize the waveform. It takes approximately 25 us for digitizing 10-bit 128 samples, and during the period the ATWD does not accept a new waveform, instead, the other online ATWD accepts the new waveform. With this scheme, the delayed coincidence events of anti-neutrinos are surely acquired. Once the digitization is done, the waveform is transferred to the on board memory and then to a DAQ computer via the VME interface. When an ATWD have waited 'digitize' for 1 us since it accepted 'capture' and started to hold a waveform, it discards the waveform.

An ATWD works with configurable clock of interpolated on board clock (40 MHz).

The typical sampling interval is approximately 1.5 ns and this is calibrated by the on board 40 MHz sinusoidal waveform generator at the very beginning of daily data taking.

Finally Figure 3.10 shows a picture of a KamLAND FEE card and its layout.
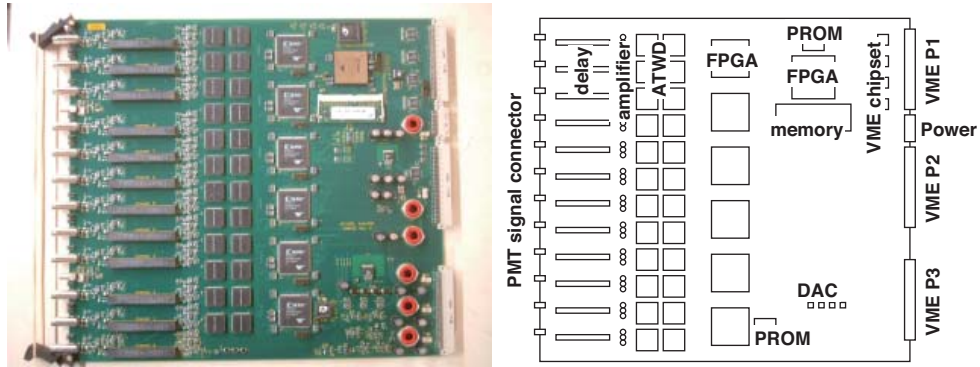
Figure 3.10.: KamLAND Front-End Electronics

Trigger System

Trigger decisions are made based on the number of hit PMT's, told as 'Hit-sum' within a certain time window. Each PMT hit signal is stretched to a 125 nsec long gate, and digital sum of the gates, 'NSum' is computed at the trigger circuitry. Most of the physics trigger is based on this 'NSum' and once the 'NSum' exceeds a preset threshold, an ' acquire ' command is sent to the FEE cards.

Figure 3.11 shows a schematic diagram of the trigger subsystem. The trigger circuitry
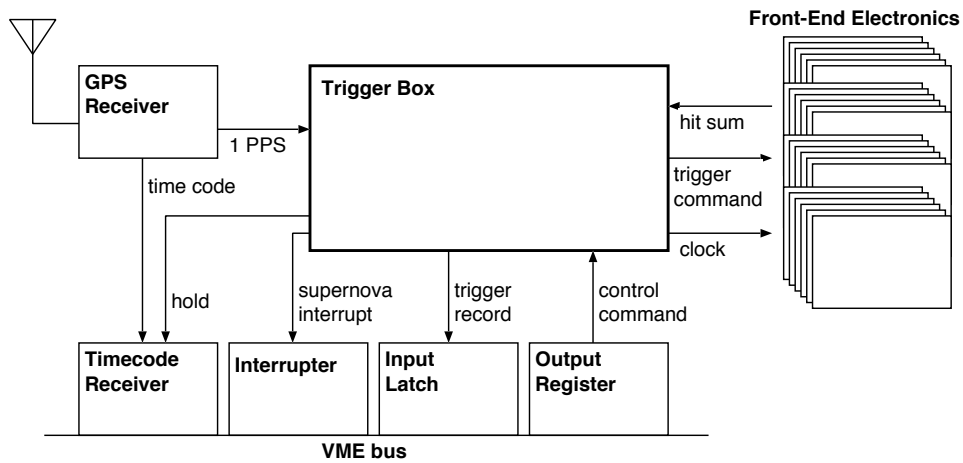
Figure 3.11.: KamLAND Trigger Circuitry

receives PMT hit signals from every FEE card, and sends various trigger commands

to the FEE. The trigger commands include the 'acquire' commands that command to acquire waveforms, the calibration commands that command to perform self-calibration (with the built-in test pulser and 40 MHz clock signal etc.), and some other control commands such as initialization. Some trigger types (e.g. History trigger) do not involve acquire signals to the FEE, but the 'NSum' and timestamp are recorded by the trigger circuitry. These types of trigger is better at study of sub-threshold events.

A Global Positioning System (GPS) receiver is connected to the trigger circuitry and all time information used in the system is synchronized to the GPS time. The trigger circuitry also provides the 40 MHz system clock, synchronized to the GPS, to the FEE cards. Event timestamp is generated with this 40 MHz clock and is added to every waveform,

The most important trigger in normal physics data taking is ID Prompt trigger. With the background reduction by the 2nd purification, 'NSum' threshold is lowered down to 70, which roughly corresponds to more than 70 ID PMT hits. Following every prompt trigger, the delayed trigger is enabled for 1 ms, which is issued when the 'NSum' excesses 70. Previously, this trigger is meant to improve detection efficiency of timely correlated multiple signals, such as cascade decays, there is no longer such superiority in this setting now. Another important trigger for physics run is the ID Prescale trigger, whose 'NSum' threshold is 50. This trigger also involves 'acquire' commands and only is issued within 10 ms after a 1PPS trigger in order no to make so huge data flows. Another important trigger for physics run is the OD-to-ID trigger, which is issued when any of OD segment detects certain number of photons, which is used for event veto.

Figure 3.12 shows a ID Single Prompt/Delayed trigger efficiency. The efficiency is evaluated as the ratio of the number of those triggers to the number of ID Prescale triggers in ID Prescale trigger window (i.e. 10 ms since 1PPS trigger). 99.9 % efficiency is achieved at 0.38 MeV $< E$. In the visible energy histograms in this thesis, events taken by ID Single Prompt/Delayed triggers are only used above the energy, and events taken by ID Prescale triggers are used below the energy, while the event rate there is scaled by calibrated ratio of Prescale trigger window, which is ideally 1 s / 10 ms.

3.2.4. Calibration Equipment

For detector calibration, various radioactive sources are deployed in the ID. There are two deployment devices, one is called MiniCal for z-axis calibration and the other is called 4π for off-axis full volume calibration.

"Z-axis" calibration device deploys radioactive sources to arbitrary points along the detector's z-axis by an encoded pulley and a teflon coated stainless steel cable. The deployment is done from the a glove box located atop of the detector through the Chimney. During the calibration, nitrogen gas is supplied to the glove box to prevent the in-flow of Rn.

"Off-axis" calibration device is shown in Figure 3.13. It consists of control cables, several poles, calibration source, and deployment system. Each pole has a pin source at the one edge and the pivot block also has a pin source. These pin source are ^{60}Co and prepared for monitoring of the position. Main calibration source is located at the
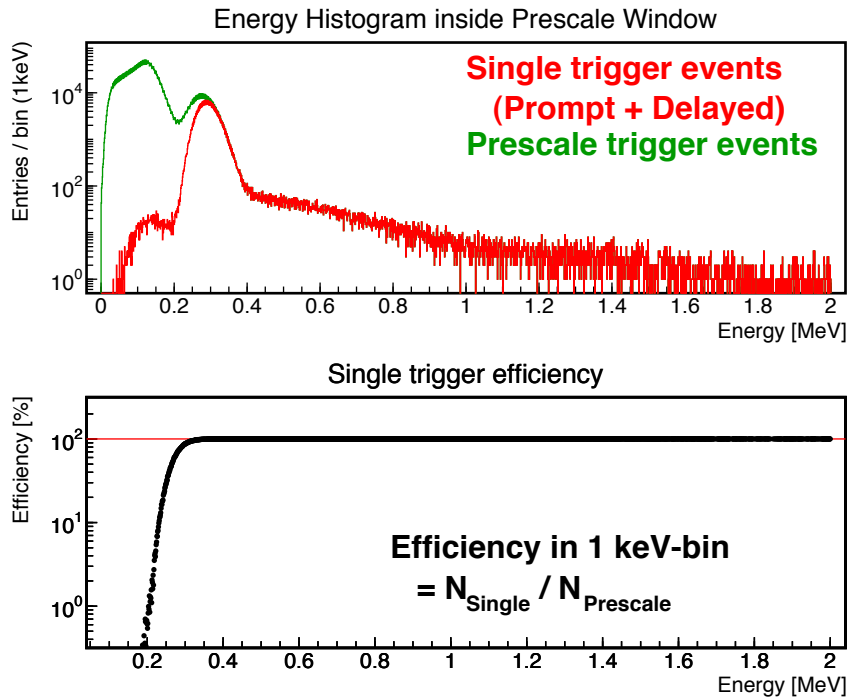
Figure 3.12.: Single Prompt Trigger Efficiency. The ratio of the number of Prompt and Delayed triggers to the number of Prescale triggers is larger than 99.9 % at 0.38 MeV$< E$.

end of poles. With the cables, the poles and the pivot block, the main source can be deployed any coordinates of the detector. Figure 3.14 shows how the deployment system controlled. During insertion (1) or retraction (6), the pole is set vertical, during calibration (2)–(5), the pole is tilted so that the main source can be deployed everywhere.

The radioactive sources used for the calibrations are summarized in Table 3.2.
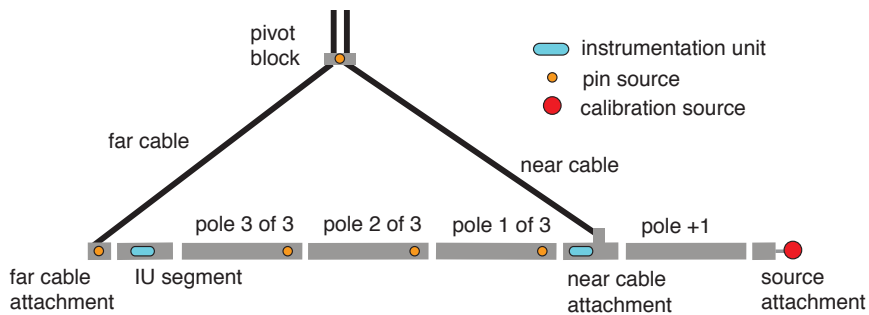
Figure 3.13.: Schematics of off-axis calibration system. (Berger et al., 2009)

42
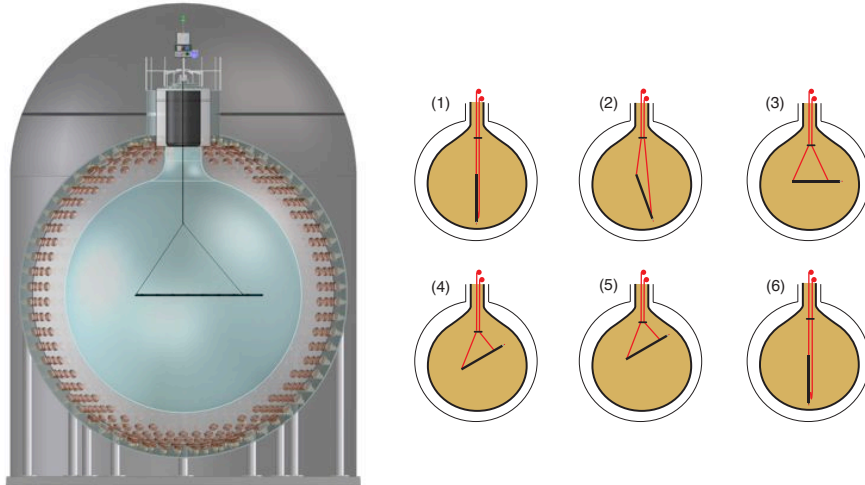
Figure 3.14.: Deployment of off-axis calibration system. (Berger et al., 2009)

Table 3.2.: Calibration Sources

Source	Visible Particle	Real Energy [MeV]	Calibration
^{203}Hg	1 γ	0.2792	z
^{7}Be	1 γ	0.4776	z, off
^{85}Sr	1 γ	0.5140	z
^{137}Cs	1 γ	0.6617	z, off
^{68}Ge	2 γ	0.511×2	z, off
^{60}Co	2 γ	1.173 + 1.133	z, off
^{241}Am^{9}Be	neutron, γ	neutron + 4.438	z, off

4. Event Reconstruction and Detecter Calibration
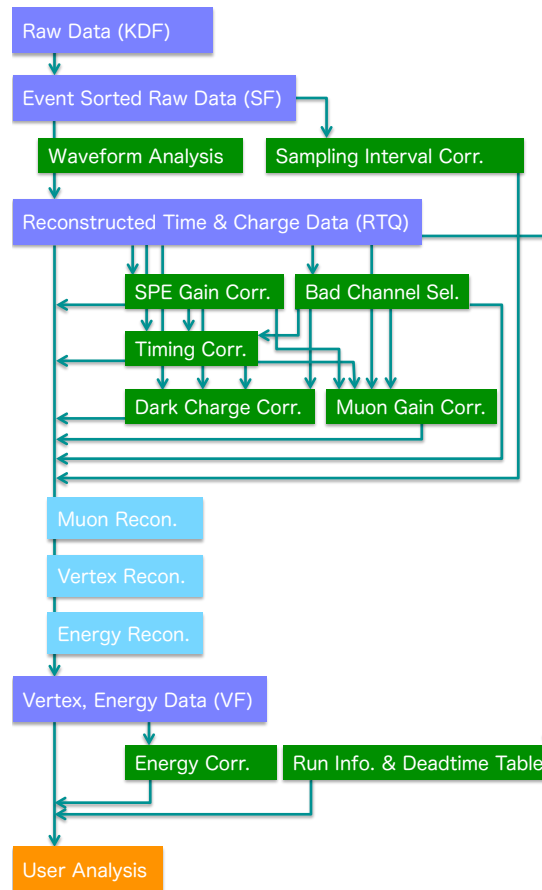
Figure 4.1.: Event Reconstruction Procedure

Event reconstruction process is mainly composed of waveform analysis, parameter correction and vertex and energy reconstruction. In this chapter, all most all of the components in Figure 4.1 except for Run Info and Deadtime Table is described.

4.1. Waveform Analysis

4.1.1. Pedestal Calculation

A waveform from an ATWD consists of 128 samples. The i-th sample of a waveform always is converted into ADC value from electrical charge, which is stored in the i-th capacitor of a capacitor array inside the ATWD. Thus, the characteristics of the i-th electronic circuitry affects every i-th sample. The value of the i-th sample from a waveform without pulses is called "Pedestal" of the i-th sample. Compensation of the effect of the pedestal of every sample of a waveform is called "Pedestal Subtraction".

Waveforms for analysis of Pedestal are acquired at the beginning of every run. 50 waveforms are acquired for every H, M and L gain channel of every A and B ATWD channel with the triggers, Acquire Trigger [pedestal acquisition A (or B)]. Additional 50 waveforms are also acquired for every H gain channel of every A and B ATWD channel with the triggers, Acquire Trigger [forced acquisition A (or B)]. Good waveforms are selected with the following criteria,

- (Any pulse height) < (1 p.e. discrimination threshold)
- (Difference between any adjacent samples) < (40 samples)
- (Difference between maximum and minimum of a waveform) < (50 ADC count)

A Pedestal waveform is acquired by averaging every set of i-th samples from these waveforms.

4.1.2. Baseline Calculation

The analog zero volt level, "Baseline" could be distorted by previous pulses. For example a muon event deposits very high charge in the detector and induces very large electric current in a PMT electronic circuitry then invokes overshoot backward. In order to compensate such long term variation of baseline, we analyze baseline for every waveform with following procedure, then subtract the acquired baseline value from the waveform.

1. Subtracting Pedestal from a waveform.
2. Getting height of a waveform as difference between the maximum and minimum of the moving average of a waveform
3. Choosing samples by comparing the value of them and the gradient at them with the height
4. Getting average over the chosen samples

An example Pedestal and baseline analysis is shown in Figure 4.2.
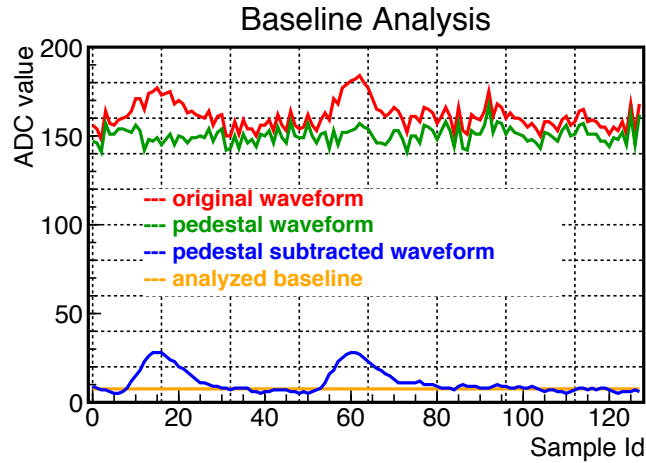
Figure 4.2.: An example baseline analysis of a waveform. "Pedestal subtracted wave-
form" (blue) is derived by subtracting "Pedestal waveform" (green) from
"Original waveform" (red). "Baseline" (yellow) is derived from "Pedestal
subtracted waveform"

4.1.3. Waveform Analysis

After the subtraction of Pedestal and baseline, extraction of mean component of a
pulse from a waveform is possible, then important parameter set of a pulse, timing and
charge is analyzed.

In a waveform, at first peaks are identified by their height and derivative. Then for
each peak, the start and end points are analyzed from height, derivative, and distance
from the peak and adjacent peaks. The charge of the peak is acquired as sum of ADC
counts of smoothed waveform between the start and end points.

Originally, multi peak analysis is done and acquired time and charge is called MultiTQ.
In this analysis, mainly time of the first pulse and total charge of pulses in a waveform,
SingleTQ is used. An example waveform analysis is shown in Figure 4.3.

4.1.4. Sampling Interval

An ATWD chip regenerates interleaved overlapping high frequency clock from the
board level clock (40MHz) for Sample-and-Hold of an input analog waveform. This
regeneration is configured by input electrical current applied into Trigger Bias pin on
the chip. While the 40MHz board level clock could be calibrated with information of
absolute timing of GPS signals, the sampling interval uncertainty due to the regeneration
should be calibrated differently.

In order to calibrate the regenerated clock, 40MHz sinusoidal waveform from an on-
board oscillator is input to an ATWD chip on the board and 50 waveforms are acquired
at the beginning of DAQ for both A and B channel with Clock Acquisition A or B
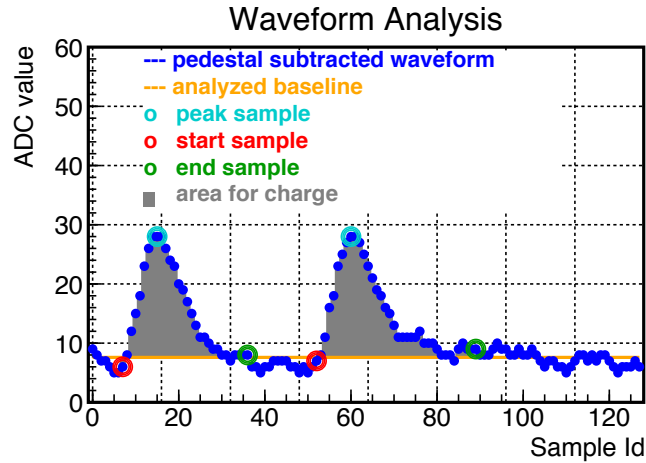
Figure 4.3.: An example of waveform analysis. A "Peak sample" is identified "Pedestal subtracted waveform" (blue) by analyzing the height at the sample from the "Baseline" (yellow) and the derivatives at the sample. Then "Start sample" (red) and "End sample" are searched from the "Peak sample". A charge is evaluated as sum of "Area for charge" (gray).

triggers.

After rejecting a waveform including a PMT pulse, the number of sinusoidal pulse is analyzed and then mean sampling interval is analyzed. An example sampling interval analysis is shown in Figure 4.4.

Time variation of sampling interval for each type of PMTs is shown in Figure 4.5 It is steadily increasing, although there are several jumps related to electronics or detector modification. The average sampling interval of ID PMTs during the analysis of this thesis is approximately 1.505 ns, which is interpreted that the length of one ATWD waveform is approximately 192.5 ns.

4.2. SPE Gain

Gain is defined as the ratio of charge of a single photo electron (SPE) pulse at a time to that at Jan. 2004. Since charge is calculated as area of a pulse, it can be affected by variation of electrical current gain on PMT and ATWD as well as by variation of sampling interval at ATWD.

4.2.1. 17 inch PMT

SPE pulses on the ATWD channel for a 17 inch PMT are selected with following criteria,

- Event selection
    - muon events veto

47
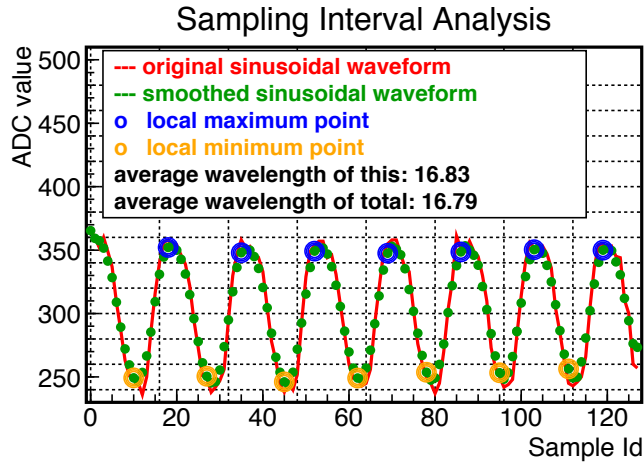
Figure 4.4.: Example of sampling interval analysis. "Local maximum point" (blue) and "Local minimum point" (orange) are selected from "Smoothed sinusoidal waveform". "Average wavelength of this" is evaluated by dividing sum of distance of "Local maximum point"s and of distance of "Local minimum point"s by the number of interval of them. "Average wavelength of total" is evaluated by averaging "Average wavelength of this" over 50 sinusoidal waveforms.

- − 2 msec veto after muon events
- − 100 usec veto after every events
- − 120 < (total HITs of all ATWD channels for 17 inch PMTs) < 230
- Pulse selection
  - − 1 peak in a waveform
  - − (distance between event vertex) > (5.5 m from location of the PMT)

After the selection of above, the charge of a SPE pulses is defined as the center of Gaussian formula fitted to the distribution of the charge of the selected pulses as shown in the left graph of Figure 4.6.

4.2.2. 20 inch PMT

Extracting Gaussian-shape like SPE charge distribution for a 20 inch PMT channel is difficult as shown in Figure 4.6 due to the difference of the dynode of the PMT. Then the relative gain of a 20 inch PMT channel is evaluated by comparing the charge of a event in the channel, Q_{20} with average gain-corrected charge of the neighboring eight 17 inch PMT channels, Q_{17}. Event selection for the comparison is as follows.

- muon events veto
- (distance from the 20 inch PMT to the reconstructed muon track) > 1.4 m

48
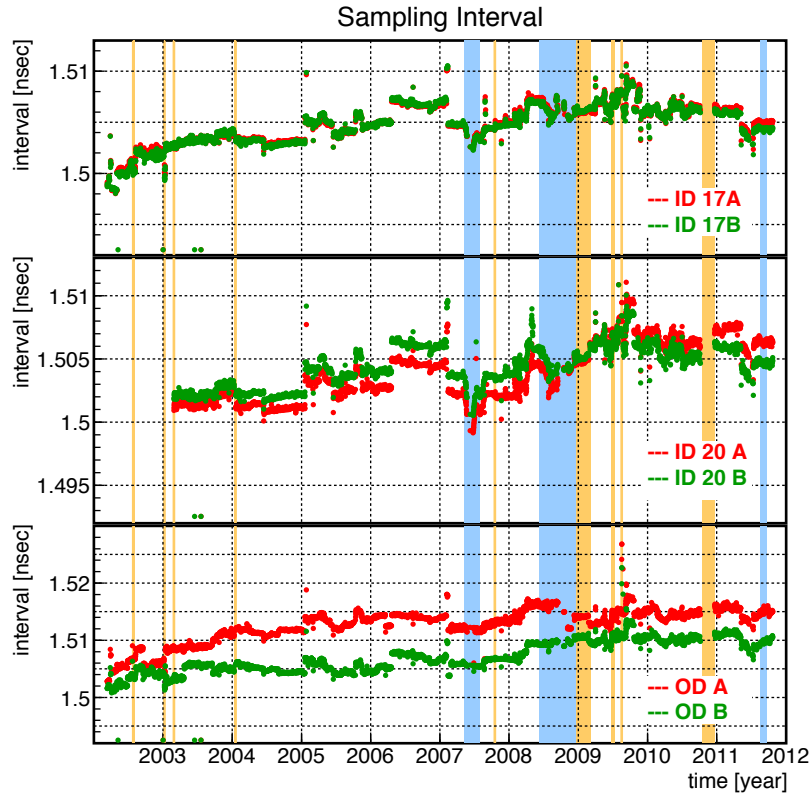
Figure 4.5.: Time variation of sampling interval. The top graph shows the trend of the ID 17-inch PMTs, the middle the ID 20-inch PMTs, and the bottom the OD 20-inch PMTs. The blue bands show periods when there were remarkable detecter modification works such as the liquid scintillator purification. The orange bands show periods when there were remarkable electronics modification works such as the ATWD updates.

- $300 < Q_{17} < 5000$

Then, the relative gain of the channel, G_{20}, is defined as, $G_{20} = (Q_{20} / S_{20}) / (Q_{17} / S_{17})$, where S_{20} and S_{17} means the area of the acceptance surface of a 20 and 17 inch PMT respectively.

The SPE gain of the 17-inch PMTs and the relative gain of the 20-inch PMTs are steadily increasing except when there is operation for HV or ATWD as seen in sampling interval trend.

4.3. TQ Map

Interval between the timing of light emission inside the detector and the timing of the start time of the pulse in a waveform is different for each channel and is different for
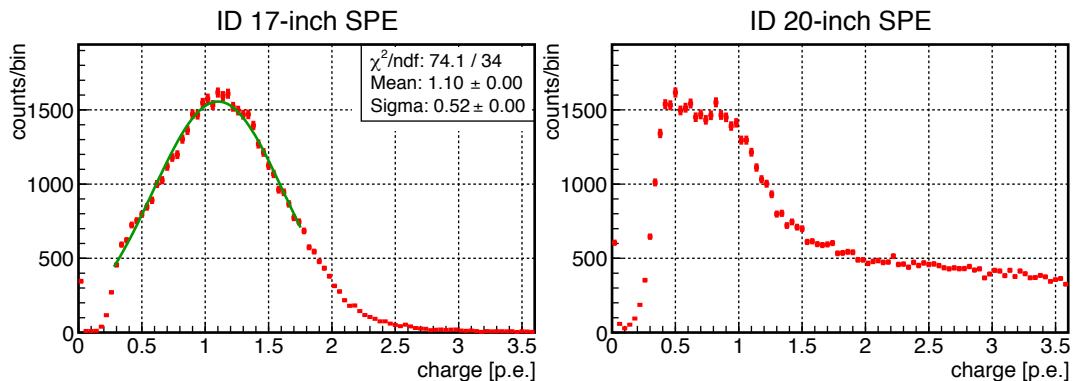
Figure 4.6.: Typical SPE distribution. Charge distribution of selected pulses in a ATWD channel in a run is shown. In the left graph, 17-inch PMT charge distribution is fitted with Gaussian formula and the mean value 1.1 is the relative gain of this channel in this run.

various pulse size. The main differences inducing this difference are following,

- Distance from a light emission position to a PMT surface.
- Signal processing time inside the electronic circuitry.
- Cable length between the PMT to an ATWD channel.
- Slewing effect from waveform analysis.

These difference must be well calibrated so as to reconstruct event position.

4.3.1. Laser calibration

In order to calibrate these effects, calibration DAQ was performed at earlier time of KamLAND DAQ in May 2004. In the measurement, light from a laser was introduced to the center of KamLAND via a fiber optic cable to a light diffusion ball hanged there, in order that uniform-intense light is delivered to all PMTs. DAQ was done with various light intensity from 1 to 10^4 of SPE level for each channel. Result of the measurement for each channel is fitted with following function.

$$T = T_0 + T_1 \cdot \log_{10} (\text{ADCsum}) + T_2 \cdot \log_{10} (\text{ADCsum})^2, \tag{4.1}$$

where ADCsum is sum of ADC value acquired with waveform analysis. Channel by channel T_0 is shown in Figure 4.8.

4.3.2. BLR extension correction

BLR installation induced additional delay for KamLAND DAQ by extending signal cables between PMTs and ATWD channels. The extension is classified in to 5 types by the type of PMTs and by the location of the VME crate of the PMTs. Those types are summarized in Table 4.1.
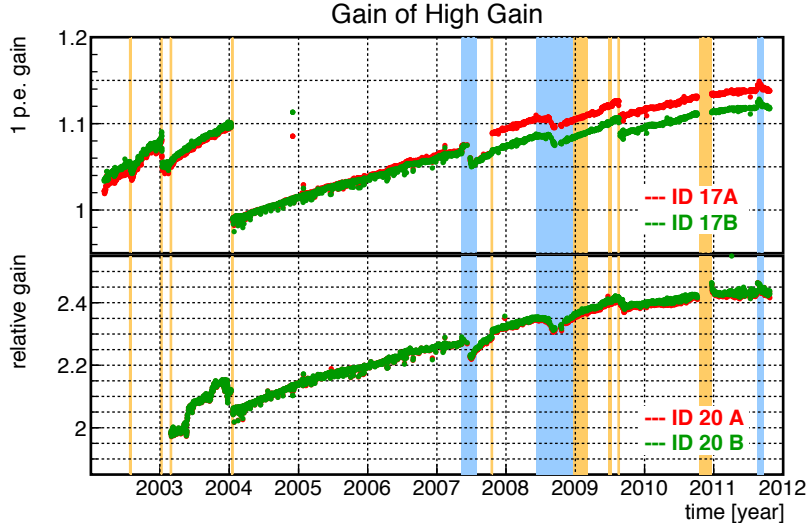
Figure 4.7.: Time variation of Gain. The top graph shows 17-inch SPE gain trend and the bottom 20-inch relative gain. The colored bands are the same as those in Figure 4.5.

Table 4.1.: Types of cable extension and delay due to BLR installation

delay [nsec]	length [m]	channel
2.4	0.44	ID 20 inch, in the upper VME crates
9.9	1.50	ID 20 inch, in the lower VME crates
8.4	1.92	ID 17 inch, in the upper VME crates
23.4	4.43	ID 17 inch, in the lower VME crates
-	-	OD 20 inch

4.3.3. Time Dependence correction

In addition to the two identical data from laser calibration and BLR cable extension, run-dependent delay for each channel is calculated. Precise timing $T_{\text{run base}}$ for each run for each channel is calculated by comparing timing difference between the channel and the others. The same process is performed for source calibration data for ^{60}Co

51
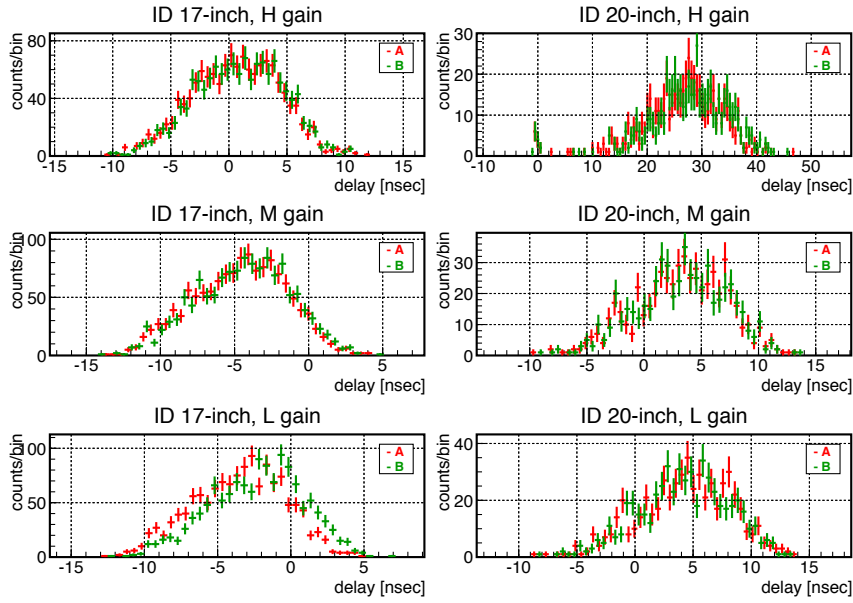
Figure 4.8.: Constant delay T_0 of all channels, measured by laser calibration.

source located at the center of the detector in order to calibrate the time variation, and evaluated value $T_{^{60}\text{Co}}$ is applied to near normal run. Reference ^{60}Co calibration is summarized in Table 4.2.

Table 4.2.: Reference ^{60}Co source calibration run for Time Dependence correction

Period			^{60}Co run	Period			^{60}Co run	Period			^{60}Co run
9088	–	9248	9137	9527	–	9618	9527	9948	–	9971	9948
9249	–	9292	9249	9619	–	9648	9619	9972	–	10073	10017
9293	–	9319	9293	9649	–	9678	9649	10074	–	10190	10074
9320	–	9395	9320	9679	–	9784	9679	10191	–	10315	10191
9396	–	9489	9396	9785	–	9791	9785	10316	–	10678	10316
9490	–	9526	9490	9792	–	9947	9846				

Finally, timing correction function is defined for each channel of each run as follows.

$$T_{\text{correction}} = T_{\text{run-basis}} + T_{^{60}\text{Co}} + T_{\text{cable-extension}} \tag{4.2}$$
$$+ T_0 + T_1 \cdot \log_{10} (\text{ADCsum}) + T_2 \cdot \log_{10} (\text{ADCsum})^2.$$

4.4. Bad Channel

Signal acquisition quality on each channel varies according to time due to failures or

problems of electrical components such as PMTs, HVs, cables and ATWDs. Channels with low quality should be unmasked for keeping event reconstruction quality.

There are 7 criteria for ID channels, and one for OD channels.

ID criteria:

1. Small number of hits (N) within the first 10000 events

$$
\begin{array}{ccccccc}
N & < & 1000 & (& & \text{run} & < & 8649\ ) \\
N & < & 800 & (\ 8640 & \leq & \text{run} & < & 9627\ ) \\
N & < & 600 & (\ 9627 & \leq & \text{run} & &)
\end{array}
$$

2. No hit within the first 10000 events

3. Large hit rate difference between A and B channel within the first 10000 events

$$
\left| 1 - \frac{(\text{Hit rate at B})}{(\text{Hit rate at A})} \right| > 0.22 \tag{4.3}
$$

4. Small number of hits ($N < 400$) with muon veto within the first 10000 events

5. Small number of hits ($N < 80$) for the first 100 high energy muon events

6. High charge bias for the first 100 high energy muon events

$$
\frac{1}{N} \sum_i^N \frac{(\bar{Q}_i - Q_i)^2}{\bar{Q}_i} > 400\ (> 1000\ \text{for}\ \ \text{run} \geq 10626) \tag{4.4}
$$

$(\bar{Q}_i$: average charge over neighboring 17-inch channels$)$

7. SPE charge, Q_{SPE}, derived via Gain calibration is much lower or much higher than the designed value, Q_{designed}.

$$(Q_{\text{SPE}} < 0.4 \cdot Q_{\text{designed}}) \cup (4 \cdot Q_{\text{designed}} < Q_{\text{SPE}})\ \text{for ID 17-inch}$$
$$(Q_{\text{SPE}} < 0.4 \cdot Q_{\text{designed}}) \cup (6 \cdot Q_{\text{designed}} < Q_{\text{SPE}})\ \text{for ID 20-inch}$$

OD criteria:

1. Small number of hits ($N < 5$) within the first 10000 events

The trend of the number of bad channels is shown in Figure 4.9.

4.5. Dark Energy

The charge of accidental HITs, which is called "dark charge", contributes the energy of each event. For estimating this contribution, the charge is calculated from off-time window of each event. The run-specific value, "dark charge" is used for energy estimation, and the cable-specific value, "dark ring" is used for vertex reconstruction.
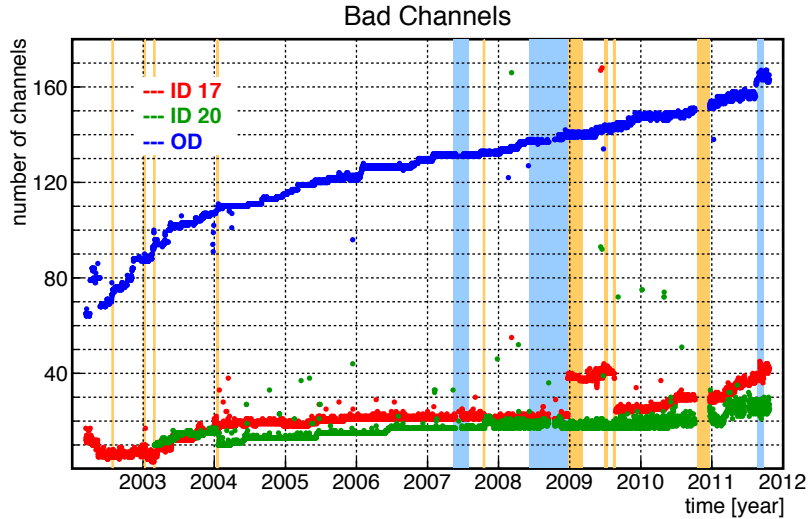
Figure 4.9.: Time variation of bad channel. The colored bands are the same as those in Figure 4.5.

dark charge

Dark charge is derived with following procedure.

1. Select events locating less than 2 m from the center of the detector whose vertex is given by vertex fitting with only 17-inch PMTs after vetoing GPS trigger event, muon events and 2 ms after the muon events.

2. Setting "off-time" window in TOF subtracted time spectrum from the -100 ns to -50 ns from the start timing of 50 ns in which the number of hits peaks as shown in Figure 4.10.

3. Getting the mean of the total charge of 17-inch PMTs inside the off-time window.

dark ring

Dark ring is derived with following procedure.

1. Select events locating less than 2 m from the center of the detector whose vertex is given by vertex fitting with all PMTs after vetoing GPS trigger event, muon

events and 2 ms after the muon events.

2. Setting "off-time" window in TOF subtracted time spectrum from the -100 ns to -50 ns from the start timing of 50 ns in which the number of hits peaks as shown in Figure 4.10.

3. Getting channel-by-channel mean charge inside the off-time window of all events.
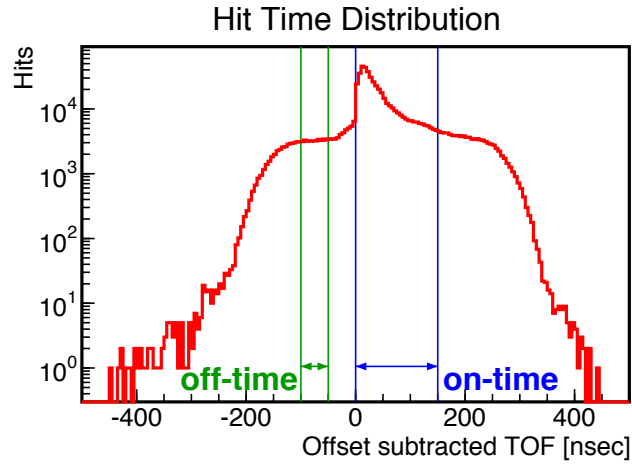
Figure 4.10.: Hit time distribution of a typical one day run.

The dark charge is basically related to the temperature inside the detector (Shimizu, 2004:p64), and is stable and less than 10^{-4} p.e. per channel during this analysis period as shown in Figure 4.11.
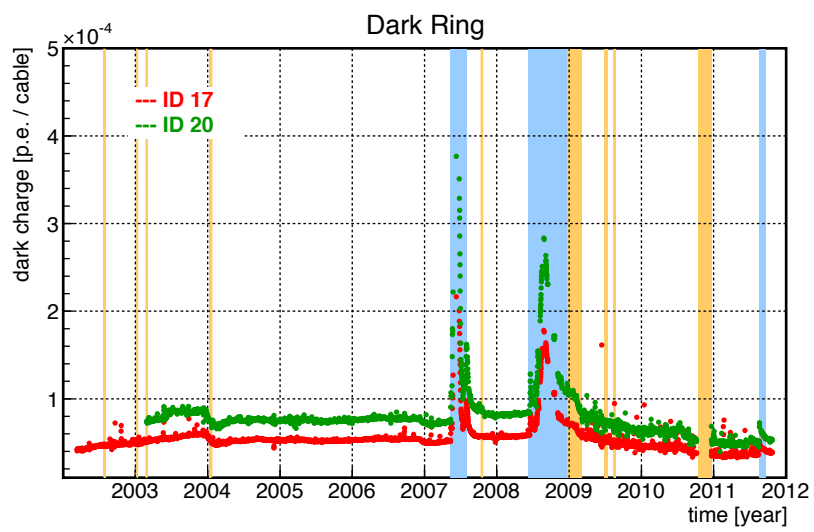
Figure 4.11.: Time variation of dark charge. The colored bands are the same as those in Figure 4.5.

4.6. Muon Reconstruction

Muons and spallation products induced by the muons are sources of background for a neutrino detector. The detector, KamLAND is located beneath the mountaintop of Ikenoyama, and the vertical overburden of KamLAND is approximately 1000 m of rocks, which corresponds to that of 2700 m water equivalent. With the shielding against cosmic rays, approximate cosmic muon rate observed with KamLAND is 10^{-5} of that observed at the ground level. However, muons passing through the rocks still induces finite amount of spallation products. In order to distinguish those spallation products, exact muon track must be reconstructed.

4.6.1. Selection Criteria

Muons are easily identified inside KamLAND with large energy deposit via one or some of the following process; water Cherenkov light yield process inside the outer detector (OD), Cherenkov light yield process inside the buffer oil (BO), scintillation and Cherenkov light yield process inside the liquid scintillator (LS).

Distribution of number of OD hit, N_{200OD} and total charge sum of the 17 inch PMTs in the inner detector, Q_{17} is shown in the left graph of Figure. 4.12. There are two clusters at higher Q_{17}, around $10^{4.5}$ and $10^{5.5}$ respectively. The cluster with the lower Q_{17} consists muons which do not enter LS and yield only Cherenkov light. Those muons are called "clipping muons". The cluster with the higher Q_{17} consists muons which enter LS and yield scintillation and Cherenkov light. Those muons are called "through going muons". These cluster are also obvious in the right graph of Figure. 4.12.
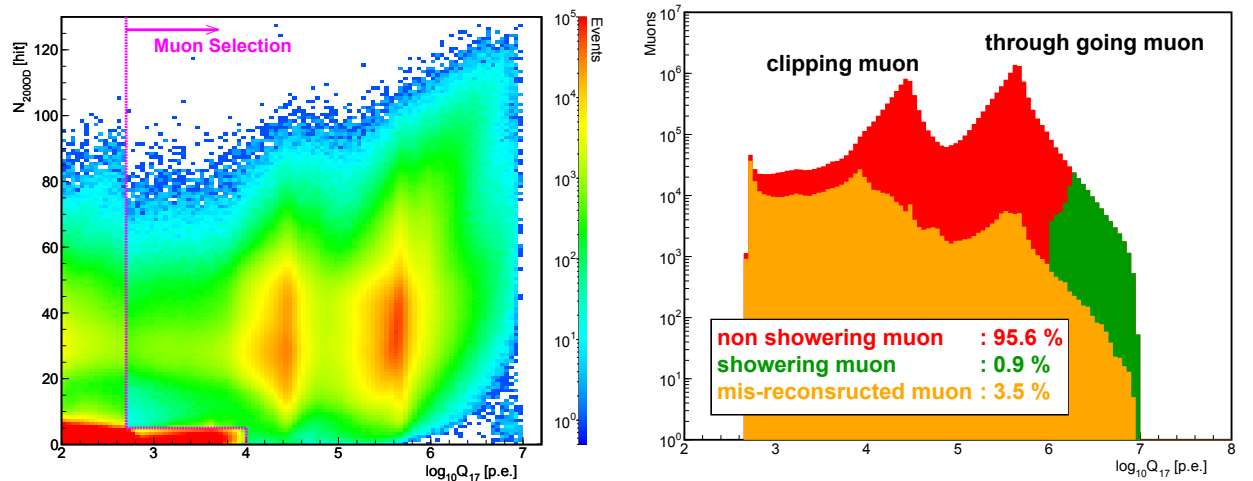
Figure 4.12.: Correlation of OD hit and ID 17-inch PMT charge is shown in the left.

In order to select each type of muons, following selection criteria is specified.

- $Q_{17} \geq 10,000$ p.e.   ; for "through going muons".
- $(Q_{17} \geq 500$ p.e.$) \cap (N_{200OD} \geq 5$ hits$)$; for "clipping muons"
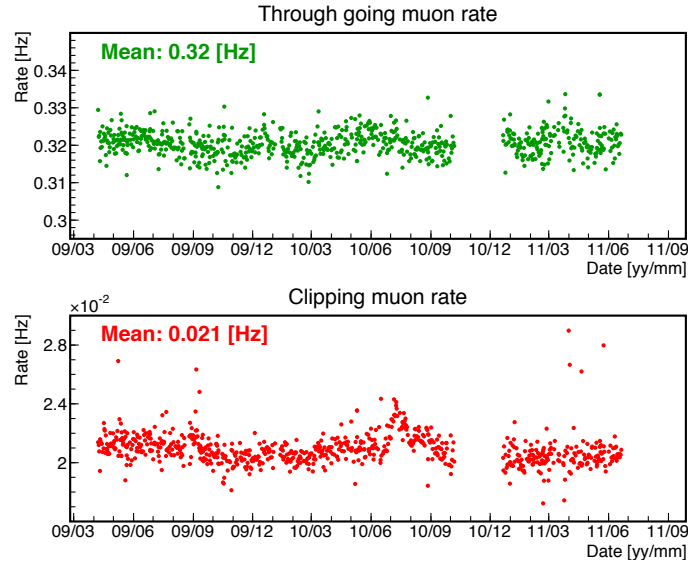
Figure 4.13.: Muon event rate for two types of muon.

The mean muon rate for "through going muons" and "clipping muons" are measured to be 0.32 Hz and 0.021 Hz, respectively as shown in Figure. 4.13. Total muon rate is then 0.34 Hz and found stable during the analysis period.

4.6.2. Algorithm for muon track reconstruction

In the inner detector of KamLAND, Cherenkov photons from BO and/or LS, and/or scintillation photons from LS from a muon track are observed.

Cherenkov photons are emitted at an angle of fixed degree, Cherenkov angle (θ_C) respect to the muon track. This angle is related to the index of refraction (n) of LS and BO 1.44 ∼ 1.47 and 1.43 ∼1.46 respectively and presented as $\cos \theta_C = 1/n$.

On the other hand, scintillation photos are emitted isotropically from each point of the muon track. Now we consider the path of the earliest photon arriving at a PMT, horizontally located ρ and vertically located z distance from the muon track in the muon track frame. The interval (ΔT) between the muon enters LS and the earliest photon arrives to the PMT is the sum of the duration the muon runs before emitting the photon and the duration the photon runs. When the photon is emitted at an angle of θ_s respect to the muon track, ΔT is represented as follows,

$$\Delta T = \frac{z - \rho/\tan \theta_s}{c} + \frac{\rho}{\sin \theta_s \ c/n}, \tag{4.5}$$

where the muon runs at the speed of light (c). Then $\cos \theta_s$ which gives minimum ΔT is derived by $d\Delta T/d\theta_s = 0$, as $\cos \theta_s = 1/n = \cos \theta_C$.

This coincidence allows simplification on the muon tracking algorithm, that is using only hit timing of earliest photons on each PMT for the reconstruction. The refractive

index and the position dependent speed of light parameterization is introduced to take account of the difference of refractive index in LS and BO and its effect on the different path length in each medium.

When the energy deposit of the muon is too small, the muon stops inside the detector, or multiple muons enter the detector, this algorithm is not appropriate and the reconstructed tracks are not reliable. Those muons are classified as "mis-reconstructed muons". The fraction of these muons are 3.5% of total muons, as in the right graph of Figure.4.12.

4.6.3. Tracking performance

In Figure.4.14, correlation between Q_{17} and the impact parameter, which is minimum distance from the KamLAND center to a reconstructed muon track is shown for well reconstructed muons. The obvious edge of KamLAND balloon divides two typical energy structure from "through going muons" and "clipping muons" in LS and BO respectively, as seen in Figure.4.12.
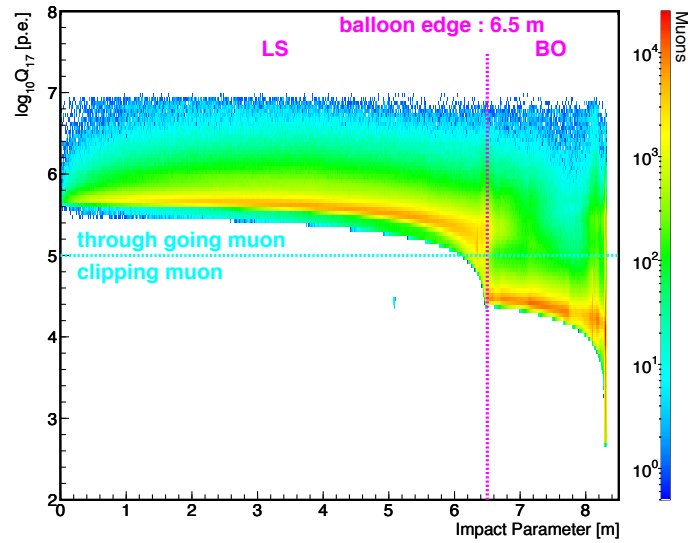
Figure 4.14.: ID charge and impact parameter

The upper two graphs in Figure.4.15 show correlation between Q_{17} and the track length of reconstructed muons in each medium for well reconstructed muons. Obvious linearity between the two parameters indicates energy deposit due to minimum ionization of muons and also indicates validity of reconstruction. High energy muons accompany more secondary events by spallation products and deposit much higher energy. Those muons appear in Figure.4.15 above the linear trend, that is, higher Q_{17} over unit track length. In order to tag those muons, "residual charge" (ΔQ), which is defined by

following equation,

$$\Delta Q = Q_{17} - L_{\mathrm{BO}} \left(\frac{dQ}{dX}\right)^{\mathrm{ideal}}_{\mathrm{Cherenkov}} - L_{\mathrm{LS}} \left(\frac{dQ}{dX}\right)^{\mathrm{ideal}}_{\mathrm{scintillation}} \tag{4.6}$$

is used and selection criterion for those muons is $\Delta Q > 10^6$. In the equation above, L_{BO} is muon track length inside BO, L_{LS} is muon track length inside LS and $(dQ/dX)^{\mathrm{ideal}}$ parameters are defined and evaluated as follows using muons in the very earlier KamLAND runs.

$$\left(\frac{dQ}{dX}\right)^{\mathrm{ideal}}_{\mathrm{Cherenkov}} = \frac{Q_{17}}{L_{\mathrm{BO}}} = 31.45 \text{ p.e. / cm} \tag{4.7}$$

$$\left(\frac{dQ}{dX}\right)^{\mathrm{ideal}}_{\mathrm{scintillation}} = \frac{Q_{17} - L_{\mathrm{BO}} \left(\frac{dQ}{dX}\right)^{\mathrm{ideal}}_{\mathrm{Cherenkov}}}{L_{\mathrm{LS}}} = 629.4 \text{ p.e. / cm} \tag{4.8}$$

For evaluating $(dQ/dX)^{\mathrm{ideal}}_{\mathrm{Cherenkov}}$, only clipping muons are used.
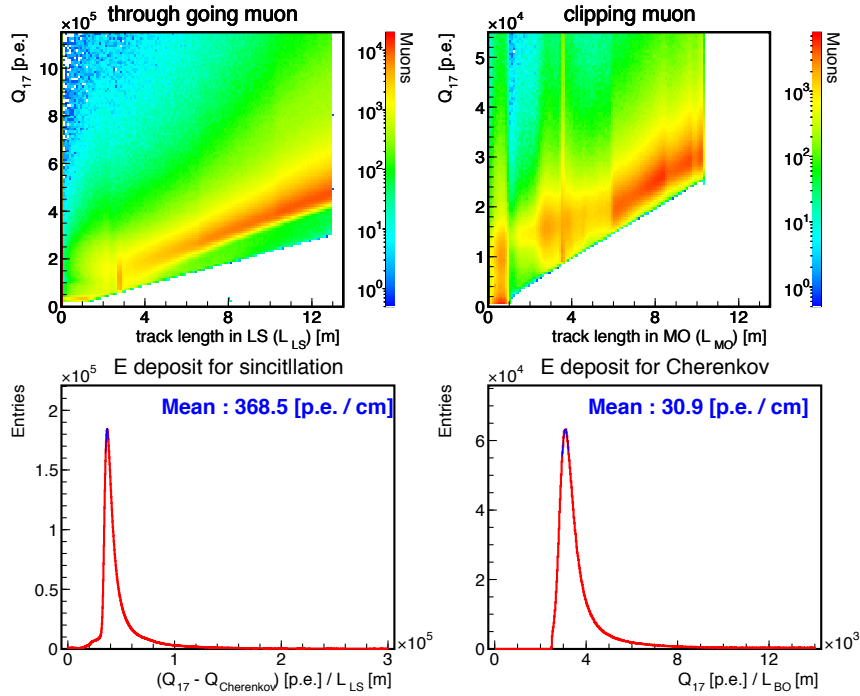
Figure 4.15.: ID charge and impact parameter

Muon Gain correction

Before tracking, calibration of the key parameter Q_{17} is performed. Figure 4.16 shows the time variation of mean Q_{17} of clipping muons and through going muons, which is

evaluated by the right graph of Figure 4.12. Q_{17} of the both types of muons decreased during the purification of the liquid scintillator. The decrease of the difference between them indicates that $(dQ/dX)_{\text{scintillation}}$ much decreased from $(dQ/dX)^{\text{ideal}}_{\text{scintillation}}$. Indeed, the latest $(dQ/dX)_{\text{scintillation}}$ shown in the bottom left graph in Figure 4.15 gets approximately 60 % of the ideal value in the very beginning of KamLAND. Q_{17} is corrected so that Q_{17} of clipping muons is stable among time.
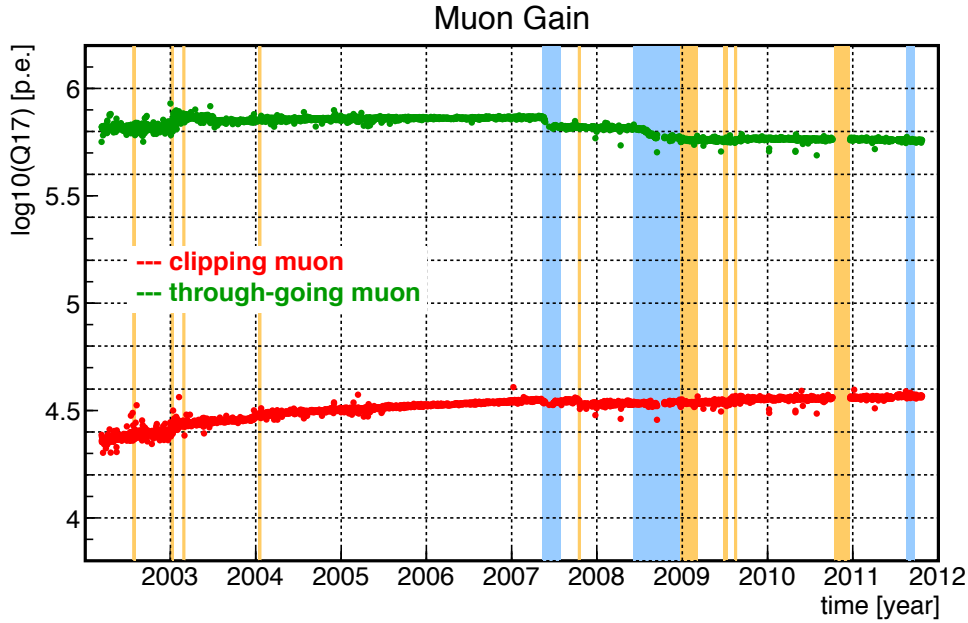
Figure 4.16.: Time variation of Q_{17}. The colored bands are the same as those in Figure 4.5.

4.7. Vertex reconstruction

The reconstructed position of a point-like event is called vertex. This fundamental parameter is used for energy reconstruction and various analysis. Thus reconstruction biases affect position-based or energy-based event selection. The reconstruction algorithm, quality and bias is discussed. Prior to the reconstruction, all the correction described above, sampling interval correction, bad channel selection, gain correction, timing correction, dark hit correction, and muon gain correction are applied to the raw time-charge data.

4.7.1. algorithm

The reconstruction is based on the relative time distribution of hit timing of PMTs.

Abstract estimation of vertex is done by "KatLTVertex fitter" with only hit timing. When a vertex point (x, y, z) is assumed, the light emission time is calculable from i-th PMT hit,

$$t_i(x, y, z) = T_{\text{detected},i} - TOF_i(z, y, z) \tag{4.9}$$

where $T_{\text{detected},i}$ is the detected time of the photon, and $TOF_i(z, y, z)$ is the time of flight as,

$$TOF_i(x, y, z) = \frac{n_{\text{eff}} \sqrt{(x - x_i)^2 + (y - y_i)^2 + (z - z_i)^2}}{c}, \tag{4.10}$$

where n_{eff} is an effective refractive index representing both the liquid scintillator and the buffer oil. In reality, $T_{\text{detected},i}$ depends on charge because of a multi photon effect. The charge dependence is measured by source calibrations at various energies. At an ideal vertex point, there is no correlation between t_i and the space-time correlation coefficient dt_i/dx, expressed as

$$\frac{dt_i}{dx} = \frac{n_{\text{eff}}(x_i - x)}{c\sqrt{(x - x_i)^2 + (y - y_i)^2 + (z - z_i)^2}}. \tag{4.11}$$

The covariance between t_i and dt_i/dx is

$$\sigma_{t_i, dt_i/dx} = \sum_i w_i(t_i - \langle t_i \rangle)\left(\frac{dt_i}{dx} - \left\langle\frac{dt_i}{dx}\right\rangle\right) / \sum_i w_i \tag{4.12}$$

$$= \left[\sum_i w_i\left(t_i\frac{dt_i}{dx}\right) / \sum_i w_i\right] - \left[\langle t_i \rangle \left\langle\frac{dt_i}{dx}\right\rangle\right], \tag{4.13}$$

where w_i is the distance dependence weight for each PMT, $\langle t_i \rangle$ and $\langle dt_i/dx \rangle$ indicate their mean value. The first term works as a pull-push balance term for each PMTs with the deviation from the origin of time. The second term is a constant in a event, but it is independent of the pull-push balance term and related to the time profile of scintillation light emission. The vertex position is moved in order that the covariance for x, y, z converges on zero.

Precise estimation of vertex is done by "v2 fitter" with PDF of pulse shape. The pulse shape is position dependent and the likelihood function which is the product of the pulse shape collected from the available calibration data is used for the maximum likelihood method on determination of the vertex position. Pulse shapes are determined by transit time spread of PMTs, dark rate, probability of multiple hits and complex properties of the scintillator. In addition, pulse shapes depend on the position of events and the distance from PMTs. Some biases are not available if the same shapes can be formed somewhere. In order to avoid this problem, pulse shapes are parametrized with the vertexes and hit time information. These four parameters are denoted as x, y, z and Δt of each PMTs. Here, Δt represents the delay of the signal timings compared to the expectations calculated for x, y, z, t, and expressed as

$$\Delta t_i = t_i - t - TOF_i(x, y, z), \tag{4.14}$$

where t_i is the observed timing of the i-th PMT and TOF_i is the same as the previous notation. Pulse shapes at various points are defined as the invariant pulse shapes, which also include the effect of the multiple hits and re-emission of the scintillation light. The likelihood function is then expressed as,

$$L = \prod_i \psi_{\text{inv}}[\Delta t(x, y, z, t)], \tag{4.15}$$

where the multiplication is made over the PMTs having hits, and ψ is a pulse shape evaluated at Δt_i. In order to obtain the correct vertex position, the equations derived from likelihood function should be solved for four parameters. The maximum of it is achieved at a point where 4 dimensional gradient turns into zero.

4.7.2. Reconstruction Quality

Vertex Resolution from z-axis Calibration

During observation period, z-axis calibration was performed periodically as in Figure 4.17.
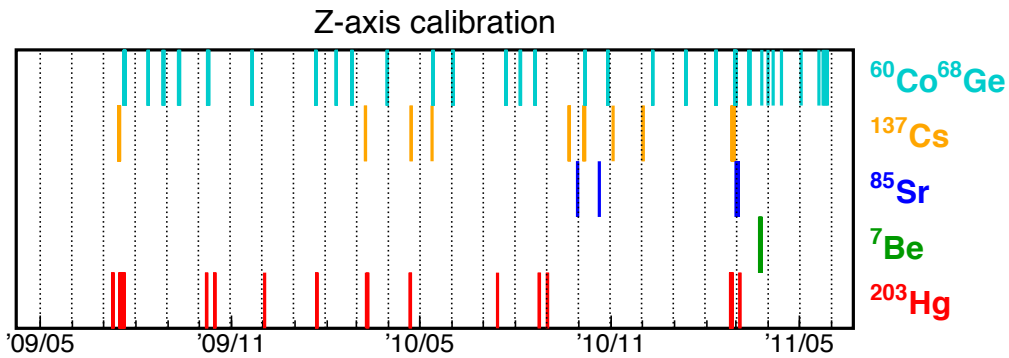
Figure 4.17.: Z-axis calibration campaign

The vertex resolution can be evaluated by comparing the radius distribution of data with simulation convoluted with resolution as shown in Figure 4.18. Obtained resolution is plotted in Figure 4.19. The vertex resolution is estimated as (14.74 ± 0.01) cm/$\sqrt{\text{E [MeV]}}$. For only higher energy sources, ^{68}Ge and ^{60}Co, both 2γ sources, the vertex resolution is independently estimated as (12.76 ± 0.02) cm/$\sqrt{\text{E [MeV]}}$.

Vertex Bias from off-axis Calibration

At the end of observation period, off-axis calibration was performed. Distance from the main source and the pin source which is closest to the center of the detector is evaluated and compared to the expected distance. The difference of the distance of observed and expected is shown in Figure 4.20. When a main source is inside 4.5 m radius sphere, the
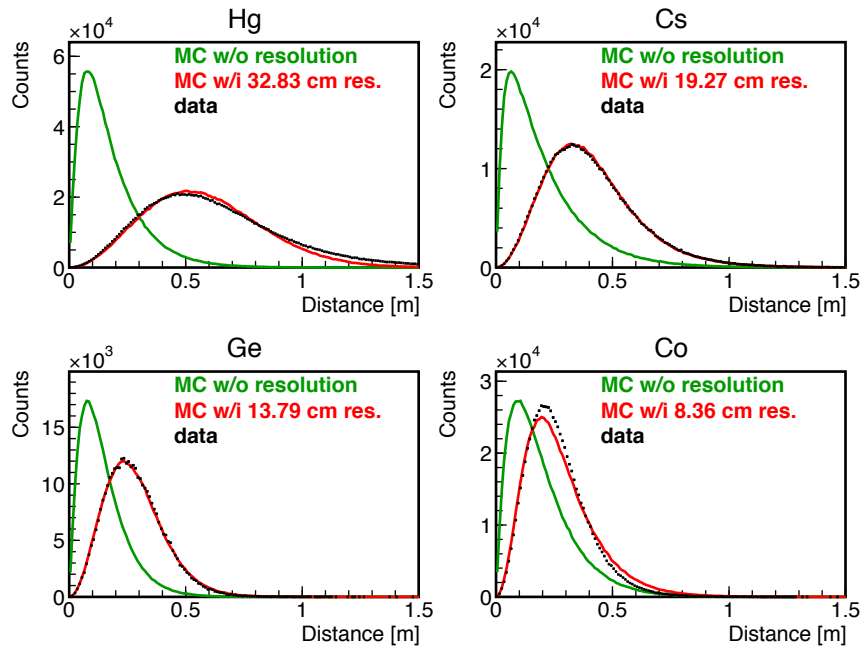
Figure 4.18.: Radius distribution of calibration sources and comparison with MC convoluted with and without resolution.
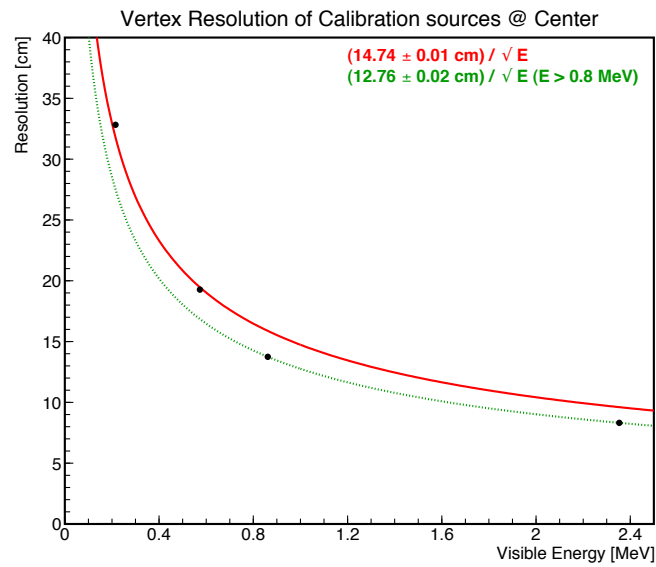
Figure 4.19.: Vertex Resolution of calibration sources as a function of energy.

difference is less than ± 5 cm. Hence the vertex bias at 4.5 m radius is evaluated as 5 cm.
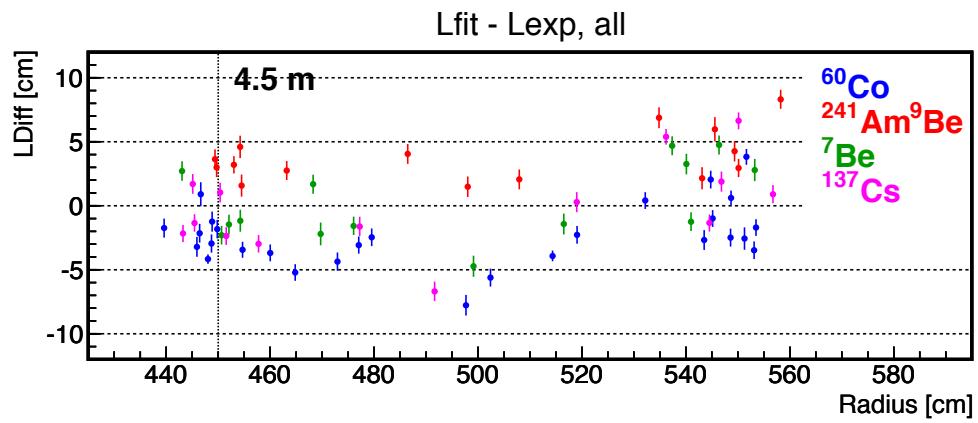
Figure 4.20.: Main Source radius and difference of distance.

4.8. Energy Reconstruction

4.8.1. pre-corrections

In prior to the vertex reconstruction, following corrections are applied to data.

- bad channel selection
- ga in correction
- dark hit correction
- muon gain correction
- shadow effect correction
- attenuation length correction
- SPE efficiency correction
- 20 inch combination correction

4.8.2. algorithm

The previous energy reconstruction algorithm, which had used only charge information of a event, had better resolution at higher energy. Several studies revealed that an energy reconstruction algorithm using hit information has better resolution at lower energy. Thus the current energy reconstruction algorithm employes hit information as well as charge information to insure better resolution both at lower and higher energy region. The current also employes hit time information for better discrimination between signal region and background region, which leads higher precision on dark hit subtraction and thus which leads lower systematic uncertainty on energy scale.

General likelihood(L) including hit, charge, time is expressed as follows,

$$L = \prod_{i \in no-hit} \kappa_{i,0} \left(\vec{r}_{\mathrm{pmt}_i}, \vec{r}_{\mathrm{impact}}, E_{\mathrm{vis}} \right) \left[\prod_{i \in hit} \left\{ \sum_{j=1}^{\infty} \kappa_{i,j} \left(\vec{r}_{\mathrm{pmt}_i}, \vec{r}_{\mathrm{impact}}, E_{\mathrm{vis}} \right) f_{i,j}(q_i) \right\} \eta_i(t_i \mid \mu_i) \right]$$

(4.16)

, where

$\kappa_{i,j}$	probability for i-th PMT to be hit by j-th photons, following the Poisson distribution
μ_i	expected number of photons hitting i-th PMT
$f_{i,j}(q_i)$	charge probability density function for i-th PMT, given j-th photon hits, following the Gaussian distribution
$\eta_i(t_i \mid \mu_i)$	hit time probability density function for i-th PMT, given μ_i

and are expressed as follows,

$$\kappa_{i,0} = \mathrm{e}^{-\mu_i} + (1 - \epsilon)\mathrm{e}^{-\mu_i} \equiv \nu_i \mathrm{e}^{-\mu_i} \tag{4.17}$$

$$\kappa_{i,j} = \frac{\mathrm{e}^{-\mu_i}\mu_i^j}{j!} \tag{4.18}$$

$$\mu_i = c \, \Omega_{\mathrm{eff}_i}(\vec{r}_{\mathrm{pmt}_i}, \vec{r}_{\mathrm{impact}})E_{\mathrm{vis}} + d_i \equiv b_i(\vec{r}_{\mathrm{pmt}_i}, \vec{r}_{\mathrm{impact}})E_{\mathrm{vis}} + d_i \tag{4.19}$$

$$f_{i,j}(q_i) = \frac{1}{\sqrt{2\pi j \sigma^2}}\mathrm{e}^{-\frac{(q_i - j)^2}{2j\sigma^2}} \tag{4.20}$$

$$\eta_i(t_i \mid \mu_i) = \frac{b_i\psi_i(t_i)E_{\mathrm{vis}} + d_i}{b_iE_{\mathrm{vis}} + \int_{-175\mathrm{nsec}}^{192\mathrm{nsec}}\Delta d_i dt_i} = \frac{b_i\psi_i(t_i)E_{\mathrm{vis}} + d_i}{\mu_i} \equiv \frac{s_i}{\mu_i} \tag{4.21}$$

, where

ϵ	detection efficiency of the 1 p.e. signal above the set threshold, 0.3 p.e, estimated to be 0.964 from the 1 p.e. distribution
c	some constant proportionality coefficient between MeV of energy scale and dimensionless occupancy factor
Ω_{eff}	effective solid angle, including quantum efficiency of PMT, attenuation length, and shadowing effects
b_i	expected number of photons per MeV
d_i	expected number of photons from dark hit of i-th PMT during time window
σ	the 1p.e. distribution, which is 0.386 p.e..
$\psi(t_i)$	real pulse shape function, given vertex and E_{vis} as a function of time
s_i	actual pulse shape function
Δd_i	$\int_{-175nsec}^{192nsec}\Delta d_i dt_i = d_i$

The analysis time window for hit and charge is 192 + 175 nsec, which corresponds to the approximate waveform recording time and time window before a trigger is issued, respectively.

Then the likelihood function, and the log-likelihood function are written down as,

$$L = \prod_{i\in no-hit} \nu_i \mathrm{e}^{-\mu_i} \prod_{i\in hit}(1 - \nu_i \mathrm{e}^{-\mu_i})\left(\sum_{j=1}^{\infty}\frac{1}{1 - \nu_i \mathrm{e}^{-\mu_i}}\frac{\mu_i^j \mathrm{e}^{-\mu_i}}{j!}\frac{1}{\sqrt{2\pi j \sigma^2}}\mathrm{e}^{-\frac{(q_i - j)^2}{2j\sigma^2}}\right)\frac{s_i}{\mu_i} \tag{4.22}$$

$$\log(L) = \sum_{i\in no-hit}\log(\nu_i \mathrm{e}^{-\mu_i}) + \sum_{i\in hit}\log(1 - \nu_i \mathrm{e}^{-\mu_i})$$
$$+ \sum_{i\in hit}\log(\sum_{j=1}^{\infty}\frac{1}{1 - \nu_i \mathrm{e}^{-\mu_i}}\frac{\mu_i^j \mathrm{e}^{-\mu_i}}{j!}\frac{1}{\sqrt{2\pi j \sigma^2}}\mathrm{e}^{-\frac{(q_i - j)^2}{2j\sigma^2}}) + \sum_{i\in hit}\log(\frac{s_i}{\mu_i}) \tag{4.23}$$

$$\log(L) \equiv \sum_{i\in no-hit}\log(\nu_i \mathrm{e}^{-\mu_i}) + \sum_{i\in hit}\log(1 - \nu_i \mathrm{e}^{-\mu_i}) + \sum_{i\in hit}\log(c_i) + \sum_{i\in hit}\log(\frac{s_i}{\mu_i}) \tag{4.24}$$

In the log likelihood function, the first two terms are taken alone constitute a generic no-hit/hit filter, the third term accommodates charge information, and the fourth term

accommodates time information. At the lower energy, no-hit, hit and time terms work effectively while charge term works effectively at higher energy. The charge term is abbreviated in the practical process since it is calculated numerically.

The best reconstructed energy is derived from the maximization condition of the log-likelihood function,

$$\frac{\partial \log(L)}{\partial E} = 0. \tag{4.25}$$

This can be solved with modified Newton-Raphson method;

$$\Delta E_{vis} = -\frac{\frac{\partial \log(L)}{\partial E}}{\frac{\partial^2 \log(L)}{\partial E^2}}. \tag{4.26}$$

The visible energy, E_{vis} is reconstructed by summing up ΔE_{vis} for some iterations. In the current analysis, five iterations are applied and it is enough to reach an accuracy of 10^{-5}. The first and the second derivative of the log-likelihood function using four terms in above discussion are written down as,

$$
\begin{aligned}
\frac{\partial \log(L)}{\partial E}\Big|_{no-hit} &= -\frac{b_i}{\nu_i}(\nu_i - (1-\epsilon)) \\
\frac{\partial \log(L)}{\partial E}\Big|_{hit} &= \frac{b_i}{e^{\mu_i} - \nu_i}(\nu_i - (1-\epsilon)) \\
\frac{\partial \log(L)}{\partial E}\Big|_{charge} &= b_i \frac{\partial \log(c_i)}{\partial \mu_i} \\
\frac{\partial \log(L)}{\partial E}\Big|_{time} &= \frac{b_i d_i}{s_i \mu_i}(\psi_i(t_i) - 1)
\end{aligned}
\tag{4.27}
$$

$$
\begin{aligned}
\frac{\partial^2 \log(L)}{\partial E^2}\Big|_{no-hit} &= -\frac{b_i^2}{\nu_i^2}(1-\epsilon)^2 \\
\frac{\partial^2 \log(L)}{\partial E^2}\Big|_{hit} &= -\frac{b_i^2}{(e^{\mu_i} - \nu_i)^2}\{\nu_i e^{\mu_i} - 2(1-\epsilon)e^{\mu_i} + (1-\epsilon)^2\} \\
\frac{\partial^2 \log(L)}{\partial E^2}\Big|_{charge} &= b_i^2 \frac{\partial^2 \log(c_i)}{\partial \mu_i^2} \\
\frac{\partial^2 \log(L)}{\partial E^2}\Big|_{time} &= -\frac{b_i^2 d_i}{s_i^2 \mu_i^2}(\psi_i(t_i) - 1)(\psi_i(t_i)\mu_i + s_i).
\end{aligned}
\tag{4.28}
$$

4.8.3. Reconstruction Quality

z-axis calibration

As described in vertex reconstruction section, z-axis calibrations were performed regularly during the observation period. Reconstructed energy distribution for each of 6 calibration sources located at the center of the detector is shown in Figure 4.21. From

Figure 4.21.: Energy distribution of calibration sources located at the center of the detector

the reconstructed energy of each calibration source, the energy dependence of the energy resolution is estimated as $(6.86 \pm 0.01)\ \%/\sqrt{E[MeV]}$ as in Figure 4.22.

Time and Position dependence of the reconstructed energy is evaluated at most 0.80 % and 1.79 % within 4.5 m radius sphere.
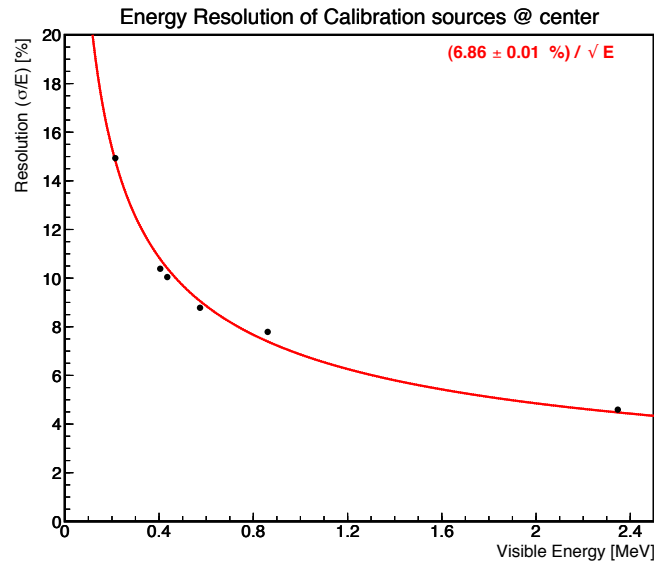
Figure 4.22.: Energy dependence of energy resolution

4.8.4. Energy Scale Uncertainty

While visible energy of data is reconstructed and calibrated as described above, variation of the reconstruction is not fully included and should be treated as systematic uncertainty. The sources of the uncertainty of the energy scale are as follows,

- Position and Time dependence

- Quenching effect

- Contribution ratio of scintillation light

- Contribution ratio of Cherenkov light

- Dark hit subtraction

Position and Time dependence

The uncertainty from the position and time dependence of energy scale is estimated by z-axis calibrations as 0.80 % and 1.79 % respectively.

Quenching effect

The number of scintillation photons is proportional to the deposited energy in the first order, but there is an non-negligible dependence on the ionization density called " quenching effect", causing the energy non-linearity for each particle. In the heavy

particle case like α, the quenching effect becomes very large because of its high ionization density. The Birks formula is suitable to estimate this effect,

$$\frac{dL}{dx} = L_0 \frac{dE/dx}{1 + kB(dE/dx)} \tag{4.29}$$

where kB is Birks constant, L is the luminescence, L_0 is the luminescence at low specific ionization density and dL/dx is the emitted light intensity per unit length.

Contribution ratio of scintillation light

Since the scintillation light emission is dependent to the quenching effect, contribution of it should be treated by altering the quenching effect.

Contribution ratio of Cherenkov light

The number of photons for electrons and positrons are both dependent to its scintillation and Cherenkov emission. Although the direct contribution of Cherenkov light is ignorable due to the smaller wavelength of it compared to the absorption wavelength of the liquid scintillator, the re-emission light contributes to the reconstructed energy. This contribution should also be treated by altering the quenching effect.

Dark hit subtraction

Although the mean dark charge is calculated for each PMT run by run and the correction is applied to data, the uncertainty is not included. The uncertainty is much more significant for lower energy.

Integration of Energy Scale Non Linearity

Using 6 gamma ray data from source calibrations (^{203}Hg, ^{137}Cs, ^{68}Ge, ^{60}Co), spallation neutron capture on proton and ^{12}C, 2 positron data (^{11}C, ^{10}C), and 1 electron data (^{12}B), uncertainties from the quenching effect, contribution of Cherenkov light and scintillation light, and dark hit subtraction are analyzed. Note that the two gamma rays emitted from ^{68}Ge and ^{60}Co are treated as one gamma rays whose energy is the effective mean of them (0.511 MeV and 1.253 MeV, respectively), because quenching effect depends on the energy of each gamma rays, not on the sum of them. In the case of gamma rays, MC simulation using GEANT4 is employed to calculate dE/dx of electrons produced in Compton scattering and photoelectric absorption.

$\Delta\chi^2$ distribution of Birks constant, contribution of Cherenkov light and scintillation light, and dark hit subtraction are shown in Figure 4.23. The best parameter with 1σ error is evaluated as,

- Birks constant (kB) : (0.26 + 0.10 - 0.07) mm/MeV
- Contribution of Cherenkov light (C_{Che}) : 0.037 + 0.030 - 0.032

71
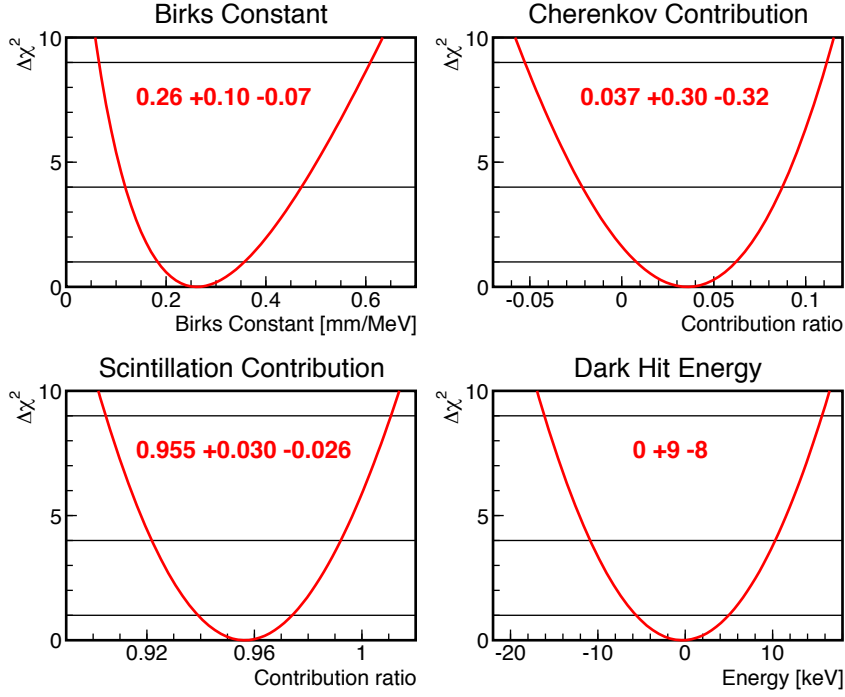
Figure 4.23.: $\Delta\chi^2$ distribution of energy scale parameters

- Contribution of scintillation light (C_{sci}) : 0.955 + 0.030 - 0.026
- Dark hit subtraction (E_{dark}) : (0 + 9 - 8) keV.

Then, the correlation between each parameter is shown in Figure 4.24. Among them, especially Birks constant and Cherenkov light are strongly anti-correlated.

Using these 4 parameters, the visible energy is calculated as,

$$E_{\mathrm{vis}} = C_{\mathrm{Che}}E_{\mathrm{Che}} + C_{\mathrm{sci}}E_{\mathrm{sci}}(kB) + E_{\mathrm{dark}}, \tag{4.30}$$

where $E_{\mathrm{sci}}(kB)$ is the visible energy with full contribution of scintillation light given Birks constant. Figure 4.25 shows the energy non-linearity correction between real energy and visible energy given with the four best parameters, and Figure 4.26 shows contour plots of the energy non-linearity for electron, gamma, and positron. The energy non-linearity for electron spreads at low energy because of the uncertainty from dark hit subtraction. The dominant theoretical visible energy spectrum for ^{7}Be solar neutrino analysis such as ^{7}Be solar neutrino, ^{210}Bi, ^{85}Kr, and ^{11}C is produced considering the 4 parameters as in Figure 4.27 but other spectra are produced with the best parameters of them for simplification.

The uncertainty of energy is summarized in Figure 4.28. Energy uncertainty is evaluated to be 2.9 % above 0.5 MeV, 2.1 % above 1 MeV, 1.7 % above 2 MeV, and 1.5 % above 4 MeV, respectively.
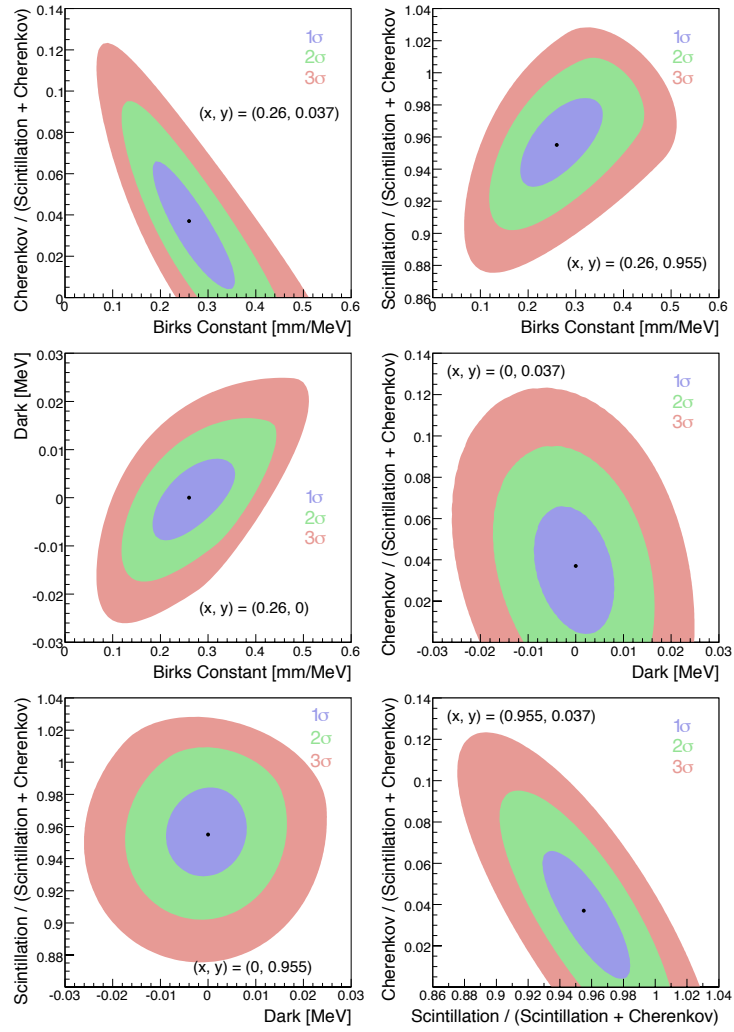
Figure 4.24.: Correlation of energy scale parameters
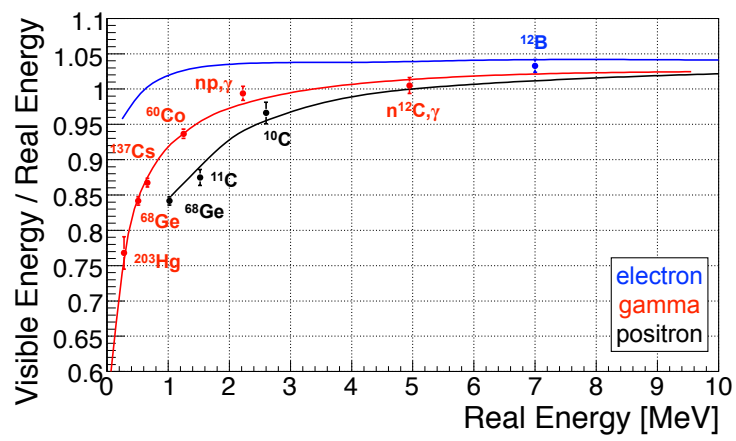
Figure 4.25.: Correlation of energy scale parameters
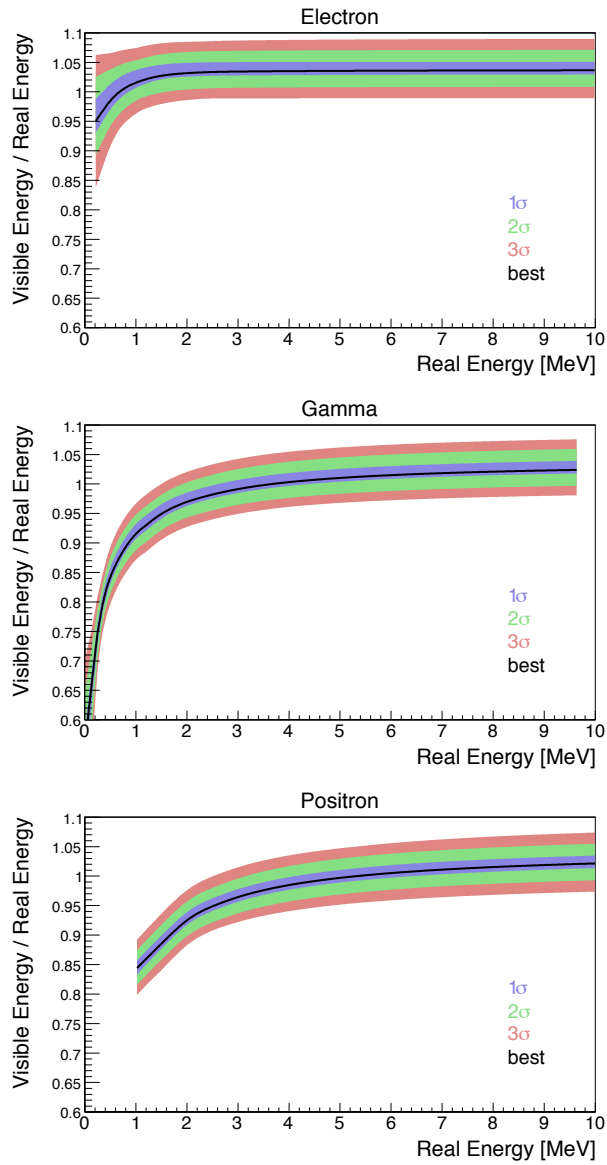
Figure 4.26.: Correlation of energy scale parameters
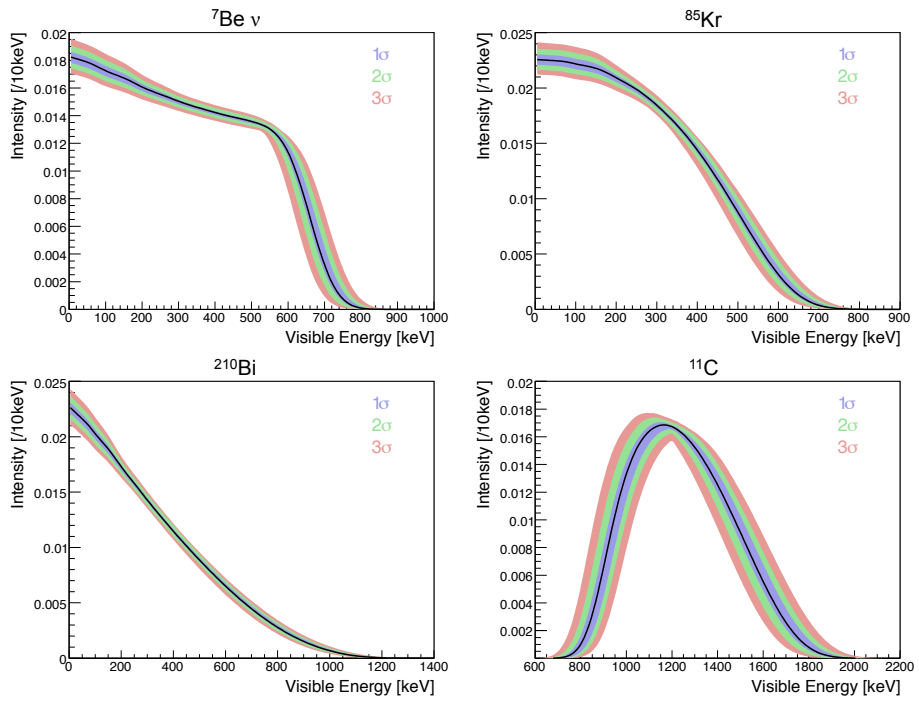
Figure 4.27.: Correlation of energy scale parameters
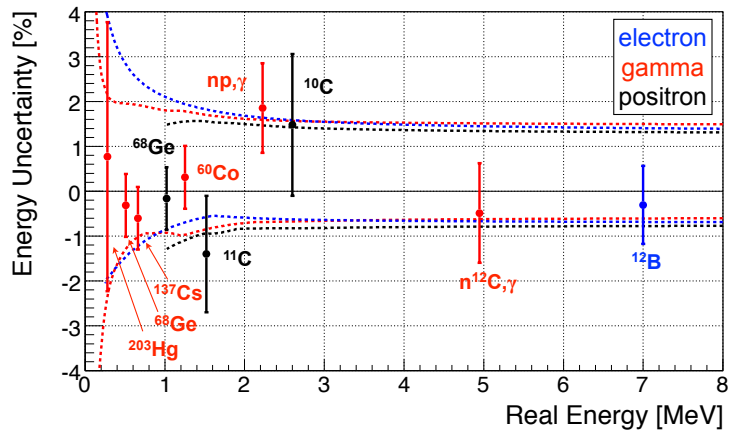
Figure 4.28.: Correlation of energy scale parameters

5. Event Selection

5.1. Primary Data Set

5.1.1. KamLAND ^{7}Be Solar Neutrino Phase

KamLAND collaboration had purified the KamLAND liquid scintillator in 2008 and 2009 for enabling observation of ^{7}Be solar neutrinos whose energy is less than 1 MeV. Whole period of ^{7}Be solar neutrino phase is between just after finishing the purification and the just before the preparation of the next phase of KamLAND for observation of neutrino-less double beta decay, KamLAND-Zen. The summary of period is listed in Table 5.1.

Table 5.1.: KamLAND ^{7}Be Solar Neutrino Phase

	date & time	run number
start	Feb. 06, 2009 08:02	8292
end	Aug. 16, 2011 17:39	10678

5.2. Bad Event Rejection

Among KamLAND events acquired with physics triggers, there are unphysical events due to performance limitation or malfunction of PMTs or electronics. These unphysical events are categorized into the following types and removed from the candidate events for ^{7}Be solar neutrino analysis.

1. Flasher event

2. Missing waveform event

3. Post 1PPS trigger event

4. Post high charge event

5. Post deadtime event

6. Close event

In addition, a

7. Poorly reconstructed event

is also removed from the candidate events.

5.2.1. Flasher event

A flasher event is caused by light emission from a PMT. Such emission is probably due to discharge in dynodes. The surrounding PMTs detect photons from the light emission then a event is triggered. Due to this characteristic process of event generation, a flasher event is easily selected with following criteria:

- Total charge in ID > 2500 p.e.

- The maximum charge in a single PMT in ID / Total charge in ID ≥ 0.6

- Mean charge of the neighboring PMTs around a PMT accepting the maximum charge ≥ 20 p.e.

- Not noise event; number of hit in 17-inch PMTs is less than average of maximum number of hit in 100 ns-window and 50 hit.

The time and charge distribution of a typical flasher event and the flasher event selection is shown in Figure 5.1. The ratio of the number of flasher events to that of good events is approximately 5.0×10^{-4} % in low energy, thus the inefficiency of the flasher event cut is estimated to be less than 5.0×10^{-4} %.

5.2.2. Missing waveform event

A missing waveform event is caused by saturation of a waveform buffer in an ATWD in a KamFEE channel. Such effect from the limitation likely occurs when event rate is high. In such case, the number of acquired waveforms is less than the number of HITs, which the FBE trigger accepted. Thus, a missing waveform event is selected with following criteria:

- Nhit17 $\leq$ NsumMax

, where Nhit17 is the number of recorded waveforms in 17-inch PMTs and NsumMax is the maximum number of 17-inch PMT hits within a 125 ns-period around the time a trigger was issued. The correlation of Nhit17 to NsumMax is shown in Figure 5.2. The inefficiency is estimated to be 7.6×10^{-3} % from that in ^{137}Cs source calibration runs.

5.2.3. Post 1PPS trigger event

KamFEE was upgraded in 2007 in order to reconstruct an event more effectively when missing waveform events frequently appear, e.g. just after muon events. Since then new noise-like events have became obvious after 1PPS triggers. Time interval from preceding 1PPS events and proceeding noise like events is multiples of approximately 34 us, as shown in Figure 5.3.
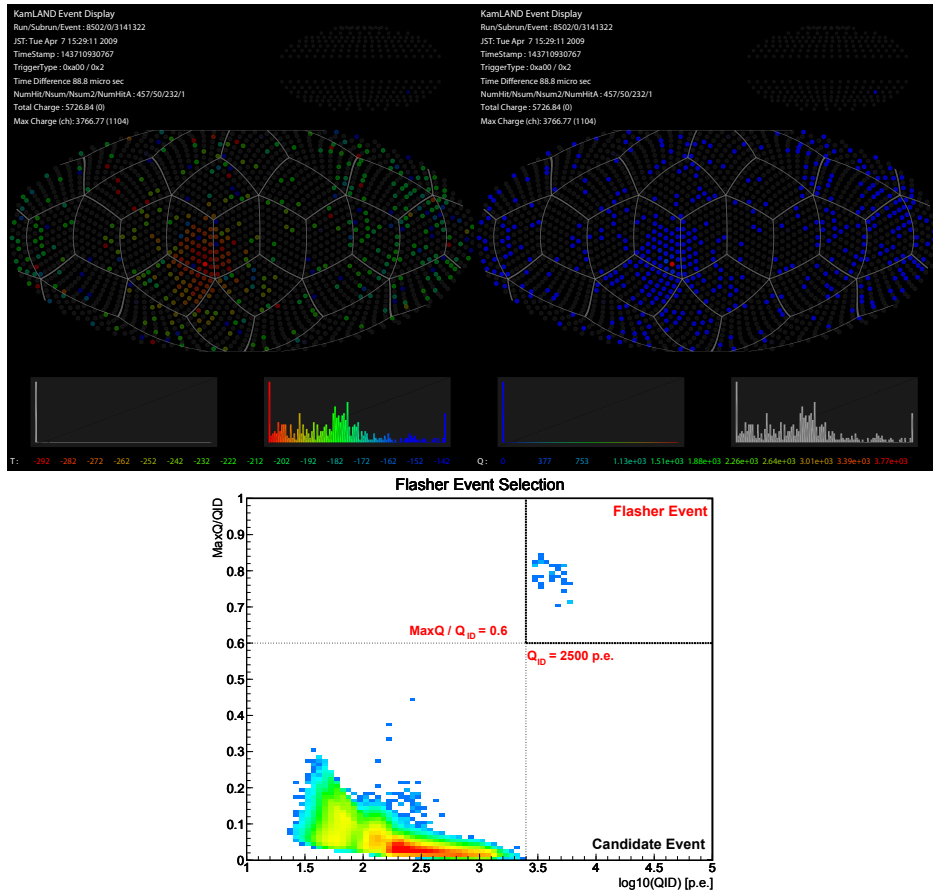
Figure 5.1.: Typical flasher event and flasher event selection. The top figures show timing distribution (left) and charge distribution (right) of a typical flasher event inside the detector. Each dot corresponds to a PMT. The faster the timing or the larger the charge a dot is shown in red. The most vivid red dot in both figures is the source flasher PMT. The flasher PMT fires the earliest by the light emission in itself with dominant charge of the event, then the near PMTs fire. The bottom graph shows distribution of (maximum charge in ID, 'MaxQ') / (total charge in ID, 'QID') in a typical one day run. Flasher events cluster at larger QID and MaxQ/QID.

From the time constant, this symptom is presumably related to digitization interval in ATWD chips, which takes 25.6 us. A post 1PPS trigger event is selected with following criteria:

- Time interval from the preceding 1 PPS event < 100 us

For a physics event, a Prescale trigger is only issued within 10.24 ms after a 1PPS trigger while a Single trigger is issued independently to a 1PPS trigger, thus removing
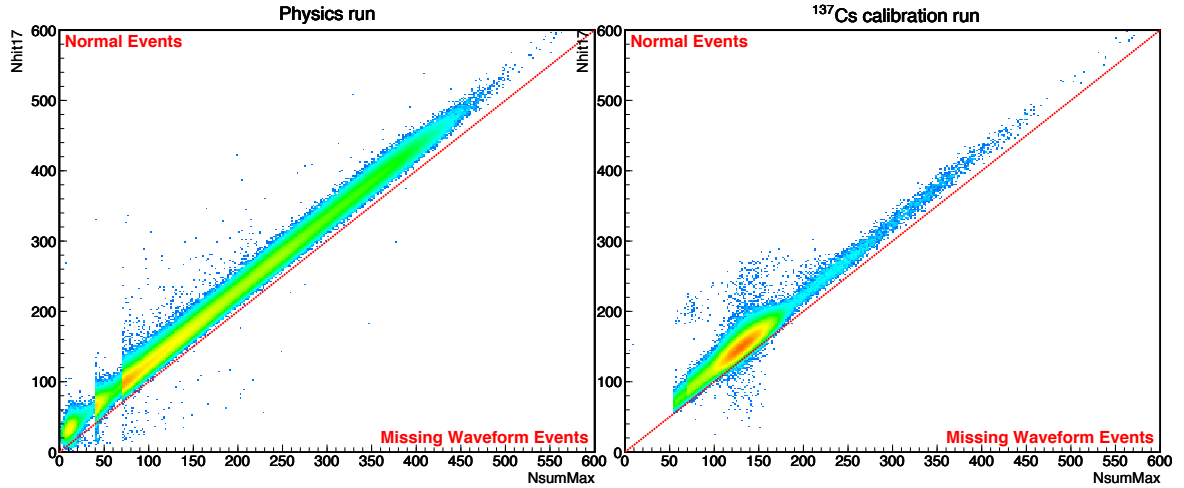
Figure 5.2.: Correlation between *Nhit17* and *NsumMax* and Missing Waveform event selection. The left graph shows the correlation in a typical one-day physics run. The right graph shows the correlation in ^{137}Cs source calibration runs, in which the source is deployed in different position between -4.5 m $\leq z$ $\leq$ 4.5m. For the events shown in the graph, 2 m distance cut from the source position is predominantly applied. In the source runs, the number of selected events is 874, while the number of normal events is approximately 1.15×10^7, from which the selection inefficiency is calculated to be 7.6 $\times 10^{-3}$ %.
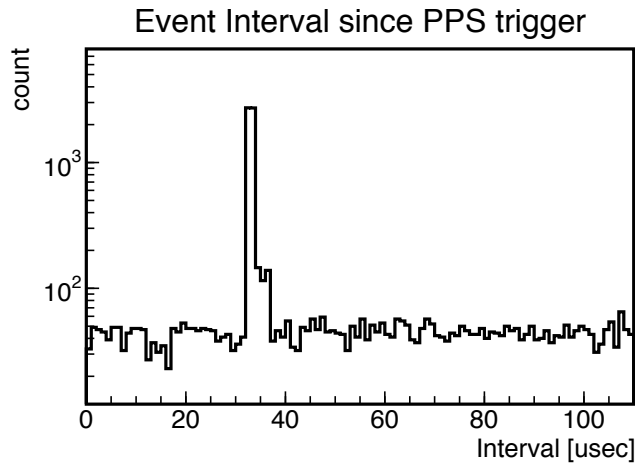
Figure 5.3.: Event Interval since previous PPS trigger. Noise like events cluster at 34 us.

post 1PPS trigger event introduces difference in livetime for Prescale trigger events and Single trigger events. This selection affects livetime and is discussed in the following

section. A leading PPS trigger event itself is also rejected.

5.2.4. Post high charge event

After a high charge event, many events follow for a while. Such high charge events correspond to muon events, sub-muon energy events and flasher events. The following events are partially physics events e.g. muon spallation products, and partially electronics noise from PMT afterpulses and/or ringing effects in analog circuitry. Total charge of 17-inch PMTs of an event is used as one of basis for muon event selection as described in the previous chapter. Figure 5.4 shows event rate trend after a high charge event.
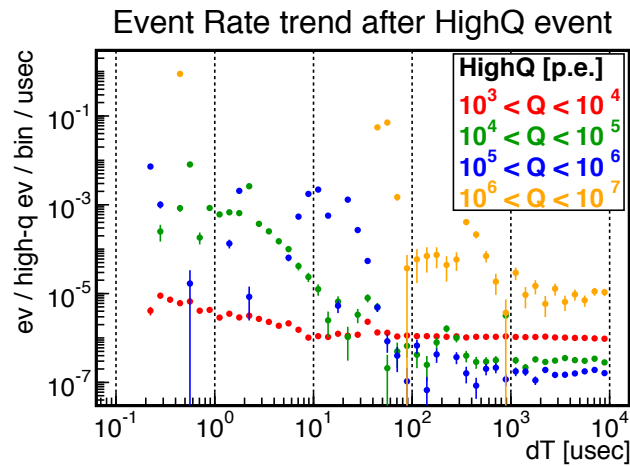
Figure 5.4.: Event rate trend of post high charge event. $10^3 < Q_{17} < 10^4$ p.e. events accompanies high rate events for approximately 10 us. It also accompanies a high event rate cluster at 32 us, which is presumably the same noise events as post 1PPS noise events. Higher charge events approximately correspond to different types of muons, that is, $10^4 < Q_{17} < 10^5$ p.e. events correspond to clipping muons, $10^5 < Q_{17} < 10^6$ p.e. events through going muons and $10^6 < Q_{17} < 10^7$ p.e. events showering muons respectively. They accompanies high rate events at most for 2 ms, while there is visible suppression at around 10 us due to deadtime of electronics.

In order to reject those unphysical events or background physics events after high charge events, veto window is specified. Preceding high charge events are classified into two criteria:

- muon event
  · $Q_{17} \geq 10^4$ p.e. (Q_{17} : total charge in the 17-inch PMTs)
  · $Q_{17} \geq 500$ p.e. $\cap$ $N_{200\text{OD}} \geq 5$ hits ($N_{200\text{OD}}$: maximum number of PMT hits in the outer detector within a 200 ns window)

- sub-muon event
  - $10^3 \leq Q_{17} < 10^4$ p.e. .

And veto window is specified with following criteria:

- post muon event :   2 ms

- post sub-muon event or post flasher event : 100 us

This selection affects livetime and is discussed in the following section. A leading muon event is also rejected.

5.2.5. Post deadtime event

While buffer on the trigger electronics board gets full, no acquisition trigger is generated. This period is called trigger deadtime. In order to avoid post muon events after possible muon events inside this deadtime, the same veto time as post muon event veto is specified as following criteria:

- event interval since previous end of a deadtime is less than 2 ms

This selection affects livetime and is discussed in the following section.

5.2.6. Close event

The distribution of time interval (Δt) of any temporally adjacent events should follow an exponential decay curve whose time constant is ($\ln 2 \times$ event rate), when they are not correlated. In KamLAND data, the distribution has much excess at Δt is less than 1 us. A pair of events occurs at such short Δt is called a Close event and the property is shown in Figure 5.5. The event pairs shown in the figure are those either event of which has passed through the previous event selection and is inside R < 4.5 m, which means that the other event of a pair can be almost any events inside the detector. The former and the latter event of a pair is called prompt and delayed event respectively.

In the Δt distribution, the excess at less than 1 us has approximately 100 ns of time constant, which is smaller than that of any known background sources. The source of the enhancement is partially regarded as the sequential decay of ^{212}BiPo events which has 431 ns of time constant, and is evident as the cluster less than 1 m in the distance distribution and as the peak around 0.7 MeV in the delayed energy distribution.

In the prompt energy distribution, the red histogram for the case a prompt event is a candidate event, or in the delayed energy distribution, the green histogram for the case a delayed event is a candidate event, ^{210}Po peak at 0.3 MeV and ^{14}C distribution at energy less than 0.2 MeV is evident. On the other hand the green histogram in the prompt energy distribution or the red one in the delayed show different spectrum from physics event spectrum and thus infer the poor quality of data acquisition.

Although exact cause is not discovered, it is assumed that this problem is related to event separation of a close event. When event separation is not well performed, event reconstruction of both the prompt and delayed event is reliable. In order to reject such possibility, a close event is removed with following selection criteria:

Figure 5.5.: Close Event property

- event interval < 1 us

This selection affects livetime and is discussed in the following section.

5.2.7. Poorly reconstructed event

After rejecting events selected with the previous selections, there still remains poorly reconstructed events. In order to distinguish those events from well reconstructed events, a parameter "*VertexBadness*" is useful. *VertexBadness* of an event is estimated from distribution of time T, hit HIT and charge Q of each PMT pulse and is composed of 9 parameters listed below;

83

- χ^2_T :Difference of the expected and the observed time distribution

- σ_T :Standard deviation of time of flight (TOF) subtracted time spectrum

- H_T :Peak height of TOF subtracted time spectrum

- χ^2_{HIT} :Difference of the expected and the observed number of *HIT*s

- R_{HIT} :Ratio of number of total hits to integrated expected *HIT*s

- R_{N150} :Ratio of maximum number of hits within 150 ns to NsumMax

- R_{N48} :Ratio of maximum number of hits within 48 ns to NsumMax

- χ^2_Q :Difference of the expected and the observed charge in PMTs

- σ_Q :RMS of distribution of ratio of total charge to total expected charge.

Readers may refer to (Nakajima, 2009:p120-p125) for the meaning of each component in detail. Notice that χ^2_Q is modified.

Figure 5.6 shows correlation of *VertexBadness* and visible energy of all events inside 4.5 m radius, which have passed event selections above.

There are three prominent clusters. The most dominant one lies at *VertexBadness* < 2 at the energy higher than 0.5 MeV and has exponentially increasing *VertexBadness* at the lower energy. Another one spreads at $0.2 < E < 0.6$ MeV. The other one has rising-robe structure, which extends from approximately the coordinates of (0.5, 3) to (1.5, 5). More than 99 % of events belongs to the first cluster and are well reconstructed. On the other hand, the second and the third clusters have worse *VertexBadness* and likely have badly reconstructed vertex and/or energy, thus are not suitable for ^{7}Be solar neutrino analysis. In order to discriminate the first cluster from the second and the third one, an energy dependent *VertexBadness* threshold is introduced as

$$VertexBadness = 41.12 \times e^{-9.66 \times 10^{-3} \times Energy \text{ [MeV]}} + 2.307, \qquad (5.1)$$

and is shown as a black solid line in the figure. The events above the line are classified as "bad" events and are not used in ^{7}Be solar neutrino analysis. The events below the line are classified as "good" events.

In the energy distribution graph in Figure 5.7, the "bad" events show no significant physics spectrum, while the "all" events show ^{210}Bi shape at 0.4–1.0 MeV and ^{11}C shape at 1.1–1.8 MeV. This suggests that a "bad" event is not generated simply by bad reconstruction of a physics event, but that it is generated with the correlation of another event having different energy. They are partially discovered as "Pileup" events, which have multiple physics events inside a DAQ event and are described in detailed in the next chapter.

Figure 5.8 shows correlation of *VertexBadness* and visible energy of events in ^{137}Cs source calibration runs. The same selection as that in Figure 5.2 is performed. The inefficiency is estimated to be 1.4×10^{-2} % from the ratio of rejected events in ^{137}Cs source calibration runs.
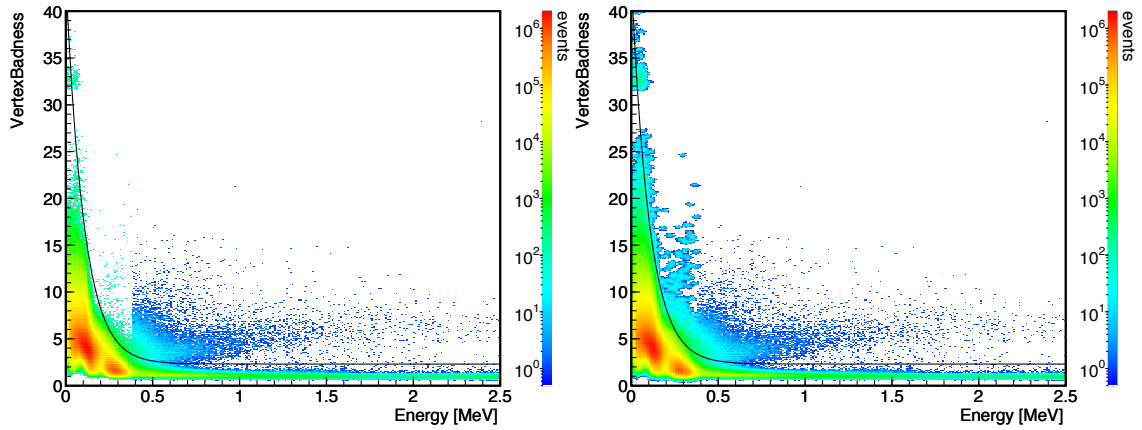
Figure 5.6.: Correlation between *VertexBadness* and Visible Energy in all physics runs. The left graph shows the original distribution of the correlation. The right graph shows a blurred distribution of the left one at $E < 0.38$ MeV in order to visualize the continuity of the distribution among events acquired with different types of triggers and thus scaled differently.
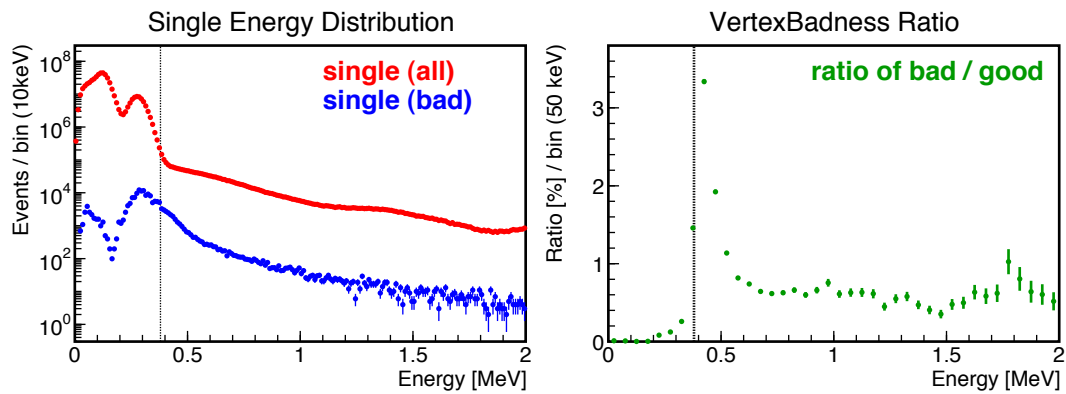
Figure 5.7.: Energy distribution of poorly reconstructed events compared to that of all single events and the ratio of the events.
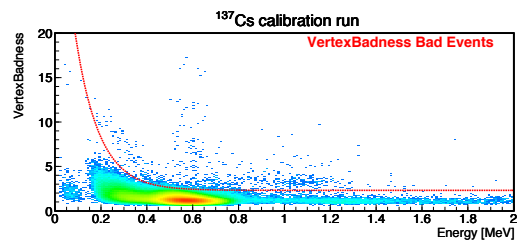
Figure 5.8.: Correlation between *VertexBadness* and Visible Energy in ^{137}Cs source calibration runs. The same selection as that in Figure 5.2 is performed. In the source runs, the number of selected bad events is 1617, while the number of normal events is approximately 1.15×10^7, from which the selection inefficiency is calculated to be 1.4×10^{-2} %.

5.3. Livetime and Analysis Period

Livetime is the total duration of confirmed clean data periods. The livetime is calculated by three types of a period as follows,

- RunTime : Time of data taking period.

- Deadtime : Time of no data period or known invalid data taking period.

- Vetotime : Time for rejection of periods with known background events.

5.3.1. Runtime

Runtime of a run is defined as the interval between the first and the last event. The uncertainty of runtime is estimated to be approximately 1.5 ms, which is derived from typical Prescale trigger rate, approximately 600Hz. The contribution of this uncertainty to a typical 24-hours run is less than 2×10^{-6} %.

5.3.2. Deadtime

Deadtime is classified into six types. In each case, whole volume of detector is vetoed.

- Primary run base deadtime selection
  In ^{7}Be solar neutrino analysis, data in a period when data quality from all of the ID 17-inch PMTs, the ID 20-inch PMTs and the OD PMTs is good is used. Thus when either of them is poor, a specified period is vetoed from candidate period. Data quality gets poor mostly due to malfunction of electronics for such cases. In the following list, the name of a run type is followed by classification code, Run Grade in parentheses. In comparison to what follow, when an entire run has clean data, the run is classified as a good run and has Run Grade 0.

  - Bad run (10)
    When data quality of ID 17-inch PMTs or OD PMTs is poor in all or almost all of a run, the run is classified as a bad run. This includes a short test run whose duration is less than six minutes. The entire run is vetoed.

  - 20-inch bad run (9)
    When data quality of ID 17-inch PMTs and OD PMTs is good in a entire run, but that of ID 20-inch PMTs is partially or thoroughly bad in the run, the entire run is vetoed.

  - 20-inch bad and half bad runs (6)
    When data quality of ID 17-inch PMTs or OD PMTs is poor in finite periods in a run, and data quality of ID 20-inch PMTs is poor outside the periods, the entire run is vetoed.

  - Half-bad run (5)
    When data quality of ID 17-inch PMTs or OD PMTs is poor in finite periods in a run, and data quality of ID 20-inch PMTs is poor only inside the periods

or is good in the entire run, the period is vetoed.

- Secondary short period deadtime selection

    - Trigger dead period
    When the buffer of the KamFEE trigger board is almost full, the trigger board issues a Disable Trigger then suspends issuing another trigger. Once the buffer gets empty, the trigger board issues an Enable Trigger then resumes issuing triggers. No triggers are issued between these two triggers, the period is vetoed.

    - Missing muon period
    Multiple noise events could follow muons within 150 us. In case muon data recording fails, timing of the muon, "missing muon" is estimated with a cluster of noise events. Noise events are specified with following selection,

$$[N_{100} < 40] \cup [N_{100} < (number \ of \ ID \ hit)/2 - 10],$$

    where N_{100} is maximum number of ID hit in 100 ns, and a cluster is selected when the number of noise events ≥ 4 within 1 ms outside 1ms window after detected muons. Between the time of the first event and that of the last event in a cluster is specified as missing muon period and is vetoed.

5.3.3. Vetotime

Vetotime is classified into four types. In each case, whole volume of detector is vetoed.

- Post muon event   : 2 ms period since a muon event is vetoed.

- Post sub-muon event   : 100 us period since a sub-muon event is vetoed.

- Post 1PPS event   : 100 us period since a 1PPS event is vetoed.

- Post deadtime   : 2 ms period since the end of a deadtime period is vetoed

5.3.4. Livetime

In ^{7}Be solar neutrino analysis, whole volume of detector is vetoed for both deadtime and vetotime periods. Thus livetime calculation is simply explained as follows,

$$\text{Livetime} \equiv \text{Runtime - Combined \ Vetotime},$$

where combined vetotime is the sum of deadtime and vetotime with considering overlap of these periods. Livetime fraction to runtime is shown in Figure 5.9. The average fraction is calculated to be 98.1 %.

The uncertainty of livetime is estimated from the fraction of the number of PPS triggers in livetime to livetime, which is ideally one. The fraction is shown in Figure 5.10. The mean deviation of fraction is $5.6 \times 10^{-3}\%$, and this is used as the uncertainty of livetime.

5.3.5. Livetime of Prescale trigger events

As described in the chapter, the Detector, a Prescale trigger is issued during 10.24 ms just after a PPS trigger. Hence, the livetime of Prescale trigger events is approximately 1 % of the livetime of Single trigger events.

The post PPS trigger veto or the close event rejection introduced for bad event rejection induces different ratio of deadtime to runtime between Prescale trigger events and Single trigger events. Thus the livetime of Prescale trigger events is defined as,

$$\text{Livetime}^{\text{Prescale}} = \text{Runtime}^{\text{Prescale}} - \text{Combined Vetotime}^{\text{Prescale}}.$$

The fraction of Livetime$^{\text{Prescale}}$ to Livetime, Prescale fraction, is 1.011 % and is a bit smaller than the designed value, 1.024 % due to the contribution of those types of event rejection. The Prescale trigger events are scaled by one over this fraction on comparing with Single trigger events.

5.3.6. Summary of Livetime

Livetime information is summarized in Table 5.2.

Table 5.2.: Summary of Livetime

Runtime	627.8 days
Livetime	615.9 days
Livetime$^{\text{Prescale}}$	6.229 days
Prescale fraction	1.011 %
Uncertainty of Runtime	$< 2 \times 10^{-6}$ %
Uncertainty of Livetime	5.6×10^{-3} %

5.3.7. Run Selection for Analysis

As described in the previous section, good runs and good periods of half-bad runs are used in ^{7}Be solar neutrino analysis. The mean analysis period is summarized in Table 5.3. The major off-time periods from Table 5.1 are the periods just after the liquid scintillator distillation thene short life BiPo event rates were high, the period when one HV crate is out of use and the period after whole detector calibration.

Table 5.3.: Analysis period for observation of ^{7}Be solar neutrinos

	date & time	run number
major on-time		
start	Apr. 07, 2009 14:29	8502
end	Oct. 07, 2010 07:22	9788
start	Dec. 21, 2010 00:43	9972
end	Jun. 21, 2011 08:58	10485
major off-time		
start	Feb. 06, 2009 08:02	8292
end	Apr. 07, 2009 14:13	8501
start	Oct. 07, 2010 17:10	9792
end	Dec. 21, 2010 00:27	9971
start	Jun. 21, 2011 13:12	10486
end	Aug. 16, 2011 17:39	10678
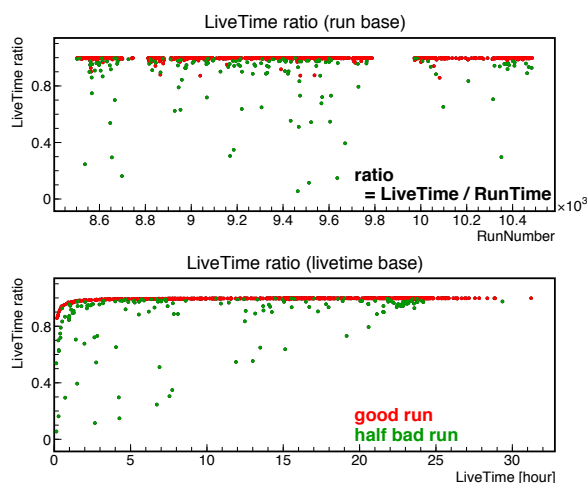
Figure 5.9.: Livetime ratio to runtime. In each graph, a single red or green dot corresponds to a good or half-bad run. The upper graph shows the trend of the ratio for the ^{7}Be solar neutrino analysis period. The lower graph shows the correlation between the ratio and the livetime. A half-bad run has smaller ratio due to bad periods in the run. A shorter run has smaller ratio due to the contribution of the period for run base calibration data taking done at the beginning of each run. The average ratio is calculated to be 98.1 %.

5.4. Fiducial Volume Selection

In order to determine precise event rate of ^{7}Be solar neutrinos, precise understanding of larger background events is important. Among those background events, external events
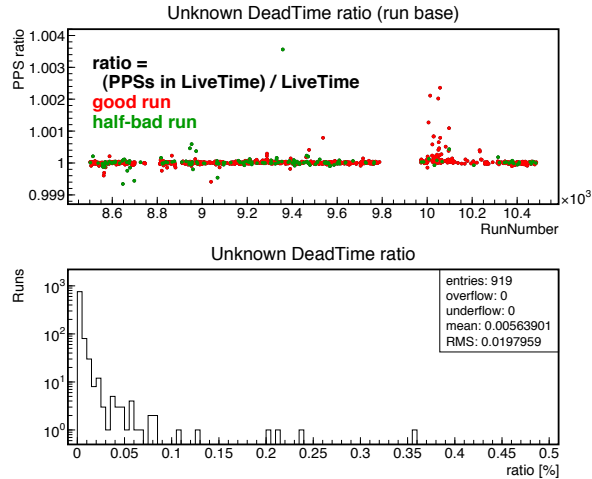
Figure 5.10.: Unknown Deadtime ratio. Unknown deadtime ratio is defined as ratio of number of 1PPS trigger events inside livetime to duration of livetime. The deviation of the ratio from one can be interpreted to the uncertainty of livetime. The upper graph shows the trend of the ratio for the ^{7}Be solar neutrino analysis period. The half-bad runs basically have worse deviation. It is confirmed that the larger ratio around run 10050 in good runs are due to false issue of PPS triggers. The lower graph shows the histogram of deviation of the ratio from one. The average deviation is calculated to be 5.6×10^{-3} %.

and internal ^{210}Bi events require the most careful treatment. Effective volume selection enables better treatment of those background and the volume is called Fiducial Volume.

5.4.1. Radius Volume Selection

Although KamLAND consists the active buffer with the mineral oil region as well as the water Cherenkov detector, inbound γ events are detected inside the liquid scintillator. Such external γ events are originated from the KamLAND balloon film and ropes, glass of the PMT surfaces, stainless steel shell of the KamLAND internal detector wall, and the surrounding rocks. Since these γ particles fly long distance and different medium, modeling of the expected position and energy of the events are not so accurate. Hence preliminary background suppression is important. Figure 5.11 shows the energy distribution with different radius cuts. In the larger radius cut, γ events from ^{40}K and ^{208}Tl events are prominent, while the smaller radius cut, e.g. 4.5 m, effectively suppress ^{40}K.

External ^{40}K γ is background against ^{11}C, which should be well evaluated, since for ^{7}Be solar neutrino fitting, determination of ^{11}C is important for following 3 reasons.

- ^{11}C is background of ^{210}Bi, which is the most dominant background against ^{7}Be solar neutrinos.
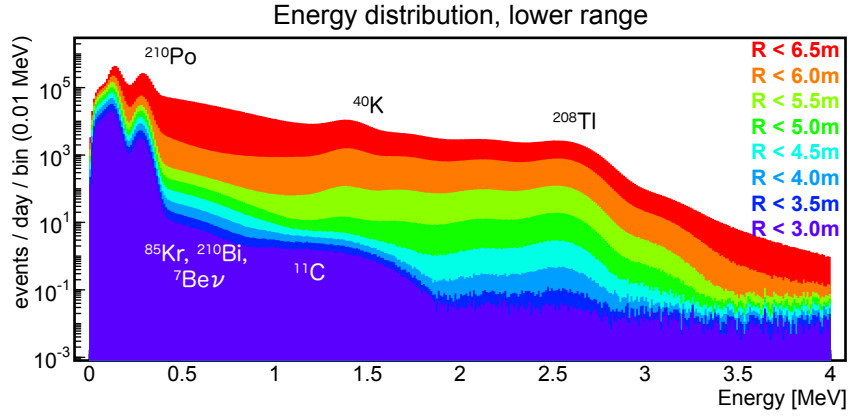
Figure 5.11.: Energy distribution in different radius sphere. In larger radius sphere, external γ events such as ^{40}K and ^{208}Tl are prominent.

- ^{11}C is background of internal ^{40}K γ, whose β decay of 90 % branch, overwhelmed by ^{210}Bi i s one of the important background against ^{7}Be solar neutrinos.

- ^{11}C determines and corrects volume bias of the ranked data sets introduced in the next section.
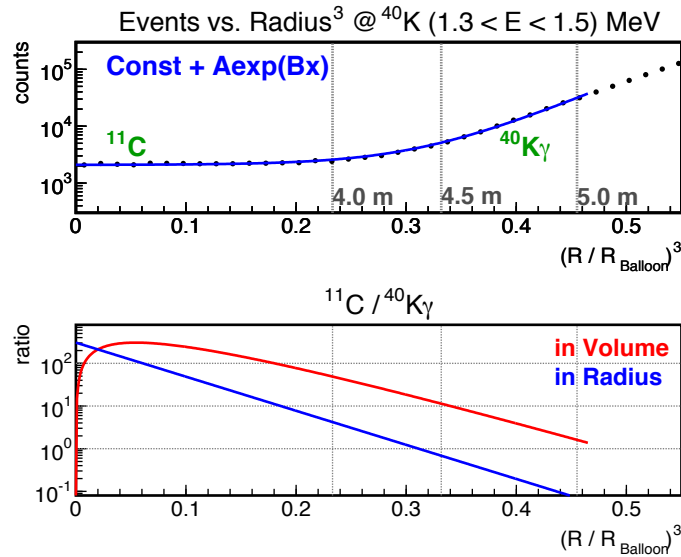
Figure 5.12.: Energy distribution in different radius sphere. In larger radius sphere, external γ events such as ^{40}K and ^{208}Tl are prominent.

Figure 5.12 shows the radius distribution of events in ^{40}K γ energy range and shows the contribution of external components to internal components. Assuming that there are

only ^{11}C and external ^{40}K γ in the energy range, third power radius distribution, in which volume of each bin is the same, is fit by a constant value and an exponential function. The ratio of the contribution of the constant component, ^{11}C to the contribution of the exponential component, ^{40}K γ is evaluated, and from the contribution ratio in volume, 4.5 m radius is selected as a preliminary cut, with considering S/N of ^{11}C/^{40}K γ.

The systematic uncertainty given from the radius cut is evaluated with the vertex reconstruction bias. From the vertex reconstruction calibration described in the previous chapter, the bias is evaluated less than $\pm$ 5 cm at 4.5 m radius. This radius bias gives the bias of the volume of a 4.5 m radius sphere as +3.37 % -3.30 %, hence the systematic uncertainty of 4.5 m radius cut is conservatively applied 3.37 %.

5.4.2. Volume Classification

^{7}Be solar neutrinos interact with KamLAND liquid scintillator by electron scattering. The possible main backgrounds events against them are ^{210}Bi and ^{85}Kr, which decays with beta particle emission with Q value of 1.162 MeV and 0.687 MeV respectively then make similar energy distribution. Since the event rate of ^{7}Be solar neutrinos are only measured by fitting energy spectrum ^{210}Bi and ^{85}Kr should be well suppressed.

The distillation of liquid scintillator was meant to reduce them and parent particles of ^{210}Bi such as ^{226}Ra. At the beginning of ^{7}Be solar neutrino observation period ^{210}Bi and ^{85}Kr was well reduced in order to fit ^{7}Be energy spectrum at the center of the detector. Later there were many times of obvious influx of low energy events from near the balloon and the energy shape reveals that the source is mostly ^{210}Bi. The influx was basically triggered by thermal destabilization of KamLAND detector, e.g. by reduction of cooling water flow. Influx occurred at various positions and the intensity of it or the duration it occurred were also various, then the position with high or low ^{210}Bi event rate always varied. In Figure 5.13, such variation and influx is shown.

In order to determine ^{7}Be solar neutrino event rate precisely, determination of fiducial volume with high signal to background ratio is important. The earlier studies (Keefer, 2009, Nakajima, 2009, Grant, 2011, Xu, 2011) tried to utilize only low ^{210}Bi event rate region with time dependent fiducial volume. However, the selection might have induced unindented bias on event rate of ^{7}Be solar neutrinos. Selection basis of ^{210}Bi event rate is simply event rate in energy window between 0.6 MeV and 0.9 MeV which includes ^{7}Be solar neutrino event rate as well, thus the selection could focus region where ^{7}Be solar neutrino event rate is statistically low. Furthermore, non-spherical surface of fiducial volume emerged with the selection could complicate the volume bias due to vertex reconstruction bias, and it is difficult to evaluate the bias.

In this analysis, exclusion of those possible biases is considered while enhancement of higher S/N region is also considered, and the scheme of the analysis is summarized as follows,

- Use of all events inside a sphere of specified radius, 4.5m.

- Classification of data set with respect to the S/N ratio.
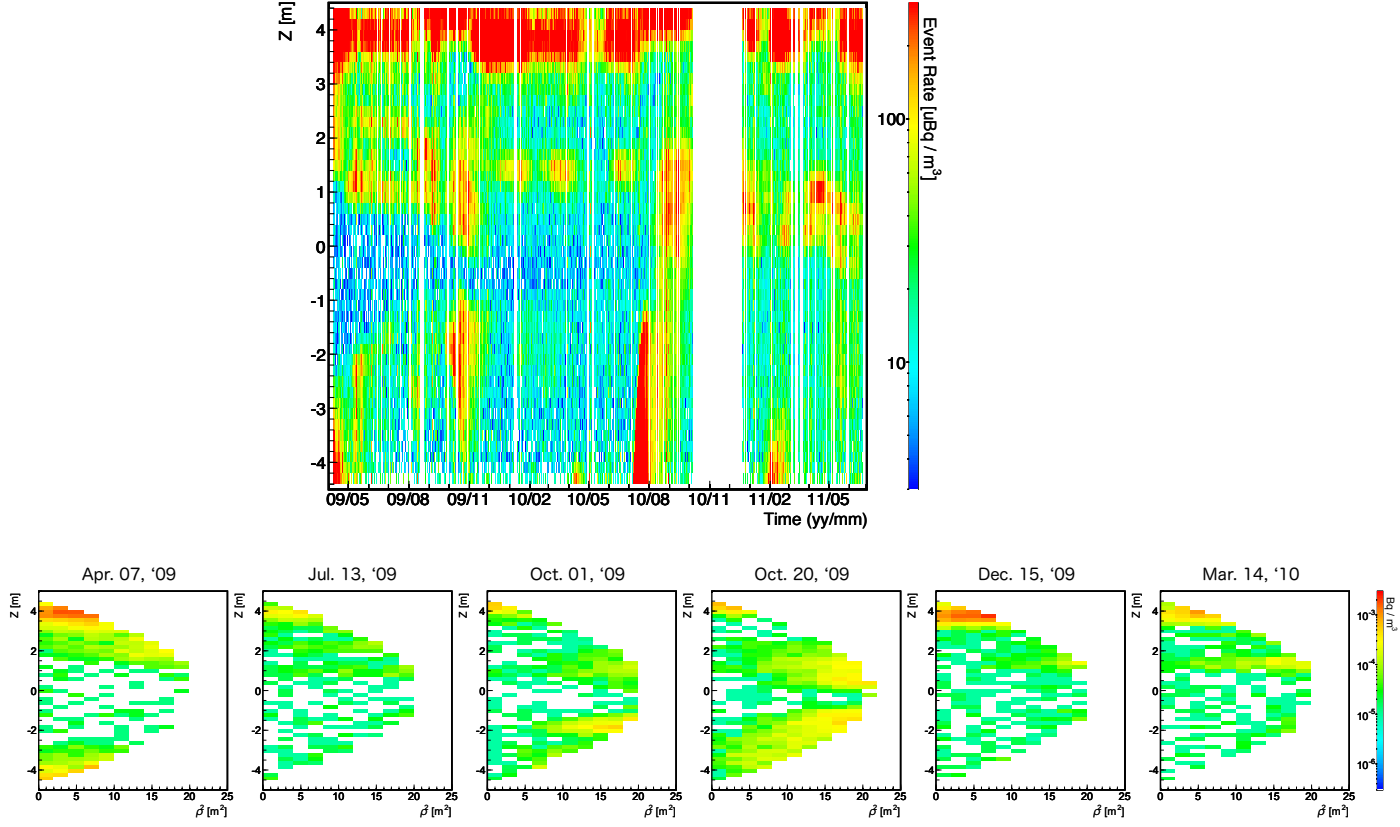
Figure 5.13.: Vertex distribution and event rate trend of low energy ($0.5 \leq E < 0.8$ MeV) event in the sphere of 4.5 m radius. In the upper graph, z-axis event rate trend is shown. The lower graphs show typical vertex distribution of the evens in the first year. The left edge of the upper graph corresponds to the first graph from the left in the lower graphs, when extremely low background region exists at $-2 < z < 1$ m, while there is higher background region at $z < -3$ m or at $3 < z$ m. In the second from the left in the lower graph, the higher background region at $z < -3$ m mostly has decayed out, while influx exits at $z \sim 1$ m. In the third to fifth graphs from the left in the lower graphs show growth and decay of large influx occurred at $z \sim 1$ m and $z \sim -2$ m.

- Simultaneous energy spectrum fitting of multiple data from different classes.

In order to realize the scheme, classification is done by following procedure.

1. Division of volume into slices.
   The sphere of 4.5 m is sliced into small torus shape volume, whose radius width (ρ) and height (z) is defined as follows so that all slices have the same volume.
   $\rho^2 = (x^2 + y^2) = 2$ m^2, $z = 0.2$ m.

The temporal length of a slice is duration of a run, thus it varies with runs.

2. Determination of representative event rate of slices.
   Event rate of a slice for classification is not the event rate of the slice itself in order to exclude the selection bias described above. Is is defined as *representative event rate* which is calculated by event rate of the adjacent slices. At most eight spatially adjacent slices in the same run and the slices located at the same position in the different runs within one day distance. For this event rate counting, events whose energy is from 0.5 MeV to 0.8 MeV are used so that contribution at ^{7}Be solar neutrino energy is classified.

3. Classification of slices.
   The slices inside the 4.5 m sphere in the observation period is classified by the representative event rate of the slices into seven classes called *Ranks*. Typical classification in a run is shown in Figure 5.14. The criteria of event rate is specified so that exposure of difference among ranks is less than one order of magnitude. The energy histograms from rank fiducial volume is showin in Figure 5.15. The criteria and exposure is summarized in the same figure.
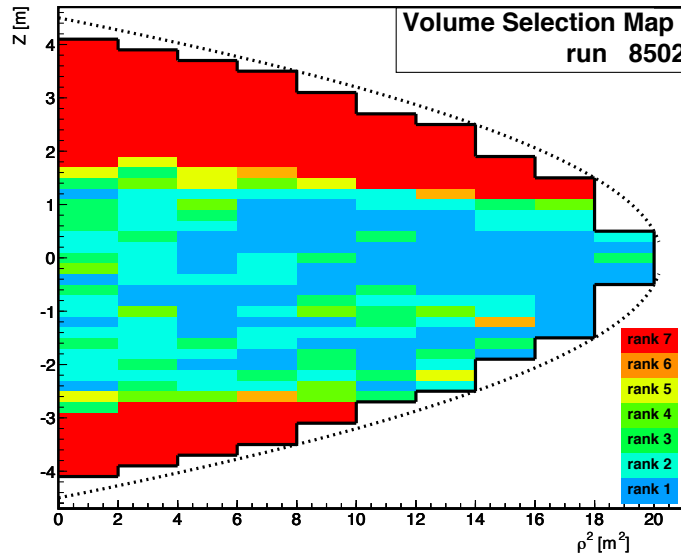
Figure 5.14.: Typical classification of slices. Each slice inside 4.5 m radius sphere in a run is classified into either of seven ranks. The dashed line shows the 4.5 m radius.

The total volume used in a run is 344.3 m^3, which is the sum of the volume of 274 slices, which is smaller by approximately 10 % than the volume of 4.5 m radius sphere. The volume division into slices accompanies uncertainty of event selection in a slice, which propagates to the uncertainty of volume of a rank. The uncertainty could be evaluated with a uniformly distributed events such as spallation products. One candidate could

95
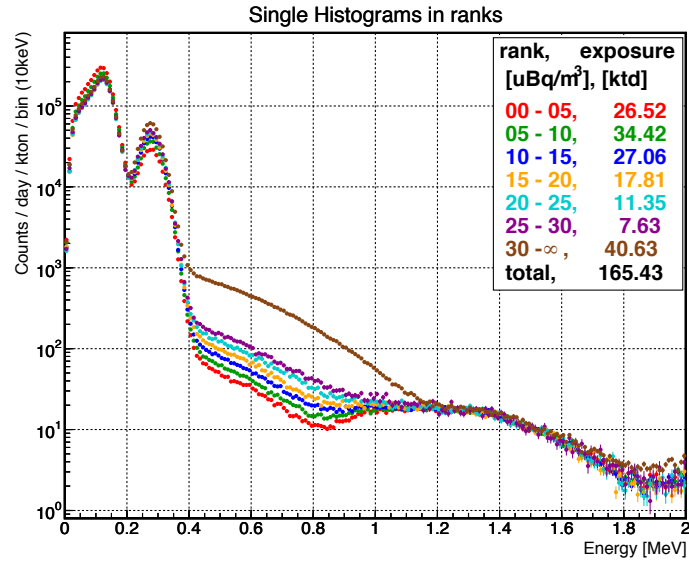
Figure 5.15.: Data energy histograms from summarized ranked fiducial volumes. These histograms are used in energy spectrum fitting simultaneously.

be ^{12}B, however the statistics are too small to evaluate it. The other candidate could be neutrons generated with spallation products, however the event rate of the same small slice varied in different occasions and thus they are not suitable for the evaluation of the uncertainty. For this reason, the uncertainty is not evaluated independently. Instead, it is included in the energy spectral fit for the evaluation of the ^{7}Be solar neutrino event rate and is calibrated by uniformly distributed event in the range; mainly ^{11}C. This is described in detail in Chapter 7.

5.5. Number of Targets

The number of electron targets for the electron scattering by solar neutrinos is calculated from the components of the liquid scintillator. The chemical composition of the liquid scintillator is as follows.

Dodecane $(C_{12}H_{26}$ [170.335 g/mol])   : 80.2 % (0.7526 g/cm^3 @ 15 °C)
Pseudocumene $(C_9H_{12}$ [120.192 g/mol])   : 19.8 % (0.8796 g/cm^3 @ 15 °C)
PPO $(C_{15}H_{11}NO$ [221.254 g/mol])   : 1.36 ± 0.03 g/l
.

The number of protons, N_H per unit liquid scintillator mass is obtained with following equation,

$$\frac{N_H}{\text{Mass of LS [g]}} = \frac{N_A}{\text{RAM}_H} + \text{RAM}_C \cdot \text{R(C/H)} + \text{RAM}_N \cdot \text{R(N/H)} + \text{RAM}_O \cdot \text{R(O/H)} \quad (5.2)$$

, where N_A corresponds to Avogadro constant, RAM_X corresponds to the relative atomic mass of a element, X and R(X/H) corresponds to the ratio of the number of a element X to that of proton. The number of carbon, nitrogen and oxygen are also calculated in the same way. The number of electron targets is calculated from those numbers. Those numbers are summarized in Table 5.5. The uncertainty from the PPO concentration uncertainty, 0.03 g/l, is calculated to be 0.0003 %.

Table 5.4.: Number of targets in KamLAND

Element	Number per kton
H	8.4706×10^{31}
C	4.3019×10^{31}
N	4.7512×10^{27}
O	4.7512×10^{27}
e^-	3.4289×10^{32}

The measured density of the liquid scintillator is 0.77754 ± 0.0002 g/cm^3 at 15 °C, which is the result from measurements during liquid scintillation installation during KamLAND construction. The temperature coefficient of expansion is measured with a pycnometer to be 7.41×10^{-4} g/cm^3/K (Mitsui, 2002). Since the average temperature of the KamLAND liquid scintillator is 11.5 °C, the average density is estimated to be 0.78013 g/cm^3. The temperature distribution in KamLAND was measured (Berger et al., 2009) and is shown in Fig.5.16 . The volume weighted average of the density change due to the temperature gradient is calculated to be 0.1 % (Winslow, 2008:p57). For materials similar to pseudocumene and dodecane, the maximum isothermal compressibility, $\Delta V/V$, is 0.01 % (Bolz and Tuve, 1991), which corresponds to a density uncertainty of 0.01 %. Uncertainty of the number of targets due to solution of nitrogen and oxygen is negligible (Winslow, 2008:p57).

The density variation after the 2nd purification is considered (Nakajima, 2009). Assuming that the liquid scintillator density in KamLAND has a layered structure, and

that the temperature of the liquid scintillator is 11.5 °C, the average density is estimated to be 0.78013 ± 0.00020 g/cm^3 at 15 °C. This corresponds to 0.025 % uncertainty.

The total number of electron targets in a unit volume is given by

$$N_{\mathrm{e}^-}[\mathrm{m}^{-3}] = 2.6750 \times 10^{29}, \tag{5.3}$$

which corresponds to 9.211×10^{31} electron targets in the fiducial volume. Total uncertainty is 0.104 % and the contribution to the uncertainty is summarized in Table 5.5.
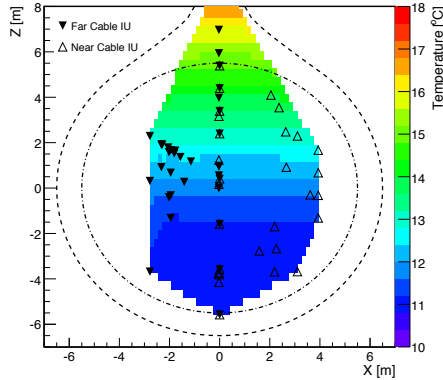
Figure 5.16.: The temperature distribution in KamLAND liquid scintillator (Berger et al., 2009).

Table 5.5.: Systematic uncertainties in the number of electron targets

Source	Uncertainty
PPO concentration	0.003 %
Temperature gradient	0.10 %
Thermal expansion	0.01 %
Gas solution	negligible
Density distribution	0.025 %
Total	0.10 %

5.6. Total Detector Related Uncertainty

From the estimation of uncertainty or inefficiency in this and previous chapters, total detector related uncertainty is summarized in Table 5.6.

Table 5.6.: Total Detecter Uncertainty

Source	Uncertainty
Cross Section	1.0 %
Energy Scale	2.0 %
Flasher Event Cut	5.0×10^{-4} %
Missing Waveform Cut	7.6×10^{-3} %
Poorly Reconstructed Event Cut	1.4×10^{-2} %
Livetime calculation	5.6×10^{-3} %
Fiducial Volume Selection	3.4 %
Number of Target	0.10 %
Total	4.1 %

6. Background

6.1. Background Study for Single Events

As described in the section Fiducial Volume Selection, there was almost always position dependent variation of background events inside the fiducial volume during observation period of ^{7}Be solar neutrinos mainly due to convection of the liquid scintillator triggered by destabilization of thermal equilibrium in the detector. The were obvious trace of dominant background, ^{210}Bi with the convection but it is difficult to measure independently the distribution or the variation of distribution of less dominant background sources. Thus, some of the backgrounds are not measured but fitted with ^{7}Be neutrino in the next chapter. In this chapter, the results of measurement of a background source or the treatment of is described.

The background source against ^{7}Be solar neutrino is categorized into mainly four; radioactive impurities, spallation products induced by muons, external γ events and pileup events.

The radioactive impurities includes ^{238}U and ^{232}Th and their daughters includes ^{210}Bi. It also includes noble gas such as ^{85}Kr or ^{39}Ar and other background such as ^{40}K.

The spallation products includes isotopes which has relatively longer life time compared to two ms veto after a muon described in the previous chapter. The main background sources against ^{7}Be solar neutrino among them is ^{11}C and ^{7}Be.

The external γ events is described in the section Fiducial Volume Selection. Remaining events after radius cut is described here.

The pileup events can be the source of poorly constructed events as briefly described in the section Poorly Reconstructed Event. The nature of the pileup events and the implementation is described here.

6.2. Radioactive Impurities

6.2.1. ^{238}U Series

Uranium is a natural element and ^{238}U is a radioactive isotope which has 99.3 % natural abundance in Uranium. The decay chain from ^{238}U to ^{206}Pb is called the "Uranium series". It is a permanent source of alpha, beta and gamma rays because of the long half life of ^{238}U, 4.5 billion years. A schematic of the ^{238}U decay series is shown in Appendix A. With the second purification of the liquid scintillator, the radioactive equilibrium of the ^{238}U chain is broken. It is confirmed that the radioactive equilibrium between ^{210}Bi and ^{210}Po is broken. Hence it is necessary to evaluate the activity of each of following sub-chain separately:

- ^{238}U → ^{234}U (^{238}U : 4.468 × 10^9 year)
  This amount can be evaluated via energy spectrum of ^{234}Pa (Q$_\beta$ = 2.27 MeV).

- ^{234}U (^{234}U: 2.455 × 10^5 year)
  ^{234}U emits α rays with Q$_\alpha$ = 4.86 MeV , which can be ignored since the α ray energy is lower than that of ^{210}Po (Q$_\alpha$ = 5.41 MeV), and since the event rate is much lower than that of ^{210}Po.

- ^{230}Th (^{230}Th : 7.538 × 10^4 year)
  ^{230}Th emits α rays with Q$_\alpha$ = 4.77 MeV, which can be ignored by the same reason as in case of ^{234}U.

- ^{226}Ra → ^{210}Pb (^{226}Ra : 1.6 x 10^3 year)
  This amount can be evaluated by the delayed coincidence rate of ^{214}Bi and ^{214}Po.

- ^{210}Pb → ^{206}Po (^{210}Pb : 22.3 year)
  ^{210}Bi and ^{210}Po can be evaluated separately via their energy spectra.

^{238}U - ^{234}U

The theoretical visible energy spectrum from ^{238}U to ^{234}U is shown in Figure 6.1 The beta rays from ^{234}Pa are distinct among these isotopes, and can be used to evaluate the ^{238}U–^{234}U activity. The most dominant background against ^{234}Pa is ^{11}C. Theoretically, ^{11}C can be tagged and removed by the three-fold coincidence of a muon, a neutron capture gamma ray, and an event with energy of a ^{11}C decay. During data period of this analysis, the neutron capture rate is not stable among rank fiducial volumes of different time, which could introduce serious bias on the event rate of the dominant ^{11}C, thus the thee-fold coincidence method is not employed. The event rate of ^{234}Pa is evaluated simultaneously with ^{7}Be solar neutrino evaluation in the next chapter.
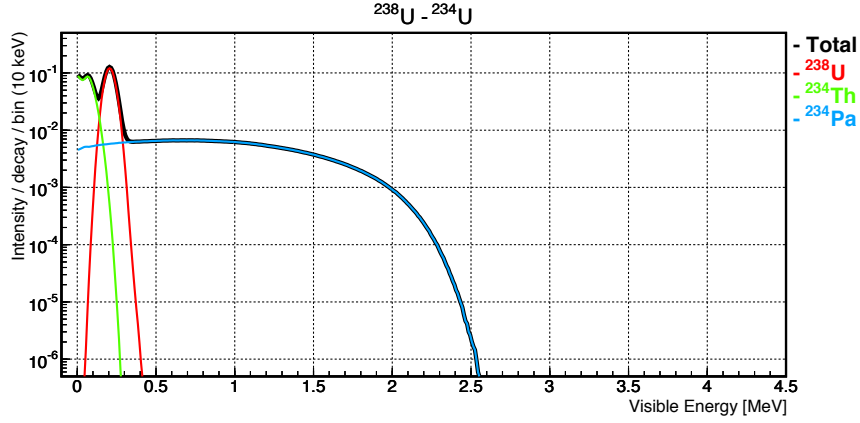
Figure 6.1.: The theoretical visible energy spectrum from ^{238}U to ^{234}U

^{214}Bi–^{214}Po

The decay chain from ^{214}Bi to ^{210}Pb is as follows,
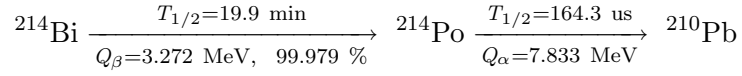
$$^{214}\text{Bi} \xrightarrow[Q_\beta=3.272 \text{ MeV}, \ \ 99.979\ \%]{T_{1/2}=19.9 \text{ min}} {}^{214}\text{Po} \xrightarrow[Q_\alpha=7.833 \text{ MeV}]{T_{1/2}=164.3 \text{ us}} {}^{210}\text{Pb}$$

The selection criteria and corresponding efficiencies and systematic uncertainties for ^{214}Bi–^{214}Po delayed coincidence are summarized in Table 6.1. In the time correlation cut, $\Delta T \geq 5$ us is applied to avoid ^{212}Bi–^{212}Po coincidence events (half-life of ^{212}Po is 299 nsec).

Table 6.1.: ^{214}Bi–^{214}Po event selection criteria and corresponding detection efficiency

Type	Selection	Efficiency [%]	Uncertainty (Syst.) [%]
Prompt Energy (E_p)	$0.35 \leq E_\text{p} < 3.5$ MeV	98.0 ± 0.04	0.028
Delayed Energy (E_d)	$0.35 \leq E_\text{d} < 0.8$ MeV	~ 100	negligible
Distance (ΔR)	$\Delta R < 1.2$ m	99.4 ± 0.0	0.203
Interval (ΔT) On Time	$5 < \Delta T < 1200$ us	97.3 ± 0.01	0.015
Interval (ΔT) Off Time	$1205 < \Delta T < 2400$ us		
Fiducial Volume	($R < 4.5$m)		3.37
Total		94.8 ± 0.04	3.38

The calculation method is as follows;

- Prompt Energy   Calculation of the number of MC events in the prompt energy window when scaling the energy $\pm$ 1.6 %.
- Delayed Energy   Same as prompt energy. Since the delayed energy window is sufficiently wide, there is almost no difference in the event counts.
- Space Correlation Calculation of the number of MC events in the space correlation taken account of the vertex and energy resolution 12.8 cm/$\sqrt{MeV}$ and 6.9 %/$\sqrt{MeV}$ respectively.
- Time Correlation Calculation of the change of the efficiency when the half life is varied within its uncertainty, $T_{1/2} = 164.3 \pm 2.0$ us.
- Fiducial Volume Calculation of the volume with assuming a vertex bias of 5 cm at 4.5 m radius, obtained from the off axis calibration data.

Figure 6.2 shows the MC energy spectrum for decays from ^{226}Ra to ^{210}Pb. The veto inefficiency (1 - 0.948) of ^{214}Bi–^{214}Po and that of close event is considered in the spectrum.

Figure 6.2.: The theoretical visible energy spectrum from ^{226}Ra to ^{210}Pb. ^{214}Bi and ^{214}Po spectrum are scaled to meet their tagging inefficiency, (1 - 0.948) and then scaled to meet the efficiency of close event rejection described in the previous chapter.

Figure 6.3 shows a typical sample of ^{214}Bi–^{214}Po coincidence events, which were collected during the livetime. The interval distribution is fit with a formula

$$f(t) = \frac{N}{\tau} \exp(-t/\tau) + Background. \tag{6.1}$$

The half life is evaluated to be 158.7 ± 4.5 us. The ^{214}Bi–^{214}Po events vertex distribution is shown by the distribution of ^{214}Po in Figure 6.4, where events satisfying all selections are shown.
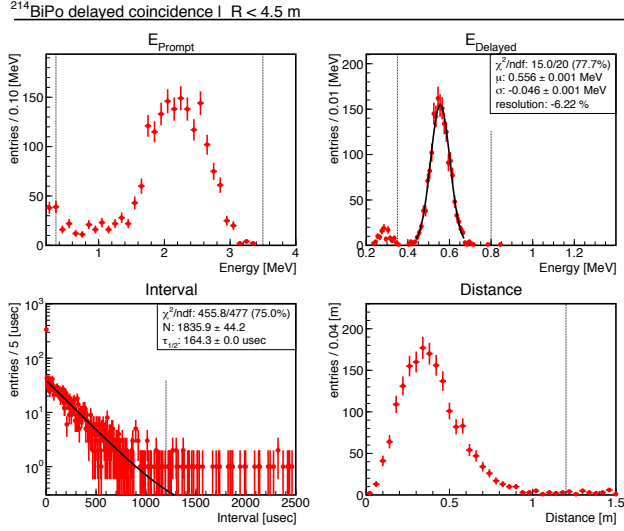
Figure 6.3.: ^{214}Bi–^{214}Po event selection in 4.5 m radius. The dotted lines in each graphs indicate the selection criteria in Table 6.1.
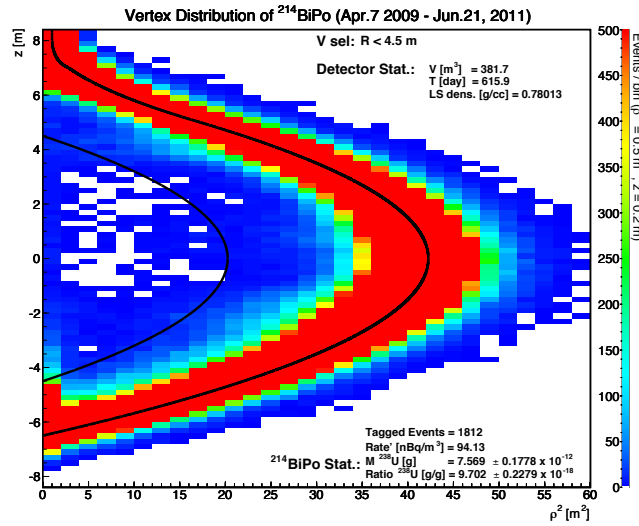
Figure 6.4.: ^{214}Bi–^{214}Po event distribution. The internal solid black line indicates 4.5 m radius, and the external one indicates 6.5m radius.

The time variation of ^{214}Bi–^{214}Po event rate inside on-time window is shown in Figure 6.5. Event rate inside 4.5 m radius is averagely 10^{-1} uBq/m^3.

In order to evaluate the number of ^{214}Bi–^{214}Po events, which is N in Eqn. 6.1, $\tau_{1/2}$ is fixed to 164.3 us. The counted event is (1835.9 ± 44.2) events, which corresponds to ^{226}Ra concentration of (92.8 ± 3.9) nBq/m^3 and ^{238}U concentration of $(4.97 \pm 0.21) \times$
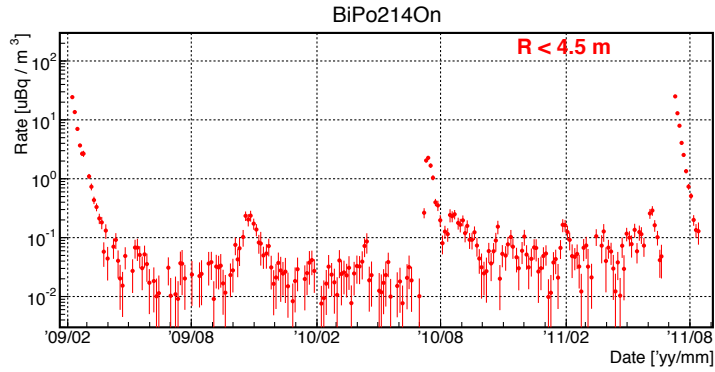
Figure 6.5.: Three-day average of ^{214}Bi–^{214}Po event rate trend in 4.5 m radius. Apr. 2009 to Jun. 2011 is the period for ^{7}Be solar neutrino analysis. Prior to the period, high rate events after liquid scintillator purification is overwhelming. On the other hand, posterior to the period, high rate events due to mistaken installation of insufficiently purified liquid scintillator is overwhelming. At around Nov. 2009 and Jul. 2010, high event rate periods appeared due to the convection of the liquid scintillator, triggered by the thermal destabilization.

10^{-18} g/g under the assumption of secular radioactive equilibrium. In the solar neutrino analysis, event rate of ^{214}Bi–^{214}Po is evaluated for each rank fiducial volume with the same calculation done in the evaluation for event rate in 4.5 m radius. The event rate is summarized in Table 6.2. From the data set, the tagged events are removed in advance and the residual rate of events and the other decays of the decay chain is evaluated with constraint in the spectral fit for the ^{7}Be solar neutrino event rate analysis. The spectrum used for the fit is the total spectrum the Figure 6.2.

Table 6.2.: ^{214}Bi–^{214}Po event rate in Rank FV as ^{226}Ra rate

Rank	Event Rate [nBq/m^3]	Uncertainty (Stat.) [%]
1	8.21	20.8
2	14.5	14.5
3	19.3	14.2
4	24.4	14.7
5	32.5	16.0
6	45.2	17.3
7	250	3.11
total	75.9	2.81

105

6.2.2. ^{232}Th Series

Thorium is a natural element and comprised almost exclusively of ^{232}Th. The half life of ^{232}Th is very long, 14 billion years, and the disintegration rate of ^{232}Th is lower than ^{238}U, 4.06×10^3 Bq/g. The decay chain from ^{232}Th to ^{208}Pb is called the "Thorium series" (^{232}Th series). A schematic of this decay chain is shown in Appendix A.

The concentration of ^{232}Th in the liquid scintillator can be estimated from the ^{212}Bi–^{212}Po coincidence event rate. The selection criteria and corresponding efficiencies and systematic uncertainties for ^{212}Bi–^{212}Po delayed coincidence are summarized in Table 6.3. In the time correlation cut, since there is dead time within 300 nsec of a previous event, $\Delta T > 0.4$ us is applied. The calculation method for the efficiencies and uncertainties is the same as ^{214}Bi–^{214}Po.

Table 6.3.: ^{212}Bi–^{212}Po event selection criteria and corresponding detection efficiency

Type	Selection	Efficiency [%]	Uncertainty (Syst.) [%]
Prompt Energy (E_p)	$0.35 \leq E_\mathrm{p} < 2.5$ MeV	83.2 ± 1.42	0.34
Delayed Energy (E_d)	$0.50 \leq E_\mathrm{d} < 1.0$ MeV	~ 100	negligible
Distance (ΔR)	$\Delta R < 1.0$ m	97.8 ± 0.0	0.20
Interval (ΔT) On Time	$0.4 < \Delta T < 2.5$ us	39.3 ± 0.23	0.23
Interval (ΔT) Off Time	$2.9 < \Delta T < 5.0$ us		
Fiducial Volume	($R < 4.5$m)		3.37
Total		31.9 ± 0.58	3.40

Figure 6.6 shows the MC energy spectrum for decays from ^{232}Th to ^{208}Pb. The veto inefficiency of ^{212}Bi and ^{212}Po, $0.6406 \times (1 - 0.319)$ is considered in the spectrum, where 0.6406 is the branching ratio from ^{212}Bi to ^{212}Po and 0.319 is the selection efficiency. The veto inefficiency of close event cut is also considered in the spectrum.

Figure 6.7 shows a typical sample of ^{212}Bi–^{212}Po coincidence events, which were collected during the livetime. The half life is evaluated to be 267.5 ± 20.8 ns. The ^{212}Bi–^{212}Po events vertex distribution is shown by the distribution of ^{212}Po in Figure 6.8, where events satisfying all selections are shown.

The time variation of ^{212}Bi–^{212}Po event rate inside on-time window is shown in Figure 6.9. Event rate inside 4.5 m radius is averagely 10^{-2} uBq/m^3.

In order to evaluate the number of ^{212}Bi–^{212}Po events, which is N in Eqn. 6.1, $\tau_{1/2}$ is fixed to 299 ns. The counted event is (623.4 ± 41.0) events, which corresponds to ^{232}Th concentration of (58.9 ± 4.4) nBq/m^3 and $(12.9 \pm 1.0) \times 10^{-18}$ g/g under the assumption of secular radioactive equilibrium.

In the solar neutrino analysis, event rate of ^{212}Bi–^{212}Po is evaluated for each rank fiducial volume as ^{214}Bi–^{214}Po. The event rate is summarized in Table 6.4. From the data set, the tagged events are removed in advance and the residual rate of events and the other decays of the decay chain is evaluated with constraint in the spectral fit for
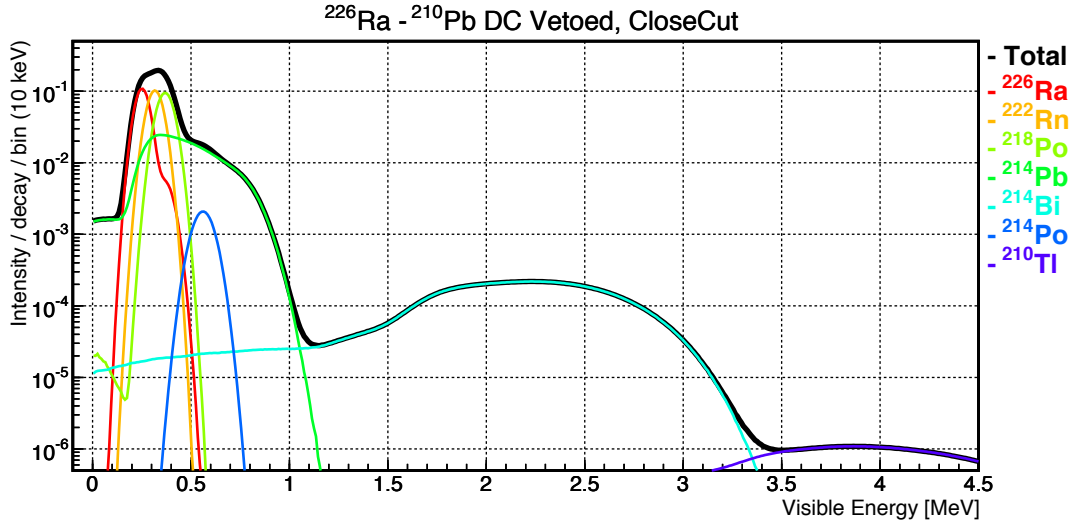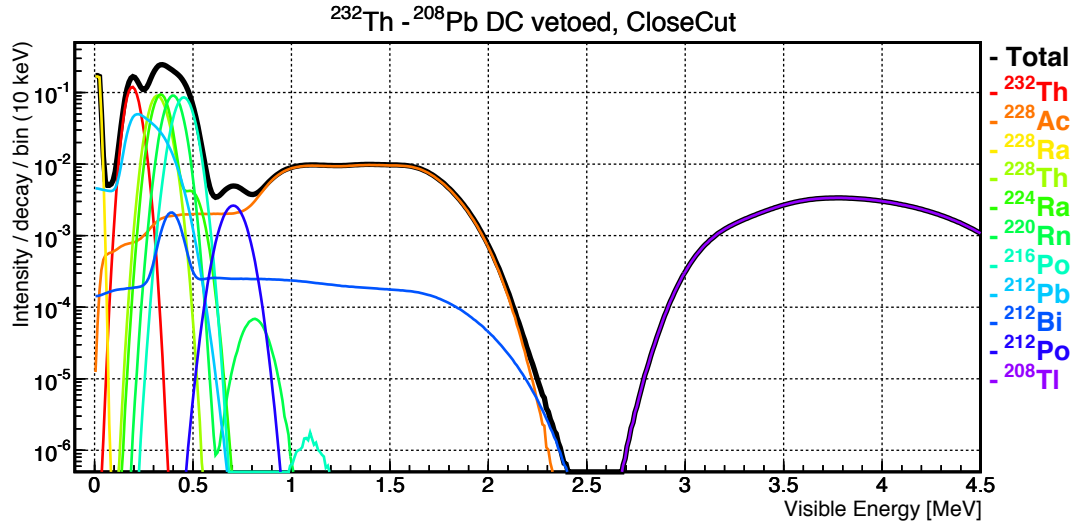
Figure 6.6.: The theoretical visible energy spectrum from ^{232}Th to ^{208}Pb. ^{212}Bi and ^{212}Po spectrum are scaled to meet their tagging inefficiency, (1 - 0.319) , and their branch ratio, 64.06 %, and then scaled to meet the efficiency of close event rejection described in the previous chapter.
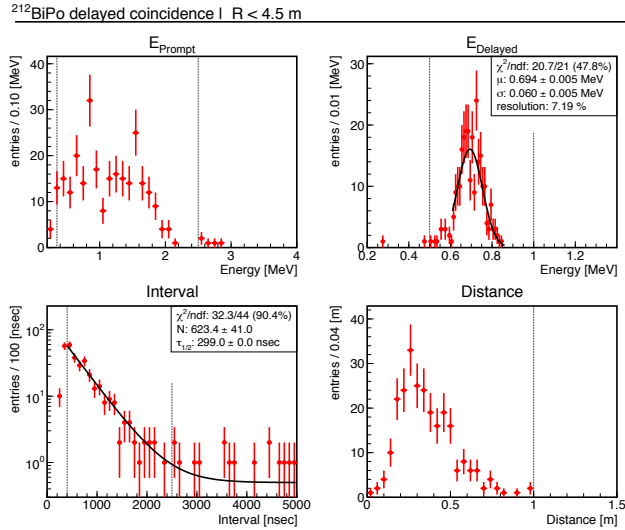
Figure 6.7.: ^{212}Bi–^{212}Po event selection in 4.5 m radius. The dotted lines in each graphs indicate the selection criteria in Table 6.3.

the ^{7}Be solar neutrino event rate analysis. The spectrum used for the fit is the total spectrum the Figure 6.6.

107
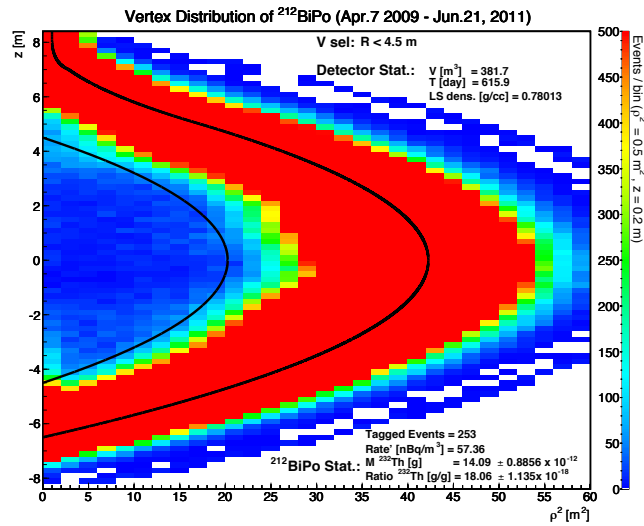
Figure 6.8.: ^{212}Bi–^{212}Po event distribution. The internal solid black line indicates 4.5 m radius, and the external one indicates 6.5m radius.
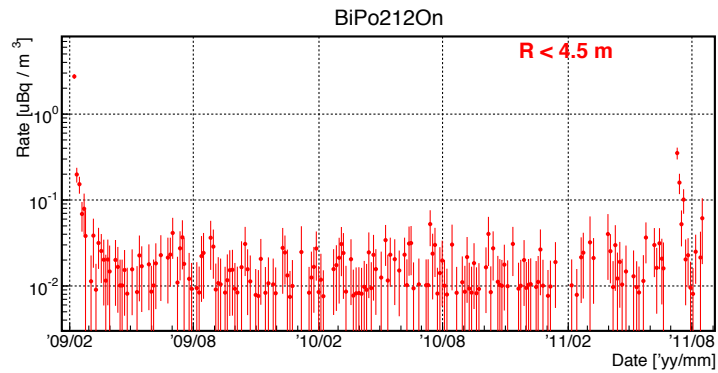
Figure 6.9.: Three-day average of ^{212}Bi–^{212}Po event rate trend in 4.5 m radius. Apr. 2009 to Jun. 2011 is the period for ^{7}Be solar neutrino analysis.

Table 6.4.: ^{212}Bi–^{212}Po event rate in Rank FV as ^{232}Th rate

Rank	Event Rate [nBq/m^3]	Uncertainty (Stat.) [%]
1	46.7	19.2
2	81.6	12.5
3	61.6	16.2
4	36.9	25.8
5	50.2	27.7
6	92.0	25.0
7	55.5	15.2
total	60.4	6.80

6.2.3. ^{210}Bi

^{210}Bi is a radioactive isotope inside U series and is evaluated in ^{7}Be solar neutrino spectral fit. The beta decay of ^{210}Bi is a first forbidden non-unique transition $[^{210}\text{Bi}(1^-) \rightarrow ^{210}\text{Po}(0^+)]$ and the proper correction to the allowed transition is required to reproduce a valid visible energy spectrum. Since the β spectrum of ^{210}Bi is already dominant in the data spectrum, ^{210}Bi shape difference is quite affective for the determination of ^{7}Be solar neutrino spectrum.

^{210}Bi correction in literatures

The probability of beta decay emitting an electron of energy between W and $W + dW$ is described as

$$w(W)dW = \frac{g^2 m_e^5 c^4}{2\pi^3 \hbar^7} |M_{if}|^2 F(\pm Z, W) pW(W_0 - W)^2 dW, \tag{6.2}$$

where W, W_0, p is total electron energy, end-point energy, electron momentum in the electron mass units respectively, g is the coupling constant for the weak interaction, $|M_{if}|$ is a nuclear matrix element, $F(\pm Z, W)$ is Fermi function. The plus sign in front of Z is for β^- decay and the minus sign for β^+ decay. $|M_{if}|$ is independent to electron energy for an allowed transition, and is dependent for a forbidden transition. Hence Equation 6.2 is re-written as

$$w(W)dW = C(W)F(\pm Z, W) pW(W_0 - W)^2 dW, \tag{6.3}$$

where again, $C(W)$ is only variable for a forbidden transition and is called β shape-factor.

The correction models of $C(W)$ are provided in different experiments (Daniel, 1961, Carles and Malonda, 1995, Carles, 2005). Daniel uses $C(W)$ of

$$C(W) = const \cdot (1 + aW + b/W + cW^2), \tag{6.4}$$

following (Fujita et al., 1958, Kotani and Ross, 1958). From his experiment using a β spectrometer, he reported $const = 13.25$, $a = 0.578$, $b = 28.466$ and $c = -0.658$ without errors. On the other hand, Carles uses $C(W)$ of

$$C(W) = c_0(1 + c_1 W + c_2 W^2), \tag{6.5}$$

and from his experiment using a liquid scintillator detector, he reported $c_1 = -0.46 \pm 0.01$ and $c_2 = 0.0586 \pm 0.002$ or $c_1 = -0.47 \pm 0.03$ and $c_2 = 0.065 \pm 0.009$ respectively for his two experiments.

It is basically considered a spectrometer experiment has better resolution and thus has better result, however utilizing the Daniel's result might have problem. Figure 6.10 shows various fits to Daniel's shape factor data listed in the literature. In the top graph, Daniel's shape factor function is used. The original function (green) has very poor fit quality ($\chi^2/\text{ndf} = 422.4 / 34$), on the other hand the re-fit function (blue) has better but still poor quality (($\chi^2/\text{ndf} = 63.6 / 34$)). In the middle graph, Carles' shape factor

function is used. The original function (green) has also very poor reproducibility (χ^2/ndf = 281.7 / 35) and the re-fit function (blue) has still very poor fit quality (χ^2/ndf = 167.3 / 35). These results yield that both the Daniel's and Carles' parameterization are inappropriate to reproduce Daniel's data. They also infer that Carles' data is different from Daniel's.
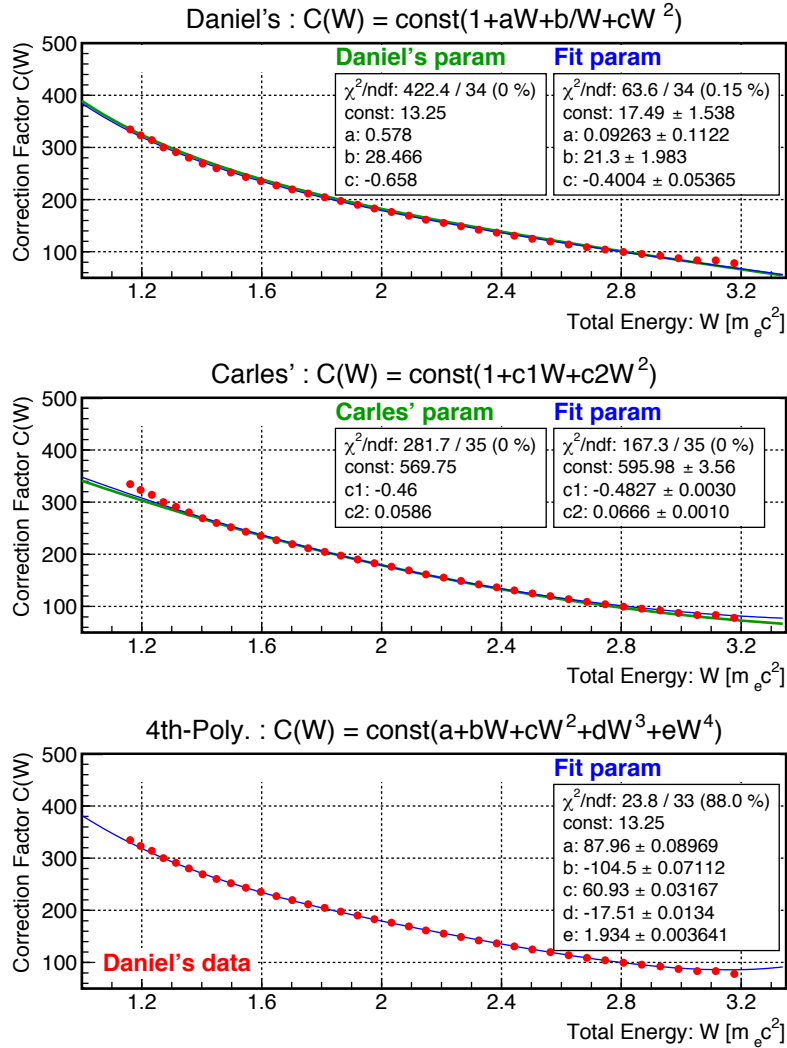
Figure 6.10.: Different shape factor parameterization against Daniel's ^{210}Bi data. In each graph, Daniels's data (red) is fit or drawn is different shape factor functions, Daniel's, Carles's and our 4th order polynomial functions.

^{210}Bi correction in KamLAND

Thus we need to consider two independent issues, a better parameterization for better reproduction of Daniel's data, and inclusion of difference of experiment, that is, the difference of Daniel's and Carles' and also KamLAND. The new parameterization is employed from (Keefer, 2009) as

$$C(W) = c_0(a + bW + cW^2 + dW^3 + eW^4), \qquad (6.6)$$

which is 4th order polynomial function and is the extension of the Carles'. The fit of the function to Daniel's data is shown in the bottom graph of Figure 6.10 and shows much better quality of fit (χ^2/ndf = 23.8 / 33).

On the other hand, the inclusion of the experimental difference is not simple since we don't have shape factor data of Carles nor of KamLAND. Thus we employ another polynomial function to reproduce the deformation from Daniel's data and make it calibrated during ^{7}Be solar neutrino fit by data itself. The function should be ideally multiplied to $C(W)$, e.g. $C'(W) = C(W) \cdot f(W)$. In a practical process a real energy spectrum is generated with a MC code library, KBeta (KamLAND β decay generator) with using $C'(W)$, then a visible energy spectrum is generated with energy scale and energy resolution conversion. This process is time-consuming and it is unrealistic to process this at every time when parameters in $f(W)$ are specified in fitting. Thus, we employ a 4th-order polynomial function for a visible energy spectrum as a shape modulation factor, i.e.

$$^{210}\mathrm{Bi}'_{visible}(E) = {}^{210}\mathrm{Bi}_{visible}(E) \cdot ShapeMod(E) \qquad (6.7)$$

$$= {}^{210}\mathrm{Bi}_{visible}(E) \cdot (1 + \alpha E + \beta E^2 + \gamma E^3 + \delta E^4) \qquad (6.8)$$

The degree of the function is specified as a minimum degree which enables $^{210}\mathrm{Bi}'_{visible}(E)$ generated with Daniel's, Carles' and 4th-order polynomial $C(W)$ get consistent after fitting them to a ^{210}Bi rich data spectrum.

In ^{7}Be solar neutrino analysis, 4 parameters $(\alpha, \beta, \gamma, \delta)$ are floated without a constraint.

6.2.4. ^{40}K

^{40}K is a radioactive metal isotopes. Its natural abundance is merely 0.012 % and its disintegration rate is 2.59 ×10^5 Bq/g. In KamLAND, ^{40}K is found in the balloon film, the suspension kevlar ropes, the glass of the acceptance surfaces of the PMTs and the steel shell and they are discussed as external background sources in the later section in this chapter. ^{40}K is also found in the liquid scintillator even after the purification of it and it is discussed here as internal ^{40}K.

The half life of ^{40}K is 1.3 billion years and it decays via two branches, beta emission (Q_β = 1311.09 keV, 89.14 %), and gamma emission (Q_β = 1504.9 keV, 10.86 %). The decay scheme of ^{40}K is shown in Figure 6.11. and the visible energy spectrum in KamLAND is shown in Figure 6.12.
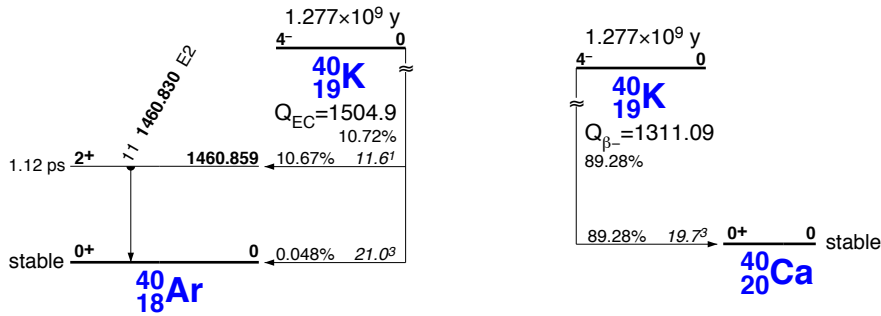
Figure 6.11.: Level diagram for ^{40}K

The internal ^{40}K could be evaluated with removing its significant background source, ^{11}C with performing 3-fold coincidence of cosmic muons, and following neutrons and ^{11}C. Previous analysis (Nakajima, 2009:p159–161) reported 0 consistent event of ^{40}K and 0.9 uBq/m^3 of the upper limit of it with utilizing the method.

Since the neutron tagging rate is not stable among different rank fiducial volume of different time, the method is not applied to ^{7}Be solar neutrino analysis. Instead, ^{40}K is just floated in ^{7}Be solar neutrino spectral fit for each rank fiducial volume. The upper energy of the fit range is set 1.4 MeV in order to include the γ peak of ^{40}K and to fit it precisely.
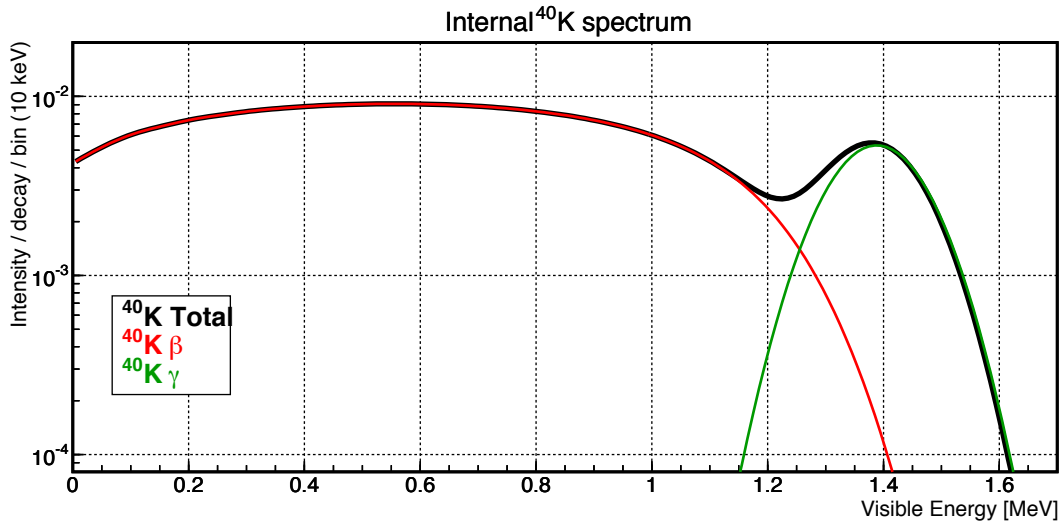
Figure 6.12.: The theoretical visible energy spectrum of ^{40}K. ^{40}K Total is used in ^{7}Be solar neutrino spectral fit.

6.2.5. Noble gas ^{85}Kr and ^{39}Ar

^{85}Kr and ^{39}Ar are radioactive isotopes of noble gases. They have long half-lives and similar Q-values to ^{7}Be solar neutrino's thus are potential background. The fundamental nature of the isotopes is summarized in Table 6.5, where R_{air} means event rate in atmosphere.

Table 6.5.: Nature of ^{85}Kr and ^{39}Ar

Isotope	$T_{1/2}$ [y]	R_{air} [Bq/m^3]	origin
^{85}Kr	10.75	1.6	anthropogenic
^{39}Ar	269	16.8×10^{-3}	cosmogenic

Direct measurement of ^{85}Kr event rate

As described in liquid scintillator purification, ^{85}Kr used to be one of the main overwhelming background and their contamination in liquid scintillator was monitored with a residual gas analyzer (Zhang, 2011:Appendix. A) during the purification. This analyzer measures the amount of natural stable isotopes ^{84}Kr and ^{40}Ar, then interprets the amount by the known ratio of amount of radioactive isotopes to that of stable isotopes in atmosphere, where equal purification efficiency and equal measurement efficiency among stable and radioactive isotopes is assumed. Later, problems of the measurement caused by saturation of the detector of the analyzer is pointed out (Kozlov, 2010), thus the values from the measurement is not applied in this analysis. The analyzer was substantially upgraded so that it has enough sensitivity to measure 10 uBq/m^3 of ^{85}Kr and 0.01 uBq/m^3 of ^{39}Ar (Kozlov, 2011), where ^{36}Ar is used instead of ^{40}Ar for the interpretation.

On Aug. 3 and 10, 2011, 8 litters of liquid scintillator were directly sampled from +1.5 m from the center of the detector and ^{85}Kr and ^{39}Ar contamination was measured with the upgraded residual gas analyzer. The measured valued is listed in Table 6.6 (Kozlov, 2011, 2013).

Table 6.6.: Direct sampling and measurement of noble gasses

Day	^{85}Kr rate [uBq/m^3]	^{39}Ar rate [nBq/m^3]
Aug. 3 2011	9.9	26.0
Aug. 10 2011	6.6	27.5

Although this measurement gives significant information of contamination of noble gasses in the liquid scintillator at a specified position and time, the measured values are not directly applied to ^{7}Be solar neutrino analysis, since there is obvious convection of liquid scintillator inducing position and time dependence of low energy events and thus we cannot assume the uniformity of the contamination. On the other hand, the ratio of ^{39}Ar to ^{85}Kr can be used for the analysis, since there is good consistency among the ratio of the measured values in the purified liquid scintillator (3.24×10^{-3}) and the ratio of the measured values in the atmosphere (10.5×10^{-3}), where the event rate of ^{85}Kr itself has 6 order of difference.

In ^{7}Be solar neutrino analysis, only a constraining parameter is applied.

$$\chi^2_{\text{penalty}} \left(ratio \equiv \frac{^{39}\text{Ar rate}}{^{85}\text{Kr rate}} \right) = \frac{(ratio - 3.24 \times 10^{-3})^2}{(7.26 \times 10^{-3})^2}, \tag{6.9}$$

which gives 0 when ratio is the same as the value of the direct measurement in the liquid scintillator and gives 1 when it is of in the atmosphere.

Delayed Coincidence Analysis of ^{85}Kr.

^{85}Kr decays with β particle emission and there is a very small branch of $\beta + \gamma$ emission which has relatively longer interval.

$$^{85}\text{Kr} \xrightarrow[Q_\beta=0.173 \text{ MeV},\ \ 0.434\ \%]{T_{1/2}=10/756 \text{ y}} \ ^{85}\text{Rb} \xrightarrow[Q_\gamma=0.514 \text{ MeV},\ \ 100\ \%]{T_{1/2}=1.015 \text{ us}} \ ^{85}\text{Rb}$$

Tagging this branch by delayed coincidence method could evaluate the total event rate. One of the measurement difficulties lies in that the prompt energy is too small to be triggered for itself. Thus a DAQ event including both a prompt and a delayed event is studied, and an event-interior signal search method (Xu, 2013a) is constructed. There are 8 events detected in the period for the ^{7}Be solar neutrino analysis in radius ¡ 4.5 m, and the ^{85}Kr event rate is evaluated as 17.3 ± 5.90 uBq/m^3 (Xu, 2013b) with consideration of contribution of background and detection efficiency. The vertex distribution of the detected events is roughly correlated to the higher ^{210}Bi event rate region, however the eccentricity of the mean value are not used for the ^{7}Be solar neutrino analysis due to the small statistics.

6.3. Spallation Products Induced by Cosmic-Ray Muons

6.3.1. Event Rate of Spallation Products

Cosmic-ray muons induce spallation products. The decay of those products can be a background for ^{7}Be solar neutrino analysis, as ^{11}C is obvious in the data energy spectrum in Figure 5.15 Hence, the isotope production yields in KamLAND are evaluated in (Abe et al. and KamLAND Collaboration, 2010). The production rate of those isotopes are summarized in Table 6.7, where the production rates from (Hagner et al., 1999) are listed with re-evaluation with the measured muon flux in KamLAND, and where the production rate for ^{7}Be indicates that for all branches instead of that for 10% branch with emitting γ shown in (Hagner et al., 1999).

In this analysis, the measured production rates are used for ^{12}B, ^{12}N, ^{8}Li, ^{8}B, ^{9}C, ^{8}He, ^{9}Li, ^{11}C, ^{10}C, ^{11}Be, and Hagner's value is used for ^{6}He. Treatment of ^{7}Be is discussed in the next sub-section. In addition, the ^{10}Be rate, estimated to be 50.2 ± 4.9 events/day/kton by MC simulation in (Winslow, 2008) is included.

The combined energy histogram is shown in Figure 6.13. Other than the dominant spallation products around ^{7}Be solar neutrino energy window such as ^{11}C, ^{10}C, ^{7}Be and ^{10}Be, the summed spectrum is used for the spectral fit for the ^{7}Be solar neutrino flux.

Table 6.7.: Summary of isotope rates from muon-initiated spallation in KamLAND

Souce	Half-life	Energy [MeV]	Decay Type	Yield [events/kton/day] Measurements	Hagner et al.
^{12}B	29.1 ms	13.4	(β^-)	54.8 ± 1.5	-
^{12}N	15.9 ms	17.3	(β^+)	2.2 ± 0.5	-
^{8}Li	1.21 s	16.0	$(\beta^- \alpha)$	15.6 ± 3.2	2.4 ± 1.0
^{8}B	1.11 s	18.0	$(\beta^+ \alpha)$	10.7 ± 2.9	4.2 ± 1.3
^{9}C	182.75 ms	16.5	(β^+)	3.8 ± 1.5	2.9 ± 1.2
^{8}He	171.7 ms	10.7	$(\beta^- \gamma n)$	1.0 ± 0.5	1.3 ± 0.4
^{9}Li	252.2 ms	13.6	$(\beta^- \gamma n)$	2.8 ± 0.2	1.3 ± 0.4
^{11}C	29.4 min	1.98	(β^+)	1106 ± 178	537.5 ± 95.5
^{10}C	27.8 s	3.65	$(\beta^+ \gamma)$	21.1 ± 1.8	68.9 ± 16.1
^{11}Be	19.9 s	11.5	(β^-)	1.4 ± 0.3	< 1.4
^{6}He	1.16 s	3.51	(β^-)	-	9.6 ± 2.0
^{7}Be	76.9 day	0.478	$(EC\ \gamma)$	-	136.6 ± 28.6

6.3.2. ^{7}Be (electron capture γ)

^{7}Be is one of spallation products and decays via electron capture with emitting 477.6 keV γ rays in 10.44 % branch. The visible energy spectrum is shown in Figure 6.13 and could be a background for ^{7}Be solar neutrino analyisis when the lower energy threshold is lowered less than around 550 keV. Among spallation products, ^{7}Be has relatively much
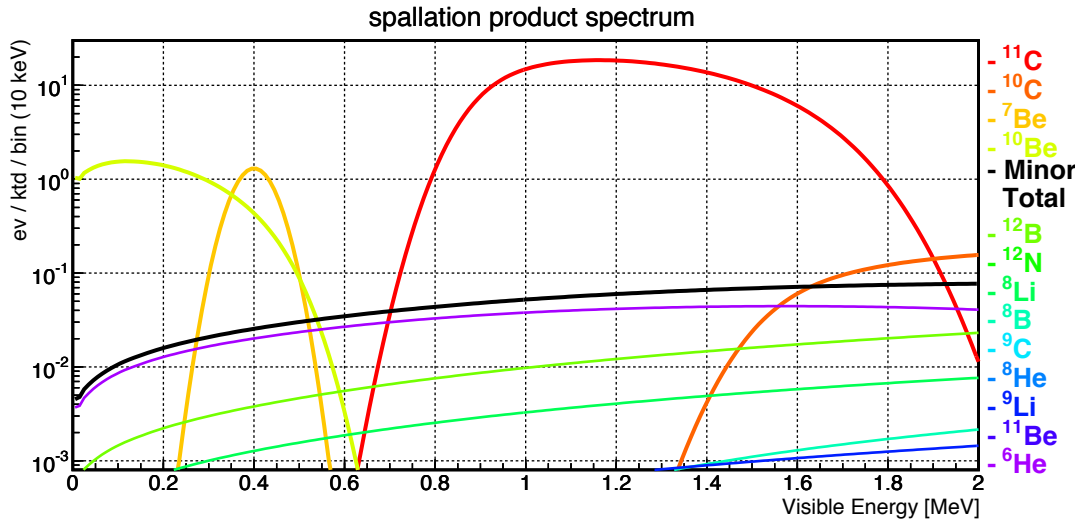
Figure 6.13.: The theoretical visible energy spectrum of spallation products. ^{40}K Total is used in ^{7}Be solar neutrino spectral fit.

longer half life and different considereation is required. As listed in Table 6.7, Hagner estimated the production rate of ^{7}Be at the KamLAND site (2,700 m.w.e.) to be 136.6 ± 28.6 events / day / kton, which corresponds to 14.3 ± 3.0 events / day / kton of gamma emission.

Although the purification of the KamLAND liquid scintillator was performed underground and the distillation effectively removes a metal element Beryllium, newly supplied liquid scintillator component might have been exposed curtain period at ground level, and thus ^{7}Be decay rate could be much higher than the estimated production rate.

With noticing the difference among event rates of Hagner's estimation and that of evaluation in KamLAND, and noticing the possible difference of decay rate due to newer components, we do not use the Hagner's value in this analysis.

Since ^{7}Be energy spectrum is located at the tail region of ^{210}Po and where the pileup events are unignorable, it is simultaneously fit with ^{7}Be solar neutrino as a thoroughly floated parameter.

6.4. PileUp events

The event window length of a KamFEE channel is 200 ns, and the event window of KamFEE DAQ is approximately 500 ns. The enhancement of the window is enabled by the NsumMax based trigger with 275 ns window in order to insure acquisition of an entire physics event which could take place in various position in the detector and thus have variousa time distribution. On the other hand, wider event window could contain multiple physics events from different sources. Such coincidence in one event window is called *Pileup*, and the resulting event is called *Pileup event*. For instance, a physics event take place at 1 kHz coincides and generates a pileup event by event rate of 0.3 Hz.

When a pileup event is generated by independent physics events with larger time and/or position difference, timing distribution of acquired pulses in PMTs is quite different from those of a single physics event or a group of physics events in a cascade decay in a few nanoseconds. A typical single source event and a multiple sources events are shown in Figure 6.14. Hereafter, the latter case is discussed.

Such a pileup event confuses vertex or energy reconstruction processes, which try to understand an event as a single source event and try to fit time, hit, charge distribution by PDF of a single source event. Then a reconstructed event has quite different position and/or energy. For instance, the left and the right events in Figure 6.14 are evaluated to have similar energy ~0.4 MeV, but the number of hits contributing the main signal are twice different. Since the number of hits is relative to energy at such lower energy, the right should have been evaluated to have twice larger energy. This infers that a pileup event could have smaller energy than not only the energy of total events but also the energy of the main signal.
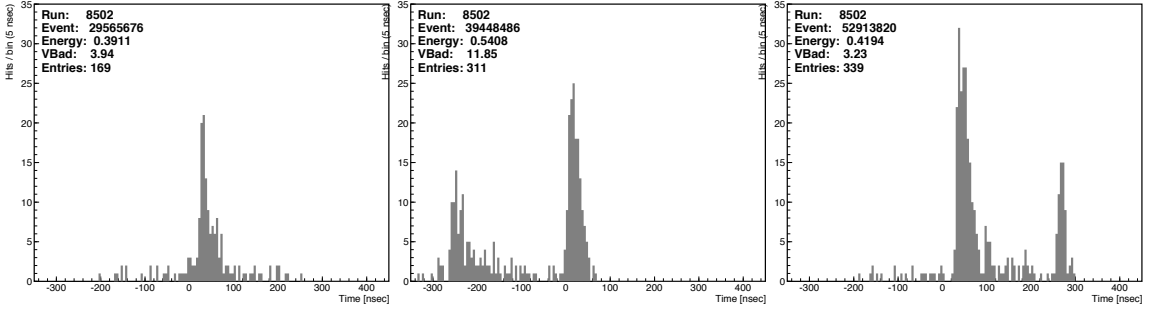
Figure 6.14.: Time Spectrum of Single and Multi-source events. All events shown are worse *Vertexbadness* events. The event on the left is likely a single source event. The events on the middle and the right have main signals at around 50 ns, and other events in front of and behind of them.

Since there are much more worse *VertexBadness* events at ^{7}Be solar neutrino energy region, studying the source signals of pileup events to evaluate the contamination of them in the data is required. For this study, the event-interior *twin-peak* search method (Xu, 2013a) constructed for evaluation of short interval cascade decay of ^{85}Kr, is adopted

and the poorly reconstructed events having worse *VertexBadness* are investigated.

During the analysis period, in the single trigger energy region, corresponding to the visible energy > 0.38 MeV, and in 4.5 m radius, 2392 events out of 30908 poor events are identified as pileup events. The property of the events are shown in Figure 6.15, where the earlier and the later signal are called the prompt and the delayed signal respectively. The original energy distribution just shows increasing event rate toward lower energy. This is related to the ^{210}Po peak located at around 0.3 MeV and to the higher ratio of the poor events around the energy range, described in the previous chapter.
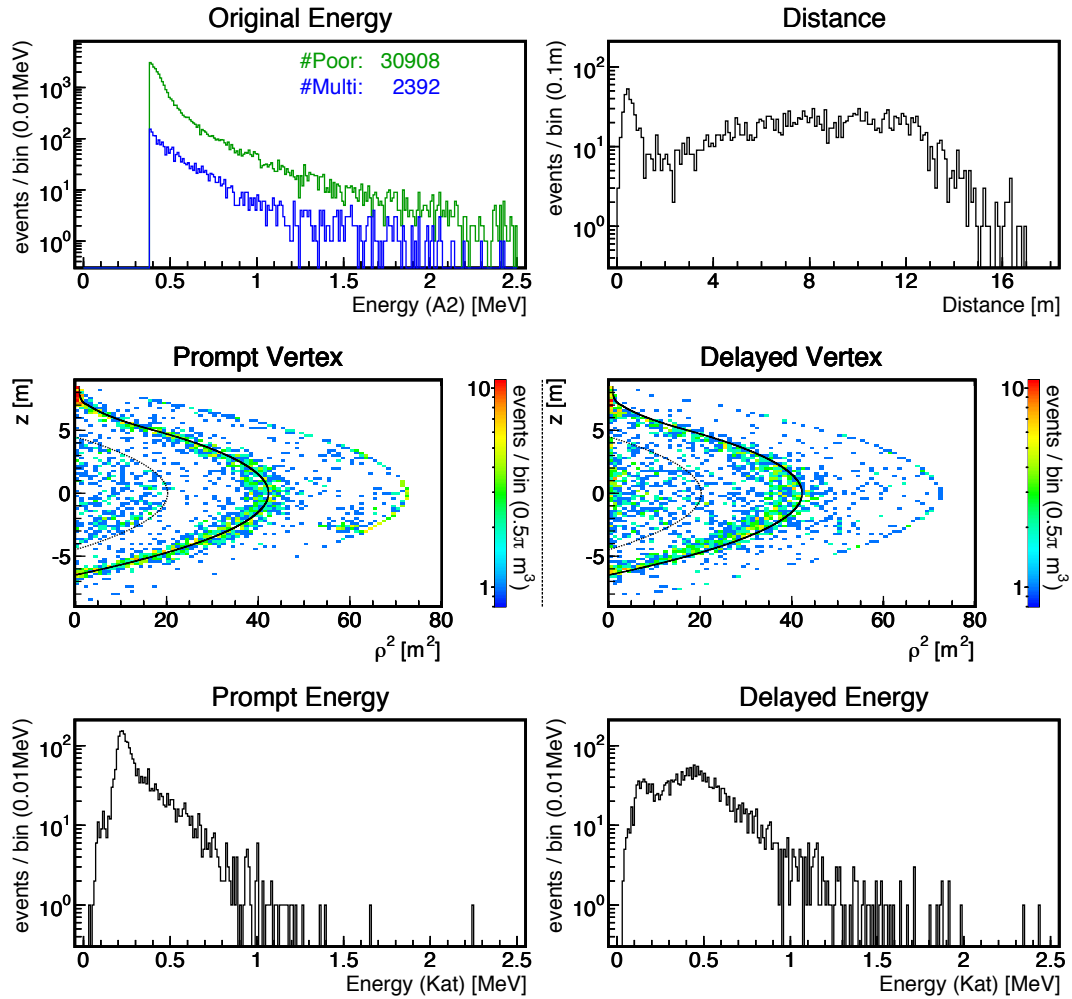
Figure 6.15.: Internal structure of pileup events. The poor events having energy > 0.38 MeV, radius <4.5m are selected.

In the vertex distribution of both of the prompt and delayed signals, the balloon shape

is prominent at radius ~ 6.5 m, marked with black solid line. Among the pileup events, approximately 80 % of the events have at least one internal event at around the balloon. From the prompt and energy distribution, one of the main source of this is estimated ^{210}Po which has approximately 0.25 MeV and 40 Hz of event rate at the balloon region. Notice that this lower energy of ^{210}Po comes from the different energy fitter used only for this study among the analysis in this thesis. The distinctive peak in the distance distribution located at distance < 1.5 m is estimated to be the cascade decay of ^{212}Bi–^{212}Po. The two thirds of approximately 300 ^{212}Bi–^{212}Po events are also located in the balloon.

This important information that even a balloon event could fall into the fiducial volume by coinciding with another event requires more study on the contribution of the accidental coincidence pileup events in the data set for ^{7}Be solar neutrino analysis. For the study, full-volume MC is performed with KLG4sim, a brach of Geant4 tool kit for KamLAND.

The major internal events from the liquid scintillator and the balloon is tuned to reproduce the measured data in KamLAND. The external events from the surface glass of the PMTs, the surrounding steel stainless shell and the surrounding rock are tuned by scaling the measurement values evaluated by a Ge detector and ICP-MASS in 1999 in order that they reproduce ^{232}Th event rate measured in KamLAND while the ratio among the measured values of ^{238}U, ^{232}Th and ^{40}K is fixed. The radioactive event rate generated in KLG4sim is summarized in Table 6.8. Notice that balloon originated events are doubled since only the half of them could enter the liquid scintillator and then are measured and also that ^{14}C is only generated for the accidental pileup with other events by the function of KLG4sim.

The resulting MC spectra is shown with data spectra in Figure 6.16. The left graph shows the comparison of the good MC, bad MC, good data and bad data spectra. The goodness or the badness is determined by *VertexBadness*, described in the previous chapter. In the figure, the bad MC spectrum almost completely reproduces the bad data spectrum above 0.55 MeV. In the right graph, the good MC spectrum is scaled by the ratio of the bad MC spectrum to the bad data spectrum and the difference of the spectra between before and after the scaling is used as the uncertainty of the spectrum. And this spectrum is used in the spectral fit of ^{7}Be solar neutrino analysis.

The contribution of the uncertainty of the scaled spectrum to the mean value of the data spectrum is shown in Figure 6.17. The contribution is increasing at the lower energy due to the insufficient reproducibility of the MC spectrum, while at the higher energy due to the smaller statistics. In order to suppress the uncertainty less than 1 % of each bin of the data spectrum, 0.50 MeV is chosen as the lower energy threshold in energy spectral fit for ^{7}Be solar neutrino analysis.

6.5. External background

The r dependent preliminary fiducial volume selection described in the previous chapter. The selection is chosen so that the event rate of external backgrounds in ^{11}C energy

Table 6.8.: Radioactivity in KLG4sim

source	origin	decay rate [Hz]
^{14}C (pileup-only)	liquid scintillator	3582
^{210}Po	liquid scintillator	1.9
^{210}Bi	liquid scintillator	0.1
^{85}Kr	liquid scintillator	0.01
^{11}C	liquid scintillator	0.01156
^{210}Po	balloon film	80
^{210}Bi	balloon film	200
^{238}U	balloon film	0.26
^{232}Th	balloon film	0.054
^{40}K	balloon film	14
^{238}U	suspension rope	1.3
^{232}Th	suspension rope	2.97
^{40}K	suspension rope	34
^{238}U	PMT surface glass	7.78
^{232}Th	PMT surface glass	6.48
^{40}K	PMT surface glass	2.76
^{238}U	stainless steel shell	20.7
^{232}Th	stainless steel shell	8.14
^{40}K	stainless steel shell	2.48
^{208}Tl	surrounding rocks	34
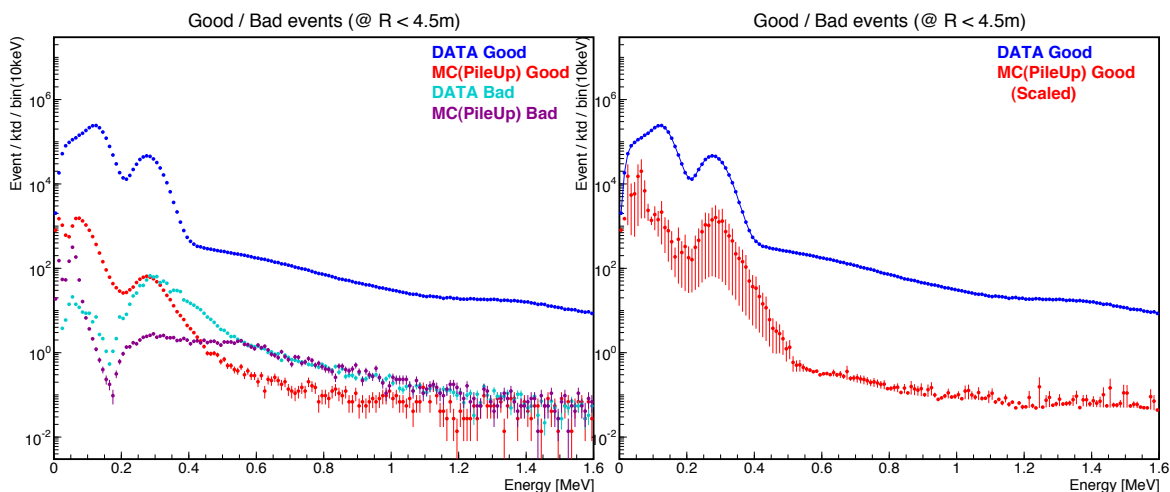
Figure 6.16.: Comparison of MC pileup spectrum and data spectrum.

region is smaller than that of the ^{11}C and the choice is based on the assumption that the external background distribution follows an exponential function of radius. The
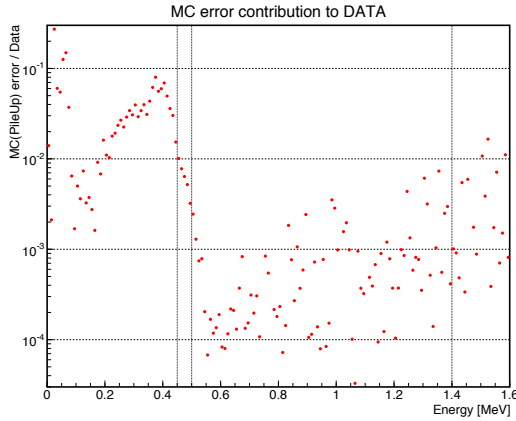
Figure 6.17.: Internal structure of pileup events. The poor events having energy > 0.38
MeV, radius <4.5m are selected.

precise estimation of the residual external background in the fiducial volume could only be proved with a detector MC. The external backgrounds originated from the balloon film, the balloon suspension rope, the surface glass of the PMTs, the stainless steel shell and the surrounding rocks in Table 6.8 are used.

The radius distribution of the generated MC and that of the data are compared in each of 10 keV bin. Figure 6.18 shows the distributions. The difference is presumably coming from the light attenuation length. The radius distribution of MC is scaled by

$$MC - Scaled(E, R) = Amplitude - Factor(E) \cdot MC(R \cdot Radius - Factor(E))$$

in order that the scaled distribution meets the data distribution.

Once the scale factors of each energy bin is evaluated, the radius of all MC events are scaled by the Radius-Factor of the energy of the event. Each of the MC events is then classified by the modified vertex of the event and rank dependent energy distributions are regenerated. The uncertainty of the regenerated spectrum is defined as the difference with the data energy distribution assuming the same exponential distribution of radius in R < 4.5 m volume. The rank dependent energy spectra of MC external events are shown in Figure 6.19.
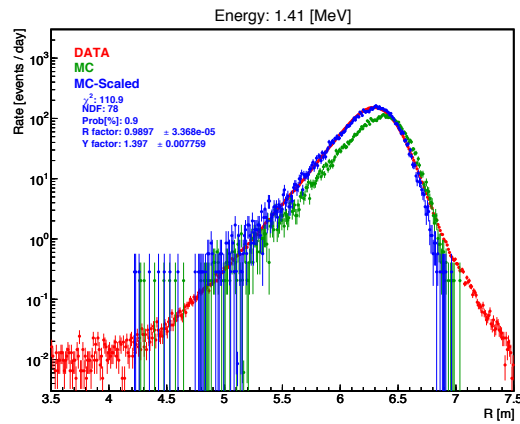
Figure 6.18.: Comparison of the radius distribution of MC and data. The radius distribution of MC (green) is shifted outside of data (red). Scaled MC (blue) is fit to data to evaluate R scale factor.
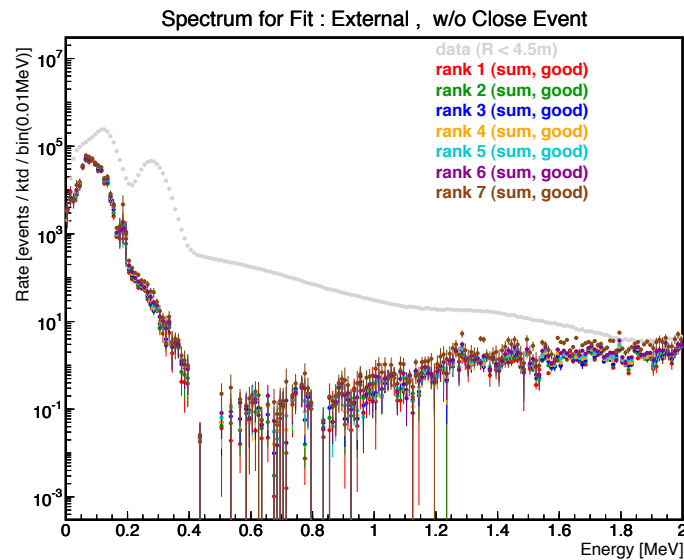
Figure 6.19.: Rank dependent MC energy spectra. The spectra is scaled so that the radius distribution of each energy bin reproduces that of data. The uncertainty of the spectra is defined as the difference between data and MC.

7. ^{7}Be Solar Neutrino Analysis

7.1. Spectral Fit

7.1.1. Fit Condition

Data Set Summary

The essence of the data set is summarized here from the previous chapters.

- Data Period : Apr. 7, 2009 – Jun. 21, 2011

- Data Quality : the good run and the half bad run

- Live Time : 615.9 days

- Fiducial Volume : background-level based rank volumes inside radius < 4.5 m

  : (344.3 m^3 in total)

- Exposure : 165.4 kton-days

- Fit Energy : 0.5 – 1.4 MeV

Fit Method

In the spectral fit the method of least-squared is adopted, where χ^2 to be minimized is defined as follows;

$$\chi^2 = \sum_{j}^{dataset} \sum_{i}^{energy} \frac{\mu_{ij} - th_{ij}}{\sigma_{ij}} + \chi^2_{penalty}, \tag{7.1}$$

where μ_i represents the data event rate, σ_i the statistical uncertainty of the data event rate, th_i total event rate of the theoretical backgrounds and the solar neutrinos in the i-th energy bin respectively, and $\chi^2_{\mathrm{penalty}}$ the total of the additional χ^2 given from the constraint parameters.

Volume Correction Factor

As described in Chapter 5, the uncertainties of the volume bias of the ranked fiducial volumes is calibrated in this fit simultaneously, by some of the backgrounds.

The backgrounds and the solar neutrinos are classified into two categories;

- uniformly distributed events $\Rightarrow$ common parameter among rank fiducial volumes

  $\Rightarrow\Rightarrow$ neutrinos and spallation products

- non-uniformly distributed events $\Rightarrow$ dependent parameter to rank fiducial volumes

  $\Rightarrow\Rightarrow$ other backgrounds

In order to simplify the situation, following parameters are used in the following explanation; event count data sets $DV_j(e_i)$, the uncertainty of them $DE_j(e_i)$, the observed exposure of EX_j, a normalized theoretical *common* background rate $TB(e_i)$ and the scaled factor of the background α, where j denotes a data set index and e_i denotes the energy of i-th bin.

In this case, χ^2 to be minimized is expressed as

$$\chi^2 = \sum_j \left[\frac{\frac{DV_j(e_i)}{EX_j} - \alpha\, TB(e_i)}{\frac{DE_j(e_i)}{EX_j}} \right]^2 , \tag{7.2}$$

where α is the same among different data sets since it should be identical against the rate $DV_j(e_i)/EX_j$ of data.

When there is a bias on the observed exposure, Equation 7.2 is written as,

$$\chi^2 = \sum_j \left[\frac{\frac{DV_j(e_i)}{TEX_j} - \alpha\, TB(e_i)}{\frac{DE_j(e_i)}{TEX_j}} \right]^2 \tag{7.3}$$

$$= \sum_j \left[\frac{\frac{DV_j(e_i)}{EX_j}\delta_j - \alpha\, TB(e_i)}{\frac{DE_j(e_i)}{EX_j}\delta_j} \right]^2 , \tag{7.4}$$

where, TEX_j and δ_j are the true exposure and the bias of it $(EX_j \equiv \delta_j\, TEX_j)$. Since there is a constraint that $\sum_j TEX_j = \sum_j EX_j$, the are totally the number of data set of free parameter exist and δ_j is calibrated so that

$$\delta_j \to \alpha\, TB(e_i)\frac{EX_j}{DV_j(e_i)}. \tag{7.5}$$

The correction factor of observed exposure, δ_j is substantially a correction factor of the measured volume since the uncertainty of livetime is negligible. Thus it is called Volume Correction Factor (VCF).

Fit parameters

Fit parameters are summarized in Table 7.1. Further information of the parameters are given later. In the description, solar neutrinos are just denoted as ν.

Table 7.1.: Fit Parameter Summary

Parameter	Condition	Dependency	Related Parameter
Spectrum Coefficient			
^{11}C	constraint	common	Energy Scale
^{210}Bi	floated	dependent	Energy Scale, Shape Mod.
^{85}Kr	floated	dependent	Energy Scale
$^{7}Be\nu$	scanned	common	Energy Scale
^{238}U–^{234}U (internal)	floated	common	
^{226}Ra–^{210}Pb (internal)	constraint	dependent	
^{232}Th (internal)	constraint	dependent	
^{40}K (internal)	floated	dependent	
^{7}Be	floated	common	
^{39}Ar	constraint	dependent	^{85}Kr
^{210}Po	fixed	dependent	
^{14}C	fixed	common	
External Background	constraint	dependent	
Pileup Event	constraint	dependent	
Other Solar ν	fixed	common	
Other Spallation	fixed	common	
Function Variable			
Energy Scale Nonlinearity	constraint	common	
^{210}Bi Shape Mod.	floated	common	
Volume Correction Factor	constraint	dependent	

Further information on Function Variable parameters are given as follows,

- Energy Scale Nonlinearity: Energy scale nonlinearity effect is parameterized into 4 parameters; Birks constant, Cherenkov contribution, scintillation contribution and dark hit energy. The parameters are floated in the fit and constrained by the value of the best fit to calibration sources and other spallation spectra. Since the minimizer, MINUIT does not tend to scan the whole parameter space, the parameter space is gridded and each point is scanned in the fit. The 4 dimensional parameter space of the energy scale nonlinearity effect is abbreviated afterwards as 4dim-ES. These parameters are related to the most dominant spectra, ^{11}C, ^{210}Bi, ^{85}Kr and ^{7}Be solar neutrinos.

- ^{210}Bi Shape Mod. : Experimental difference of the correction function of forbidden β decay of ^{210}Bi is parameterized into 4 ^{210}Bi shape modulation parameters.

The parameters are freely varied in the fit. These parameters are related to the spectrum, ^{210}Bi only.

- Volume Correction Factor : Event selection bias due to making time-volume slices and integrating them into rank FVs, is parametrized into Volume Correction Factor of each rank FVs. The parameters are freely varied in the fit. The parameters are related to the all spectra

Further information on Spectrum Coefficient parameters are given as follows,

- ^{11}C : Event rate is floated in the fit and constrained at 1106 ± 178 event/kton/day. The shape of the spectrum is varied as function of the 4dim-ES.

- ^{210}Bi : Event rate is freely varied in the fit. The spectrum shape is varied according to the 4dim-ES. The spectrum shape is also modified with the 4 dimensional ^{210}Bi Shape Mod. parameters.

- ^{85}Kr : Event rate is freely varied in the fit. The spectrum shape is varied according to the 4dim-ES.

- ^{7}Beν : Event rate is scanned at 40 points between $\sim$250 and $\sim$800 event/kton/day, in order to evaluate the uncertainty of the event rate of ^{7}Be solar neutrino precisely. The spectrum shape is varied according to the 4dim-ES.
  SFII-SSM provides two independent information of the solar interior based on AGSS09 and GS98 abundances. Hence the survival probability of electron neutrinos in the SSM information differs as well as total flux of the neutrinos. The difference of the probability results in the difference of theoretical visible energy spectra of ^{7}Be solar neutrinos. The spectral fit is done based on the two spectra, SFII-AGSS09 and SFII-GS98 spectra.

- ^{238}U–^{234}U : Event rate is freely varied in the fit considering the secular equilibrium with ^{214}Bi–^{214}Po is broken. Although there also could be non-uniform distribution of ^{238}U–^{234}U, since the expected contribution of this background source is too small, it is treated as an uniformly distributed parameter in the fit. Systematic uncertainty is only discussed when the observed contribution is negligible.

- ^{226}Ra–^{210}Pb : Event rate is fixed at the best fit value evaluated from delayed coincidence analysis. Systematic uncertainty due to fixing the event rate is evaluated afterward by shifting the event rate by $\pm\sigma$ of the best fit value.

- ^{232}Th–^{208}Pb : Event rate is fixed at the best fit value evaluated from delayed coincidence analysis. Systematic uncertainty due to fixing the event rate is evaluated afterward by shifting the event rate by $\pm\sigma$ of the best fit value.

- ^{40}K : Event rate is freely varied in the fit.

- ^{7}Be : Event rate is freely varied in the fit considering the newer liquid scintillator components have larger ^{7}Be than that generated underground. Although there

also could be non-uniform distribution of ^{7}Be, since the expected contribution of this background source is too small in the fit range, it is treated as an uniformly distributed parameter in the fit. Systematic uncertainty is only discussed when the observed contribution is negligible.

- ^{39}Ar : Event rate is floated in the fit but is constrained by the fraction of it to ^{85}Kr event rate.

- ^{210}Po : Since the contribution in the fit range is too small, the event rate is fixed to the value independently determined from a fit in lower energy region.

- ^{14}C : Since the contribution in the fit range is too small and the event rate is not well understood due to insufficient trigger efficiency, the event rate is fixed to 3Bq/m^3.

- External Background : Event rate is floated in the fit but is constrained by the difference between MC and data.

- Pileup Event : Event rate is floated in the fit but is constrained by the difference between MC and data.

- Other Solar ν : Event rate is fixed to the predicted event rate of SFII-SSM. Systematic uncertainty due to fixing the event rate is evaluated afterward by shifting the event rate by $\pm\sigma$ of the predicted event rate.

7.1.2. Best Fit Result

The ^{7}Be solar neutrino event rate and the uncertainty is evaluated from the minimum of parabolic fit to the distribution of the consecutive χ^2 of ^{7}Be solar neutrino spectral fit against the scanned ^{7}Be solar neutrino event rate.

The evaluated ^{7}Be solar neutrino event rate for SFII-AGSS09 is $(582.2 \pm 14.54$ %$)$ event/day/kton with $\chi^2/$ndf $= 635.2/589$. The probability of the fit assuming the χ^2 distribution is 9.3 %.

The event rate for SFII-GS98 is evaluated as $(581.8 \pm 14.7\%)$ event/day/kton with $\chi^2/$ndf $= 635.3/589$. In the following spectra and uncertainty evaluation, only ^{7}Be solar neutrinos based on SFII-AGSS09 are discussed.

The best fit spectra against Rank 1 data at the nearest scanned point giving ^{7}Be solar neutrino event rate 581.1 event/day/kton, are shown in Figure 7.1 and the residual of the fit against the data is shown in Figure 7.2. The best fit spectra against Rank 2 to Rank 7 data are shown in Figure 7.3, 7.4 and 7.5. The residual of the fit for each rank data is shown in Figure 7.6. For each rank, the background subtracted data, that is, (data - background sum) is shown with the ^{7}Be solar neutrino spectrum in the inset graph in the figures. The uncertainty of the background subtracted data is evaluated from the statistical uncertainty of data and the fit uncertainty of background components.

128

Figure 7.1.: Best fit of ^{7}Be solar neutrino spectral fit against Rank 1 data.
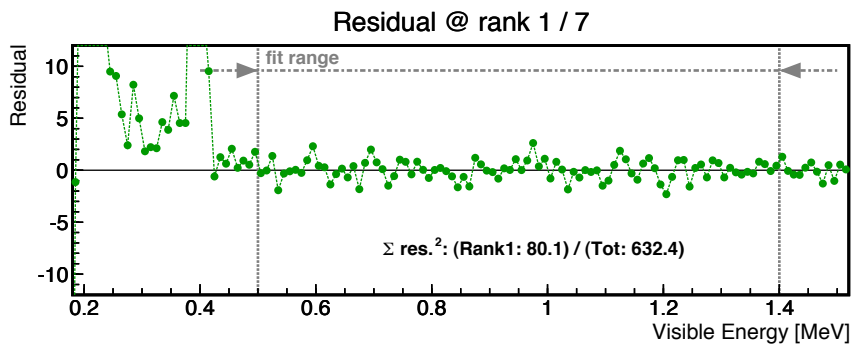
Figure 7.2.: Residual of ^{7}Be solar neutrino spectral fit against Rank 1 data.

Figure 7.3.: Best fit of ^{7}Be solar neutrino spectral fit against Rank 2 and 3 data

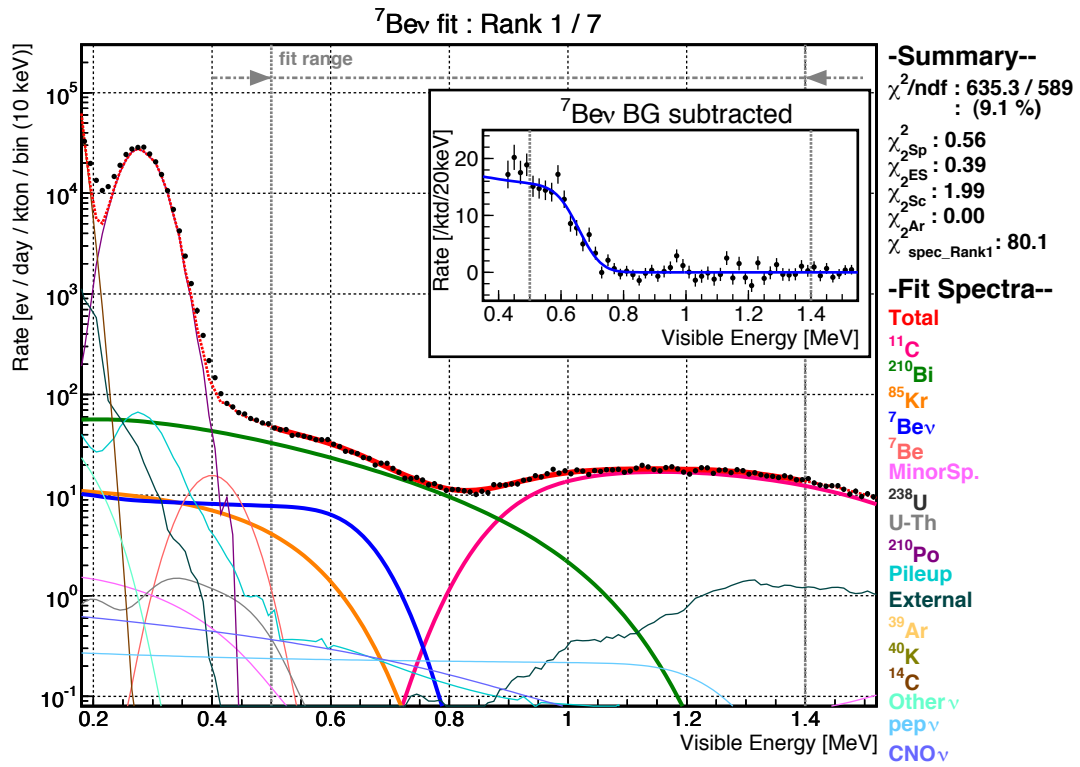Figure 7.4.: Best fit of ^{7}Be solar neutrino spectral fit against Rank 4 and 5 data
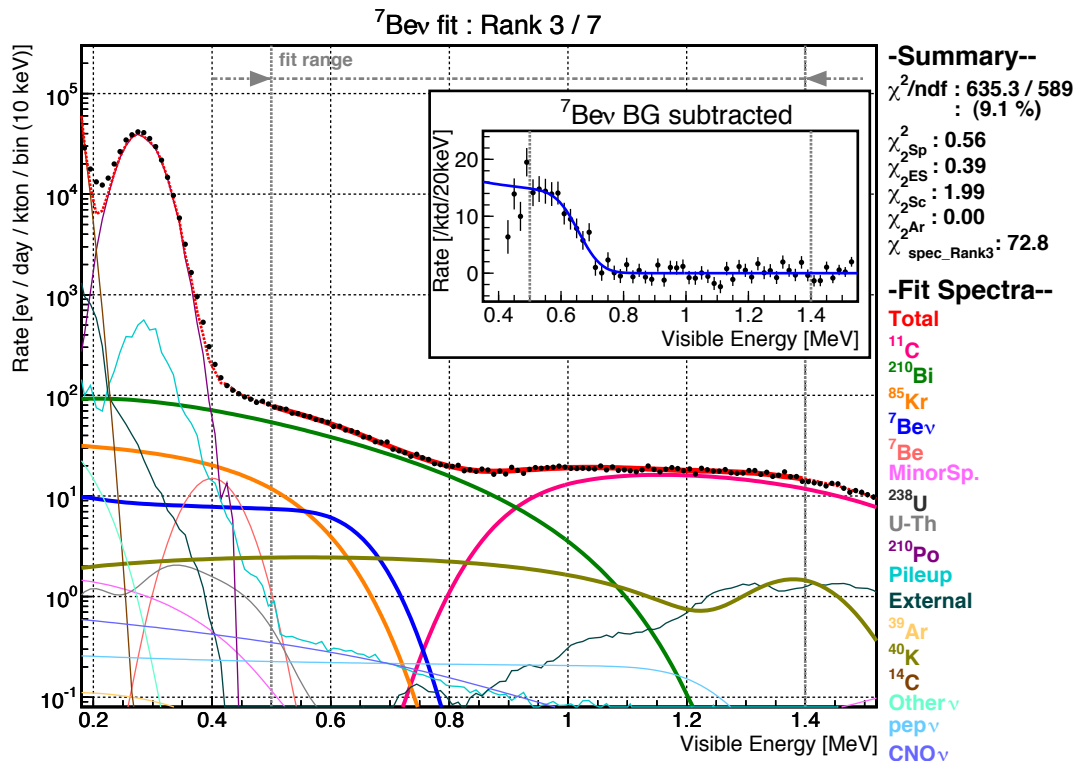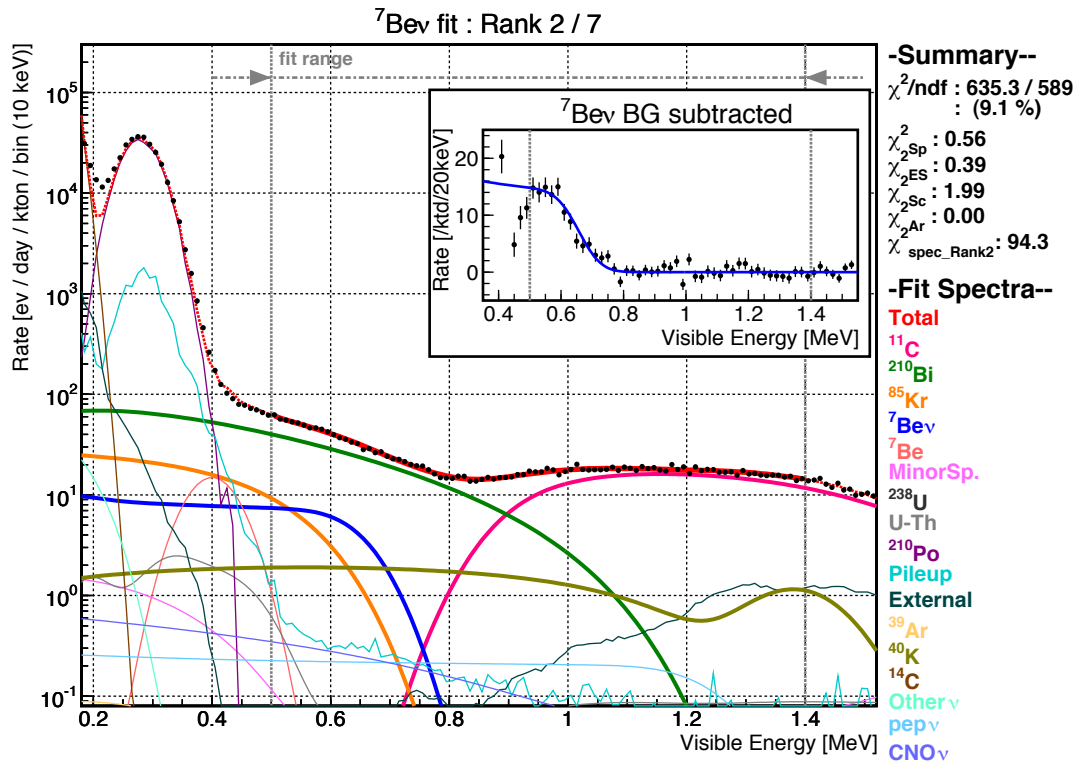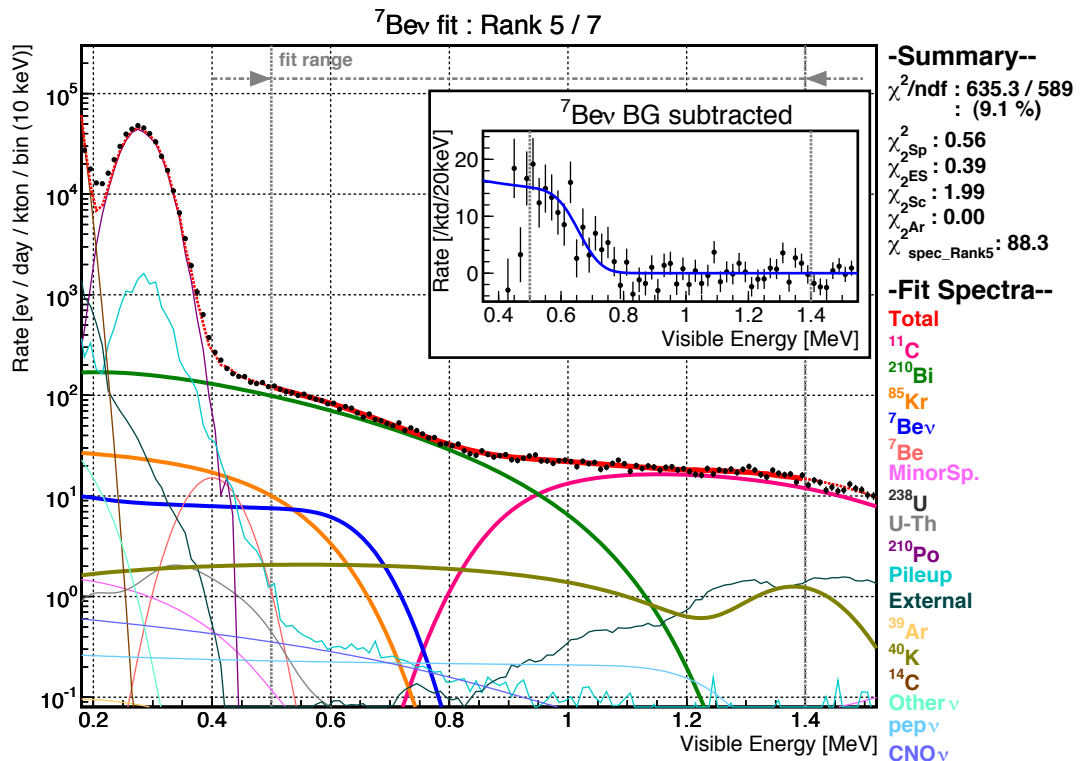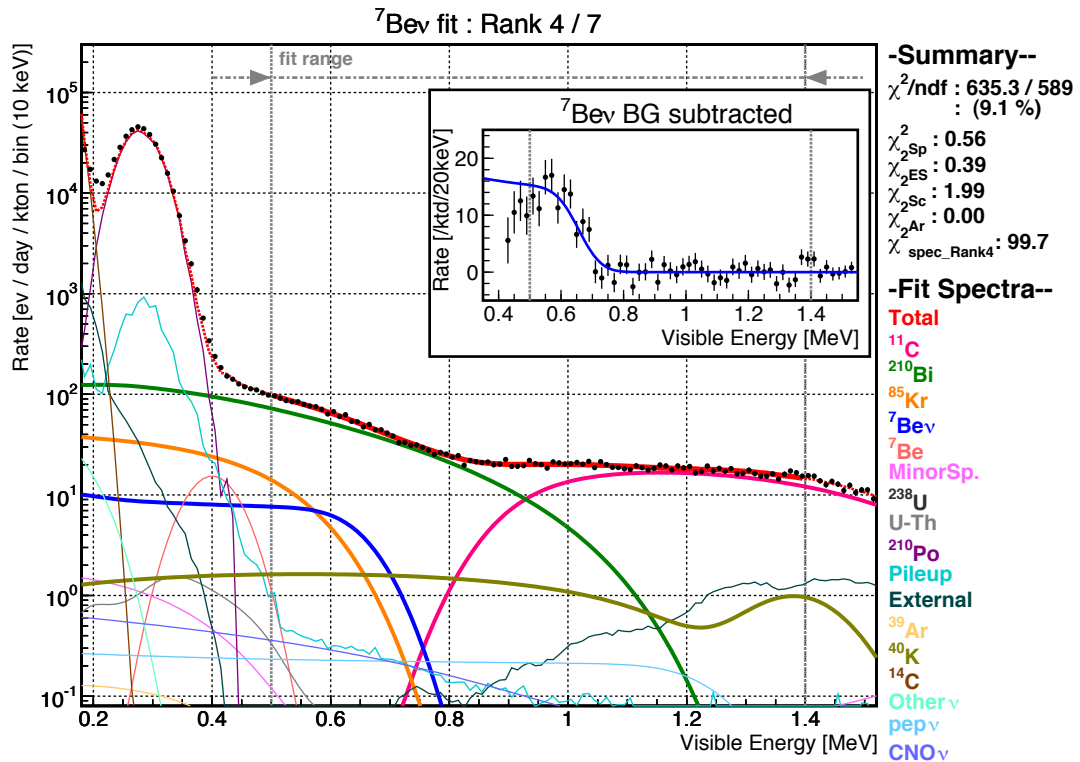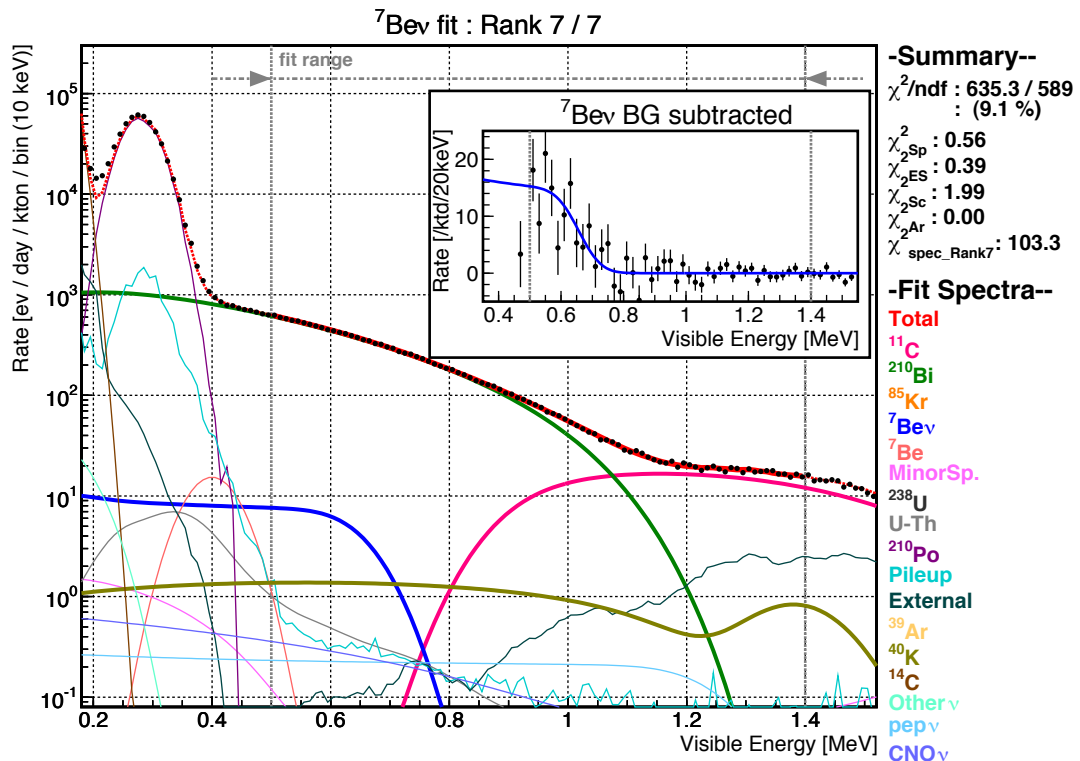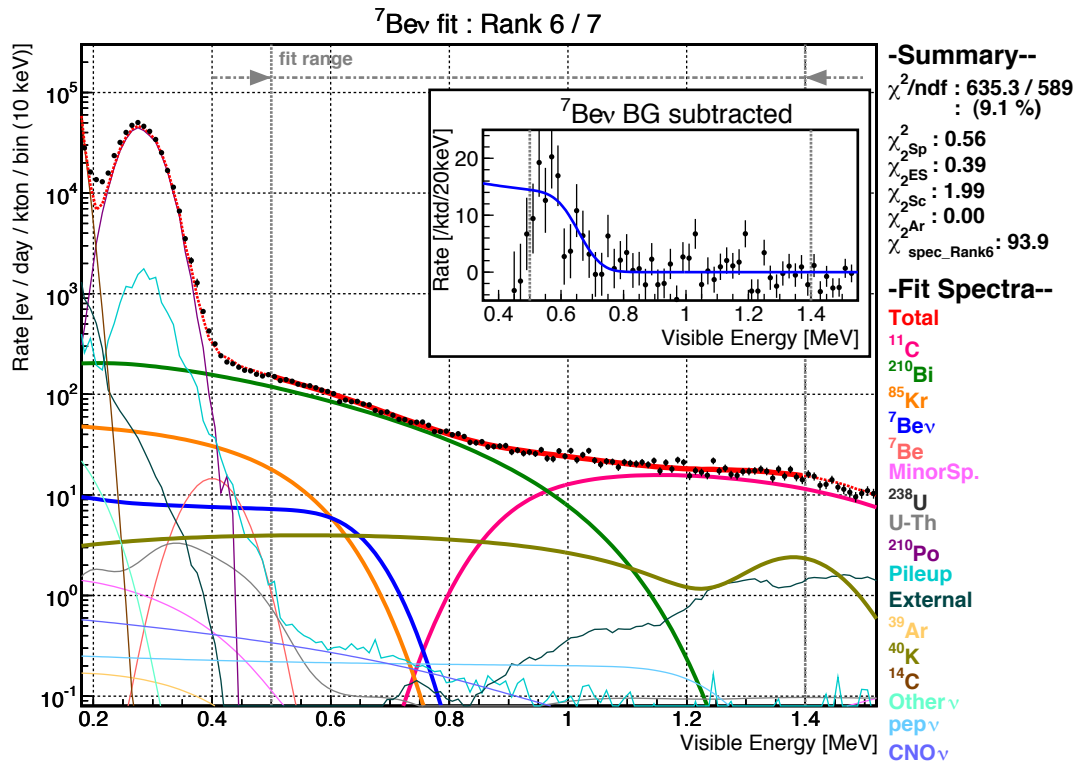
Figure 7.5.: Best fit of ^{7}Be solar neutrino spectral fit against Rank 6 and 7 data
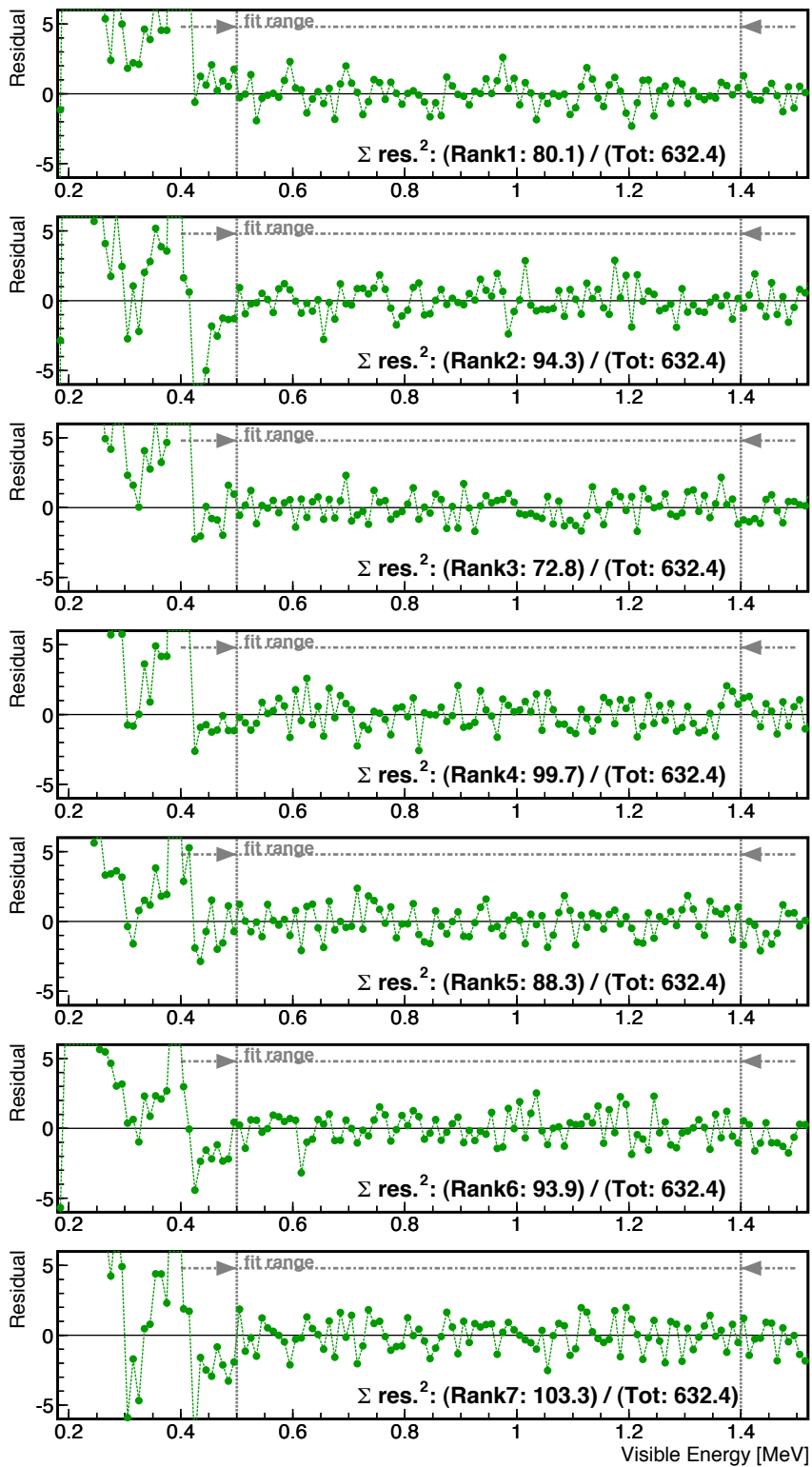
Figure 7.6.: Residual of ^{7}Be solar neutrino spectral fit against each Rank data

7.1.3. Energy Scale Nonlinearity

The four parameters for energy scale nonlinearity are evaluated as in Table 7.2. The uncertainties of the parameters are evaluated too small compared to the uncertainties given from the independent evaluation with calibration data. As already mentioned, ^{7}Be solar neutrino fit is done with scanning the parameter space of them, in order not to be affected by this smaller uncertainties.

Penalty χ^2 is added in the total χ^2 by 0.39.

Table 7.2.: Energy Scale Nonlinearity Parameters

	^{7}Be ν data fit	calibration data fit
Birks Constant [mm/MeV]	0.220 ± 0.00005	$0.26^{+0.10}_{-0.07}$
Cherenkov Contribution	0.045 ± 0.0003	$0.037^{+0.030}_{-0.032}$
Scintillation Contribution	0.935 ± 0.0002	$0.955^{+0.030}_{-0.026}$
Dark Hit Energy [keV]	-1.26 ± 0.34	0^{+9}_{-8}

7.1.4. Volume Correction Factor

The volume correction factors (VCFs) are evaluated for each rank data and shown in Figure 7.7. The biases to be calibrated is at most 4.5 % in Rank 6 and are consistent to the volume uncertainty of 4.5m radius, 3.4 %. This insures that slicing of volume done for generation of the ranked fiducial volume does bring any additional uncertainties.

Absolute difference of exposure between before and after calibration is at most 0.9 ktd in Rank 1.

7.1.5. Background Summary

Background event rate is summarized in Table 7.3. Event rate and its uncertainty and volume correction factor and its uncertainty is considered for each rank and summarized for a rank dependent background such as ^{210}Bi.

Event rate in the fit energy range ($0.5 < E < 1.4$ MeV) is also listed in the table to see the direct contribution for the fit.

7.1.6. ^{210}Bi Spectrum

In ^{7}Be solar neutrino fit, ^{210}Bi spectrum is evaluated for its intensity as well as its shape modulation in KamLAND as expressed in Equation 6.7. The free 4 parameters to modulate the original ^{210}Bi spectrum are evaluated as in Table 7.4.

In order to check the validity of the shape modulation, other 5 fits are performed, in which ^{210}Bi spectra are 4-th polynomial correction factor + no modulation in fit, Daniel's correction + no modulation, Carles' correction + no modulation, 4-th polynomial correction + modulation in fit, Daniel's correction + modulation and Carles' correction +
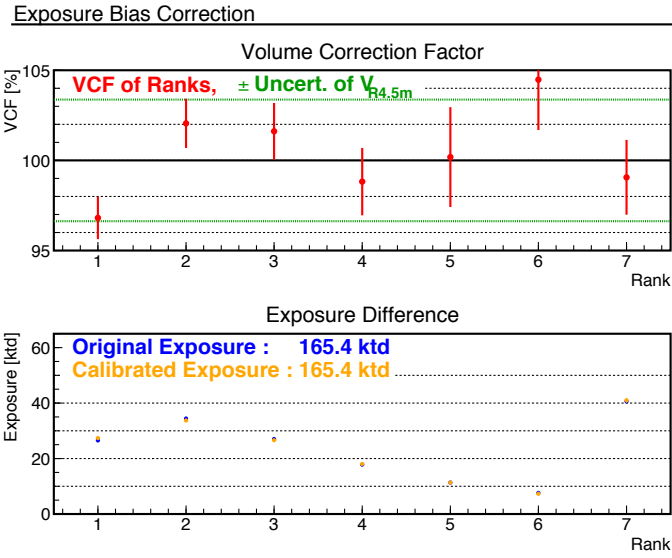
Figure 7.7.: Result of Exposure Bias Correction

Table 7.3.: Background Event Rate Summary

source	rate [ev/ktd]	uncertainty (stat.) [ev/ktd]	rate in fit range [ev/ktd]
^{7}Be ν	582.2	77.4	116.9
^{11}C	972.7	9.6	747.4
^{210}Bi	3153.3	115.4	760.9
^{85}Kr	874.3	59.7	57.8
^{7}Be	166.6	173.2	1.8
^{238}U–^{234}U	0	0	0
^{39}Ar	2.8	2.6	0.04
^{40}K	184.5	28.7	107.0

Table 7.4.: ^{210}Bi shape modulation factors

Coefficient	Fit Value
α	41.4 ± 0.8
β	-101.2 ± 1.4
γ	102.9 ± 3.5
δ	-37.9 ± 2.0

modulation. Best fit spectra for Rank 1 (the most sensitive for ^{7}Be solar neutrinos) and Rank 7 (^{210}Bi is prominently dominant) are shown in the left graph in Figure 7.8.

135

In the right graph in the figure, shape difference is shown as the ratio to Daniel's correction factor + no modulation spectrum. In comparison to Daniel's correction + no modulation spectrum, the other correction + no modulation are different by 2 to 8 % and providing with quite different ^{7}Be solar neutrino event rate. On the other hand all correction + modulation spectra are similar to each other, although they are also different from Daniel's correction + no modulation spectrum at lower energy ($0.5 < E < 0.7$ MeV). This means that shape modulation could absorb the difference of corrections, which is the difference of experiment.
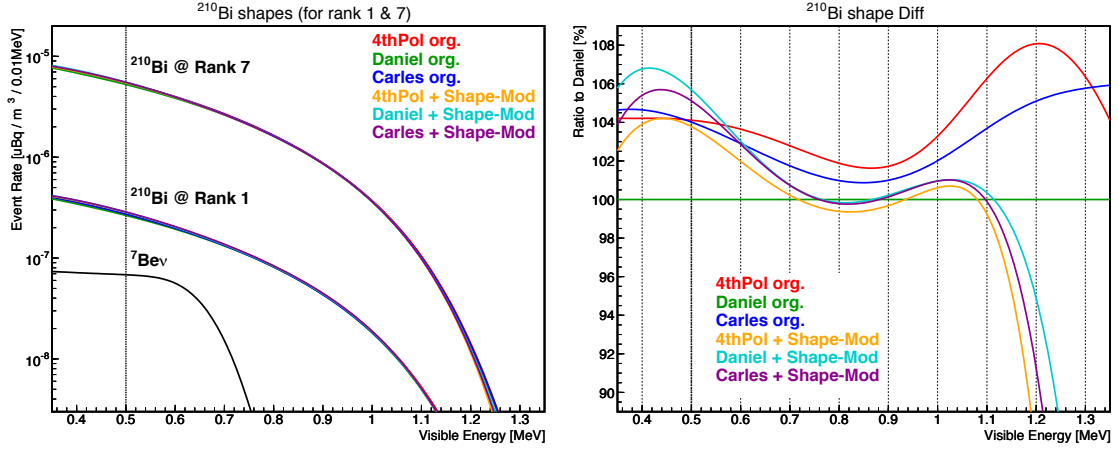
Figure 7.8.: ^{210}Bi Spectrum

7.1.7. Stability of the Fit

Fitting stability is checked against the lower energy threshold of the fit range. The lower energy threshold is varied from 0.40 MeV to 0.60 MeV. Evaluated event rate of ^{7}Be solar neutrinos and the probability, evaluated from χ^2/ndf for each fit are shown in Figure 7.9.

Decrease of probability of at lower energy, i.e. < 0.42 MeV is due to the poor reproducibility of ^{210}Po higher energy tail, while decrease of the event rate at higher energy i.e. > 0.53 MeV is due to difficulty of evaluating ^{7}Be solar neutrino contribution and ^{85}Kr contribution. Between the energy, in $0.42 < E < 0.53$ MeV, ^{7}Be solar neutrino event rate and the fit probability is stable, indicating the stability around 0.5 MeV. Notice that the lower energy threshold is not employed even though the fit result is stable, since the uncertainty of Pileup spectrum gets larger at such energy.
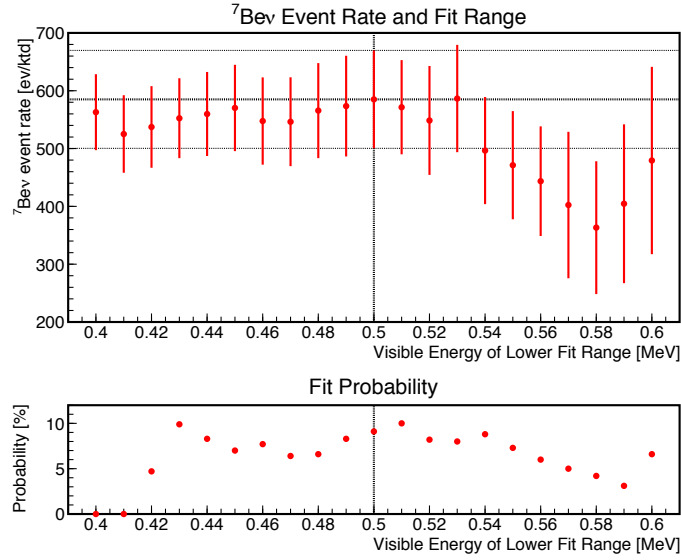
Figure 7.9.: Fit Stability against Fit Range.

7.2. Uncertainties

Systematic Uncertainty of Energy Scale Nonlinearity

The uncertainty of the event rate of ^{7}Be solar neutrinos given in the best fit includes the contribution of the systematic uncertainty of the energy scale parameters. In order to distinguish the statistical and the systematical uncertainty of ^{7}Be solar neutrino event rate the contribution is evaluated.

The uncertainties are related as

$$\sigma^2_{\text{ES-Free}} = \sigma^2_{\text{ES-Fixed}} + \sigma^2_{\text{ES-Syst}}, \tag{7.6}$$

where $\sigma_{\text{ES-Free}}$ is the uncertainty of the event rate of ^{7}Be solar neutrino in the best fit, $\sigma_{\text{ES-Fixed}}$ is that in a fit with fixing the energy scale parameters at the values in the best fit and $\sigma_{\text{ES-Syst.}}$ is the systematical uncertainty due to the uncertainty of energy scale parameters.

In ES-Free case, the event rate of ^{7}Be is already evaluated as (582.2 ± 14.54 %) event/kton/day. In ES-Fixed case, the event rate of ^{7}Be is evaluated as (586.4 ± 13.25 %) event/kton/day. Then σ_{ES} is calculated to be 5.99 %.

Systematic Uncertainty of ^{238}U and ^{232}Th series

The additional uncertainty of the ^{7}Be solar neutrino rate due to fixing the (lower) U series and Th series rates to the center value of the independent delayed coincidence analysis is estimated by changing their rates in ± 1σ. Fit results of ^{7}Be solar neutrino rate are summarized in Table 7.5. Total uncertainties of U/Th series are calculated as

the quadrature-sum of averaged difference of event rate using $\pm 1\sigma$ values for each rank. Then the systematic uncertainty of U series is evaluated as 1.65 % and Th series 1.76 %.

Table 7.5.: Systematic Uncertainty due to U/Th series event rate

	ES best, U-Th best		586.4 ± 13.3 %	
	U mod. (ES best)		Th mod. (ES best)	
		rate [ev / ktd]		rate [ev / ktd]
Rank 1	+1σ	590.0 ± 13.0 %	+1σ	592.8 ± 12.1 %
Rank 2	+1σ	588.0 ± 12.6 %	+1σ	590.4 ± 12.5 %
Rank 3	+1σ	589.0 ± 12.3 %	+1σ	590.5 ± 12.5 %
Rank 4	+1σ	590.5 ± 12.2 %	+1σ	588.5 ± 12.0 %
Rank 5	+1σ	588.3 ± 12.2 %	+1σ	588.9 ± 12.8 %
Rank 6	+1σ	589.6 ± 12.5 %	+1σ	589.8 ± 12.5 %
Rank 7	+1σ	592.8 ± 12.4 %	+1σ	589.7 ± 12.3 %
Rank 1	-1σ	589.3 ± 12.6 %	-1σ	590.3 ± 12.7 %
Rank 2	-1σ	589.7 ± 12.6 %	-1σ	587.3 ± 12.0 %
Rank 3	-1σ	587.0 ± 13.1 %	-1σ	588.7 ± 12.2 %
Rank 4	-1σ	587.6 ± 12.1 %	-1σ	589.3 ± 12.5 %
Rank 5	-1σ	586.1 ± 13.2 %	-1σ	590.5 ± 14.4 %
Rank 6	-1σ	591.1 ± 12.5 %	-1σ	591.2 ± 12.4 %
Rank 7	-1σ	589.4 ± 12.5 %	-1σ	589.9 ± 12.4 %
	U syst. uncertainty	1.65 %	Th syst. uncertainty	1.76 %

Systematic Uncertainty of Solar Neutrino Flux

The uncertainty of the event rate of ^{7}Be solar neutrinos due to fixing the event rate of other solar neutrino fluxes to the center value of the SSM prediction is estimated by the difference of the event rate among using the center value and $\pm 1\sigma$ value. Fit results of event rate of ^{7}Be solar neutrinos are summarized in Table 7.6. Total uncertainties of other solar neutrinos are calculated as the quadrature-sum of averaged difference of event rate using $\pm 1\sigma$ values for each type of other neutrinos. Then the systematic uncertainty of other solar neutrinos is evaluated as 1.87 %.

Summary of Uncertainty

The total uncertainty of ^{7}Be solar neutrinos is summarized in Table 7.7. As described in the previous section, the uncertainty evaluated by the fit is separated to the statistical uncertainty and the systematic uncertainty of energy scale nonlinearity.

Table 7.6.: Systematic Uncertainty due to the other solar neutrino flux

source	ES best, Solar ν best		586.4 ± 13.3 %	
		rate [ev / ktd]		rate [ev / ktd]
pp ν	+0.6 %	588.3 ± 13.1 %	-0.6 %	590.2 ± 12.5 %
pep ν	+1.2 %	589.2 ± 12.8 %	-1.2 %	587.7 ± 12.7 %
Hep ν	+30 %	587.7 ± 12.1 %	-30 %	589.4 ± 12.7 %
^{8}B ν	+14 %	584.9 ± 13.5 %	-14 %	590.6 ± 12.7 %
^{13}N ν	+14 %	592.9 ± 12.2 %	-14 %	591.4 ± 12.2 %
^{15}O ν	+15 %	590.7 ± 12.7 %	-15 %	588.6 ± 12.4 %
^{17}F ν	+16 %	593.0 ± 12.9 %	-16 %	590.0 ± 12.7 %
			Solar ν syst. uncertainty	1.87 %

The total uncertainty is evaluated as 15.3 %, while the statistical uncertainty 13.3 % and the systematic uncertainty 7.3 %. The most dominant uncertainty for the total uncertainty is the statistical uncertainty and that for the systematic uncertainty is the uncertainty of energy scale nonlinearity.

Table 7.7.: Total Uncertainty of the event rate of ^{7}Be solar neutrinos

Source	Uncertainty [%]
Statistics	13.3
Systematic Total	7.3
Cross Selection	1.0
Number of Target	0.10
Flasher Event Cut	< 0.01
Missing Waveform Cut	< 0.01
Event Reconstruction Quality Cut	< 0.01
LiveTime calculation	< 0.01
Radius Fiducial Volume	3.4
Energy Scale Nonlinearity	6.0
U-series	1.7
Th-series	1.8
Other Solar Neutrino	1.9
Total	15.3

7.3. Discussion on Flux of ^{7}Be Solar Neutrinos

7.3.1. Interpretation of the Event Rate to the Flux

The evaluated event rate of ^{7}Be solar neutrinos is (582.2 ± 15.3 %) and (581.8 ± 15.4 %) event/day/kton for SFII-AGSS09 and SFII-GS98, respectively. Assuming the survival probability of electron neutrinos as the best value of global fit, $P_{\nu_e \nu_e} = (0.523 \pm 1.60$ %), the event rate is translated as (5.80 ± 15.3 %) × 10^9 and (5.80 ± 15.4 %) × 10^9 cm^{-2}s^{-1} for each of the SSM, where the intensity difference of spectrum due to the uncertainty of the probability, 1 % is added in quadrature.

The earth moves an elliptical orbit around the sun and neutrino fluxes vary seasonally. Variation of the fluxes during the observation period is evaluated from variation of distance and the average flux is evaluated to be 0.996 times of the flux coming from 1 au distance. Since there is negligible uncertainty on the livetime, the uncertainty is omitted. The seasonal variation of the distance and fluxes is shown in Figure 7.10.
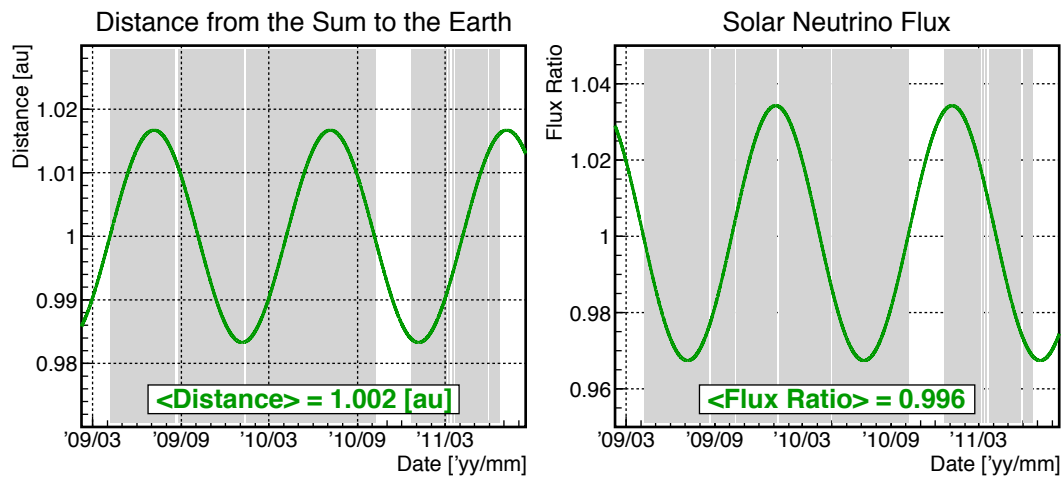
Figure 7.10.: The seasonal variation of the distance between the Sun and the Earth and the solar neutrino flux around analysis period. The gray bands indicate the livetime of the analysis. The weighted average during the livetime of the distance and the flux ratio is 1.002 au and 0.996, respectively.

Under consideration of the variation of fluxes, the flux of ^{7}Be solar neutrinos is evaluated as (5.83 ± 15.3 %) × 10^9 and (5.82 ± 15.4 %) × 10^9 cm^{-2}s^{-1} for SFII-AGSS09 and SFII-GS98 respectively.

7.3.2. Null Hypothesis of ^{7}Be Solar Neutrinos

A hypothesis that contribution of ^{7}Be solar neutrinos is absent is tested by fitting the energy spectra with fixing the event rate of ^{7}Be solar neutrinos zero. The obtained

χ^2/ndf is 702.9/589 and 793.2/589 respectively for SFII-AGSS09 and SFII-GS98. The corresponding $\Delta\chi^2$ is 67.7 and 67.9, hence the hypothesis is rejected by 8.2σ C.L. for both the case. The fit result spectra in Rank 1 with SFII-AGSS09 is show in Figure 7.11.
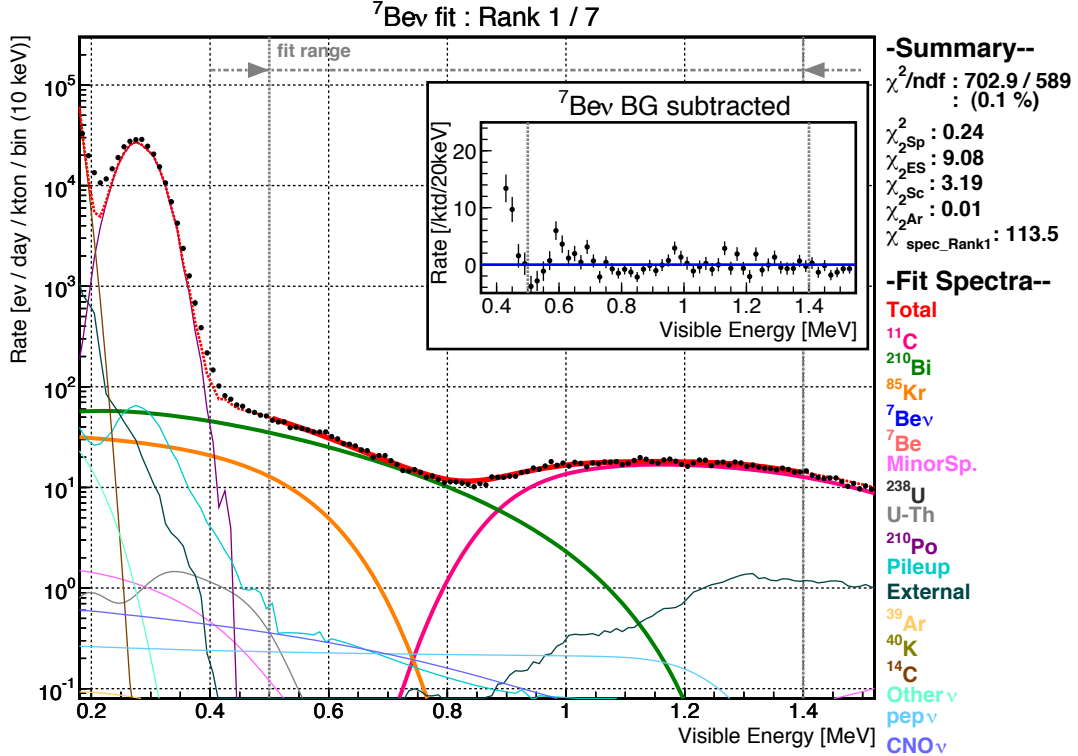
Figure 7.11.: Spectral fit without contribution of ^{7}Be solar neutrinos. Insufficiency of sum of the theoretical spectra is evident at around 0.6 MeV.

7.3.3. Existence of Monochromatic Energy Neutrino

The existence of the signal from ^{7}Be solar neutrinos is examined also in a different way.

In order to insure that the step function spectrum seen in 7.1 is the spectrum of ^{7}Be solar neutrinos, imaginary neutrinos having a monochromatic energy is used in the spectral fit instead of the main branch of ^{7}Be solar neutrino having a monochromatic 862 keV energy. χ^2 is evaluated with various monochromatic energy neutrinos at various event rate of the neutrinos and shown in Figure 7.12. Notice that the event rate includes the contribution of the smaller branch of ^{7}Be solar neutrinos (384 keV) for the consistency to the other fits.

χ^2 is minimized when the neutrino energy is 862 keV and the event rate of the neutrino is 575 event/day/kton. This is the strong evidence that the best fit energy shape is

nothing more than the shape of ⁷Be solar neutrinos.

From the χ^2 distribution of a horizontal row giving the event rate 575 event/day/kton, the energy of ⁷Be solar neutrinos is evaluated as (871 ± 14) keV, which is in good consistent to theoretical 862 keV.
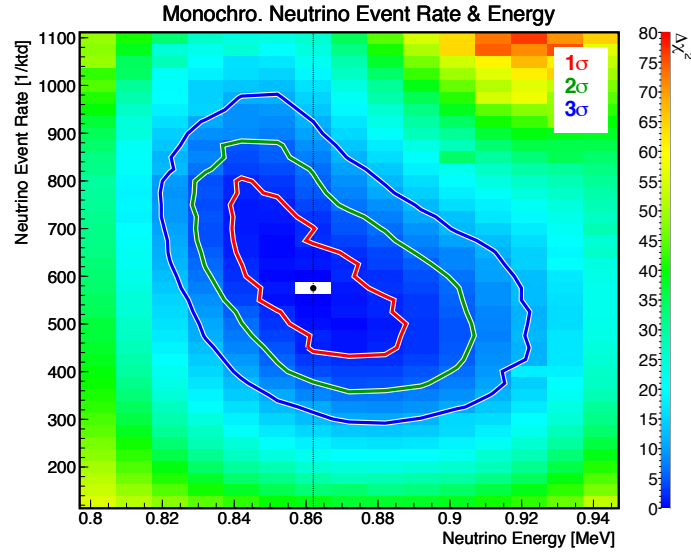
Figure 7.12.: Correlation of event rate and monochromatic energy of imaginary neutrinos.

7.3.4. Survival Probability of 862 keV Electron Neutrinos

While the flux of ⁷Be solar neutrinos is evaluated with the survival probability of electron neutrinos, $P_{\nu_e\nu_e}$ using the best fit oscillation parameters, $P_{\nu_e\nu_e}$ could be evaluated from this measurement by itself. Since only 862 keV branch is evaluated in the fit energy range, $P_{\nu_e\nu_e}$ of the branch is discussed.

As described, the event rate of the ⁷Be solar neutrino is measured to be $(582.2 \pm 15.3 \%)$ and $(581.8 \pm 15.4 \%)$ event/day/kton for SFII-AGSS09 and SFII-GS98, while the expected event rate without neutrino oscillation is $(700 \pm 7.0\%)$ and $(768 \pm 7.0\%)$ event/day/kton respectively.

The lower fit energy threshold, 0.5 MeV in visible energy scale corresponds to 0.505 MeV in electron energy scale. Considering the contribution of a spectrum in the fit energy range, The event rate is converted as $(122.7 \pm 15.3 \%)$ and $(126.6 \pm 15.4 \%)$ event/day/kton for the observed and $(152.0 \pm 7.0 \%)$ and $(166.7 \pm 7.0 \%)$ event/day/kton for the expected. The converted expected value also includes the eccentricity contribution. Hence the event rate ratio of the observed to the expected without oscillation is $(0.807 \pm 16.8 \%)$ and $(0.760 \pm 16.9 \%)$ for SFII-AGSS09 and SFII-GS98 respectively.

The event rate observed is written as

$$R_{\mathrm{obs}} = \Phi_{\nu_{\mathrm{e}}} R_{\mathrm{Branch}} N_{\mathrm{e}} \left[P_{\nu_{\mathrm{e}}\nu_{\mathrm{e}}} \int \sigma_{\nu_{\mathrm{e}}\mathrm{e}} + (1 - P_{\nu_{\mathrm{e}}\nu_{\mathrm{e}}}) \int \sigma_{\nu_{\mu}/\tau\mathrm{e}} \right], \qquad (7.7)$$

while the expected event rate without oscillation is written as

$$R_{\mathrm{exp}} = \Phi_{\nu_{\mathrm{e}}} R_{\mathrm{Branch}} N_{\mathrm{e}} \left[1 \int \sigma_{\nu_{\mathrm{e}}\mathrm{e}} \right], \qquad (7.8)$$

where $\Phi_{\nu_{\mathrm{e}}}$ is the predicted flux of ^{7}Be solar neutrinos, R_{Branch} is the branching ratio of 862 keV neutrinos, 0.8956, N_{e} is the number of target electron in the detector and $\sigma_{\nu_{\mathrm{x}}\mathrm{e}}$ is the differential cross section between neutrinos and electrons. Then the ratio of R_{obs} to R_{exp}, R_{ratio} is written as

$$R_{\mathrm{ratio}} = \left[P_{\nu_{\mathrm{e}}\nu_{\mathrm{e}}} + (1 - P_{\nu_{\mathrm{e}}\nu_{\mathrm{e}}}) \frac{\int \sigma_{\nu_{\mu}/\tau\mathrm{e}}}{\int \sigma_{\nu_{\mathrm{e}}\mathrm{e}}} \right], \qquad (7.9)$$

where $\int \sigma_{\nu_{\mu}/\tau\mathrm{e}} / \int \sigma_{\nu_{\mathrm{e}}\mathrm{e}}$ is evaluated as 0.2294 in the energy range above 0.505 MeV.

Evaluated survival probability of electron neutrino $P_{\nu_{\mathrm{e}}\nu_{\mathrm{e}}}$ is (0.751 ± 21.8 %) and (0.689 ± 21.9 %) for SFII-AGSS09 and SFII-S98 respectively, which disfavor the no oscillation hypothesis by 1.52σ C.L. and 2.07σ C.L. respectively. This probability is much higher than the value given from the global fit to all solar and reactor data, $P_{\nu_{\mathrm{e}}\nu_{\mathrm{e}}} = (0.523 \pm 1.60~\%)$.

7.3.5. Comparison with the SSM prediction and Borexino Result

SFII-SSM prediction of ^{7}Be solar neutrino flux as (4.56 ± 7.0 %) and (5.00 ± 7.0 %) × 10^9 cm^{-2}s^{-1} for AGSS09 and GS98 abundance models respectively. While the Borexino observation reported the flux $(4.75^{+0.26}_{-0.22}) \times 10^9$ cm^{-2}s^{-1}.

Compared with our measurement based on SFII-AGSS09, where ^{7}Be solar neutrino flux is evaluated as (5.83 ± 15.3 %) × 10^9 cm^{-2}s^{-1}, the fluxes of SFII-SSM-AGSS09 and Borexino are inside 1.42σ C.L. and 1.21σ C.L..

Compared with our measurement based on SFII-GS98, where ^{7}Be solar neutrino flux is evaluated as (5.82 ± 15.4 %) × 10^9 cm^{-2}s^{-1}, the fluxes of SFII-SSM-GS98 and Borexino are 0.92σ C.L. and 1.19σ C.L..

Hence our result is consistent to both the SFII-SSM measurement based on AGSS09 and GS98 and the Borexino measurement, and slightly favors the result based on GS98. The mean and the uncertainty of each flux is shown in Figure 7.13.
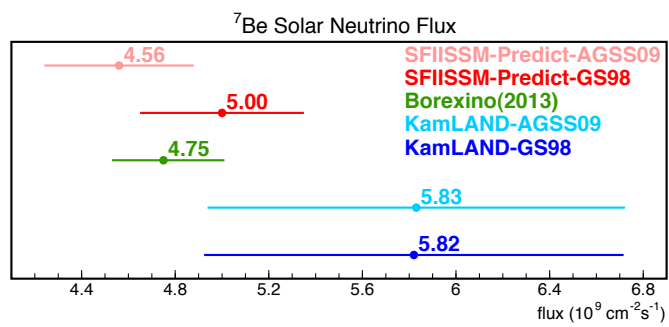
Figure 7.13.: Comparison of ^{7}Be solar neutrino flux among SSM prediction, Borexino observation and KamLAND observation

8. Conclusion

The flux of ^{7}Be solar neutrinos is predicted by Standard Solar Model. Analysis of the solar chemical abundance provides width controversial two models GS98 and AGSS09, which induces significant difference on flux of solar neutrinos generated in interaction of metal element. ^{7}Be solar neutrino is considered to be the best neutrinos for discriminating this issue owing to its relatively larger flux and smaller model uncertainty.

The detector KamLAND consisting already ultimately pure 1000 ton of liquid scintillator, is better at its statistical capability, while the purity is not enough for observation of ^{7}Be solar neutrinos. Hence further purification of liquid scintillator by distillation method was performed from 2007 to 2009 in order to reduce dominant background sources, ^{210}Bi, ^{85}Kr and ^{40}K. The purification reduced significant amount of background and the hint of ^{7}Be solar neutrino spectrum was seen in data spectrum.

Later, unfortunately, thermal destabilization in the detector triggered convection of liquid scintillator and introduced ^{210}Bi near the center of the detector from the far from the center near the balloon, liquid scintillator container. Eventually, the event rate around the energy of ^{7}Be solar neutrinos got temporally and spatially non-uniform and expected signal to background ratio was from a few times to nearly hundred times.

In this work, background treatment in order to properly evaluate better data is focused. The fiducial volume in 4.5 m radius sphere is separated into small slices and classified into 7 ranks by the event rate inside in $0.5 <$ E < 0.8 MeV. Resulting 7 data energy spectra are fitted simultaneously with considering the bias of the separation. The most dominant background ^{210}Bi is evaluated with shape modulation factors for calibrating the difference of experimental correction of the forbidden transition of its β decay.

The results based on 165.4 kton-days exposure during 615.9 days of livetime were presented. An evaluation of the event rate of ^{7}Be solar neutrino in KamLAND yields [582.2 $\pm$ 77.4 (stat.) $\pm$ 42.5 (syst.)] and [581.8 $\pm$ 72.1 (stat.) $\pm$ 53.5 (syst.)] event/day/kton for AGSS09 and GS98 based spectra respectively. The event rate corresponds to a total flux of ^{7}Be solar neutrinos (5.83 ± 0.89) and $(5.82 \pm 0.90) \times 10^9$ cm^{-2}s^{-1} respectively. These fluxes are consistent to those of SSM prediction (4.56 ± 0.32) and (5.00 ± 0.35) $\times 10^9$ cm^{-2}s^{-1} respectively. These fluxes are also consistent to the Borexino evaluation $(4.75 \, ^{+0.26}_{-0.22}) \times 10^9$ cm^{-2}s^{-1}. These results confirmed the SSM prediction and the Borexino measurement.

A. ^{210}Bi spectrum and Fermi Function and Shape Factors

A.1. β decay

When a β decay occurs, an electron and a neutrino are emitted from a nucleus. Precise description of the emitted electron requires consideration on following contributions as well as that of the motion dynamics between the particles;

- The electrical potential shape of the nucleus due to its finite size.
- The screening effect of the nuclear electrostatic field by the orbital electrons.
- The influence of the non-conservation of the spin or the parity of the nucleus.

Hence construction of the energy spectrum for a β decay involves representation of above 4 effects. For the later use, energy and momentum parameters are introduced first.

- W : total energy in $m_{\mathrm{e}}c^2$
- W_0 : maximum value of total energy in $m_{\mathrm{e}}c^2$
- p : momentum in $m_{\mathrm{e}}c$

The above parameters are for electrons when they are used without subscription, where basic equations are given as

$$W = \sqrt{p^2 + 1} \qquad (= \sqrt{(pc)^2 + 1}) \tag{A.1}$$

$$T = (W - 1)m_{\mathrm{e}}c^2. \tag{A.2}$$

β energy spectrum

The energy (momentum) dependent effect of the motion dynamics is called the *statistical shape* and represented by $S(W)$. The second and the third effect related to the electric field is explained by the *Fermi function* and represented by $F(Z, W)$, where Z is the charge and thus the atomic number of the daughter particle. The influence of the last effect is represented by the *correction factor* or the *shape factor*, $C(W)$.

Then the number of electrons decay in the energy range between W and $W + dW$ is given as

$$N(W)dW = \frac{g_\beta^2}{2\pi^3} S(W)F(Z, W)C(W)dW, \tag{A.3}$$

146

where g_β is the weak coupling constant for β decay.

$S(W)$ is given from the volume in momentum space for two particles (e, ν) with momenta (p_e, p_ν) when the total energy (W_0) is fixed and the energy of the first lies between W and $W + dW$.

$$S(W)dW = \int \delta(W_0 - W - p_\nu)p^2 dp p_\nu^2 dp_\nu \tag{A.4}$$

$$= pW dW(W_0 - W)^2 \tag{A.5}$$

$$S(W) = \sqrt{W^2 - 1}W(W_0 - W)^2 \tag{A.6}$$

where $WdW = pdp$ and $p = \sqrt{W^2 - 1}$ derived from (A.1) are used.

While $S(W)$ is given explicitly, $F(Z, W)$ and $C(W)$ are described differently according to the way they are approximated. In the following sections, treatment of them in the KamLAND β spectrum generator *KBeta*, in the experiment by Daniel (Daniel, 1961), and in a comprehensive study by Behrens (Behrens and Jänecke, 1969) are described.

β transition

Before coming into the detail of the implementation of $F(Z, W)$ and $C(W)$, the classification of β transition related to $C(W)$ should be introduced. The non-conservation of the spin or the parity of the nucleus in a β decay makes the decay go through different transition, which is classified by the variation of the spin and the parity as in Table A.1. An allowed transition can be formed with that the total orbital momentum of emitted

Table A.1.: β Transition Classification

Transition	Spin Change $(\Delta J = \|J_f - J_i\|)$	Parity Change $(P_i \cdot P_f)$
Allowed	0, 1	+1
1st non-unique forbidden	0, 1	−1
(n-1)-th unique forbidden	> 1	$(-1)^{n-1}$
n-th non-unique forbidden	> 1	$(-1)^n$

particles equals to zero, while an forbidden transition requires the non-zero total orbital momentum of emitted particles, and is retarded. An *unique* transition is governed by a single *β-moment* then is called unique.

For ^{210}Bi case, the initial and the final nucleus states are ^{210}Bi (J=1, P=-1), ^{210}Po (J=0, P=+1) respectively, which gives (ΔJ=1, $P_i \cdot P_f$=-1), hence the transition is 1st non-unique forbidden transition.

A.2. Fermi Function in KBeta

KamLAND Beta decay generator, KBeta is mainly based on the theoretical formula in Konopinski's texts on the the theory of beta decay (Konopinski and Uhlenbeck, 1941,

Konopinski, 1966, Rose and Konopinski, 1965) and coded by G. Keefer and A. Piepke (Keefer, 2009).

In Konopinski's literatures, the Fermi function is first defined with the nucleus has point charge then is replaced by factor including screening correction. The preliminary, *unscreened* Fermi function is defined as

$$fermi(Z, W) = 2(1 + \gamma_0)(2Rp)^{2(\gamma_0 - 1)} e^{\pi \nu} \frac{|\Gamma(\gamma_0 + i\nu)|^2}{(\Gamma(2\gamma_0 + 1))^2}, \tag{A.7}$$

where each of the new parameters are defined with the fine structure constant α as follows,

$$\gamma_0 = \sqrt{1 - (Z\alpha)^2} \tag{A.8}$$

$$R = \frac{1}{2} A^{\frac{1}{3}} \alpha \tag{A.9}$$

$$\nu = Z\alpha \frac{W}{p}. \tag{A.10}$$

Then the Fermi function is defined by replacing W by $W - V_0$ and multiplying screening correction

$$screen(W) = \sqrt{\frac{p^2}{W^2 - 1} \frac{W - V_0}{W}}, \tag{A.11}$$

as

$$F(Z, W - V_0) = fermi(Z, W - V_0) \cdot screen(W), \tag{A.12}$$

with V_0 as the shift in the potential energy near the nucleus arising from screening using the Fermi-Tomas model,

$$V_0 = 1.13 Z^{\frac{4}{3}} \alpha^2. \tag{A.13}$$

With the replacement, p and ν in *fermi* and *screen* is then redefined as

$$p = \sqrt{(W - V_0)^2 - 1} \quad (= \sqrt{W^2 - 1} \text{ for } W < V_0 + 1) \tag{A.14}$$

$$\nu = Z\alpha \frac{W - V_0}{p}. \tag{A.15}$$

The shape factor $C(W)$ is also defined by a user.

A.3. Fermi Function in Experiments

A.3.1. Daniel

The measurement of ^{210}Bi spectrum by (Daniel, 1961) was performed with using a β spectrometer. With the counted events $N(W)dW$, $C(W)$ is evaluated by

$$C(W) = \frac{N(W)}{S(W)F(Z, W)}, \tag{A.16}$$

which is the modification of (A.3), and the scaling constant is omitted. In the literature, the Fermi function refers to the book (Dzhelepov and Zyrianova, 1956), which is unfortunately inaccessible.

A.3.2. Carles

The measurement of ^{210}Bi spectrum by (Carles and Malonda, 1995, Carles, 2005) using a liquid scintillation detector. $C(W)$ is evaluated as Daniel did, but there is no notation for $F(Z, W)$.

A.4. Fermi Function in LANDOLT-BÖRNSTEIN table

Behrens (Behrens and Jänecke, 1969) numerically evaluated and tabulated $F(Z, W)$ by solving the Dirac equations. The table is called LB hereafter. The unscreened Fermi function there is described as

$$F(Z, W) = F_0 L_0 = \frac{\alpha_{-1}^2 + \alpha_{+1}^2}{2p^2} \tag{A.17}$$

$$F_0 = 4(2pR)^{-2(1-\gamma_1)} \frac{|\Gamma(\gamma_1 + iy)|^2}{\Gamma(2\gamma_1 + 1)^2} e^{\pi y} \tag{A.18}$$

$$L_0 = \frac{\alpha_{-1}^2 + \alpha_{+1}^2}{2p^2 F_0}, \tag{A.19}$$

where

$$\gamma_1 = \sqrt{1 - (\alpha Z)^2} \tag{A.20}$$

$$y = \alpha Z \frac{W}{p}, \tag{A.21}$$

and α_k denotes the so-called Coulomb amplitudes.

The ratio of the screened Fermi function to the unscreened Fermi function, $F_0 L_0^* / F_0 L_0$ is also evaluated and tabulated with following the method in (Bühring, 1965), where the Dirac equations are solved with including the additional potential $V(r)$. The Fermi function and the ratio, $F_0 L_0$ and $F_0 L_0^* / F_0 L_0$ for ^{210}Bi are shown in Figure A.4.

A.5. Comparison of the Fermi function

The Fermi function of KBeta and of LB are compared in Figure A.5. There is approximately 15 % absolute difference among the functions and the 2 % gradient in the ratio in the energy range for ^{7}Be solar neutrino analysis. Among the absolute difference, approximately 6 % comes from the difference in definition of the nuclear radius. KBeta defines it $\sim 1.41 A^{\frac{1}{3}}$ fm, while $LB \sim 1.20 A^{\frac{1}{3}}$ fm. The other 10 % of absolute difference comes from the definition of the Fermi function itself, however the difference can be neglected since the β spectrum is renormalized for a practical use. On the other hand
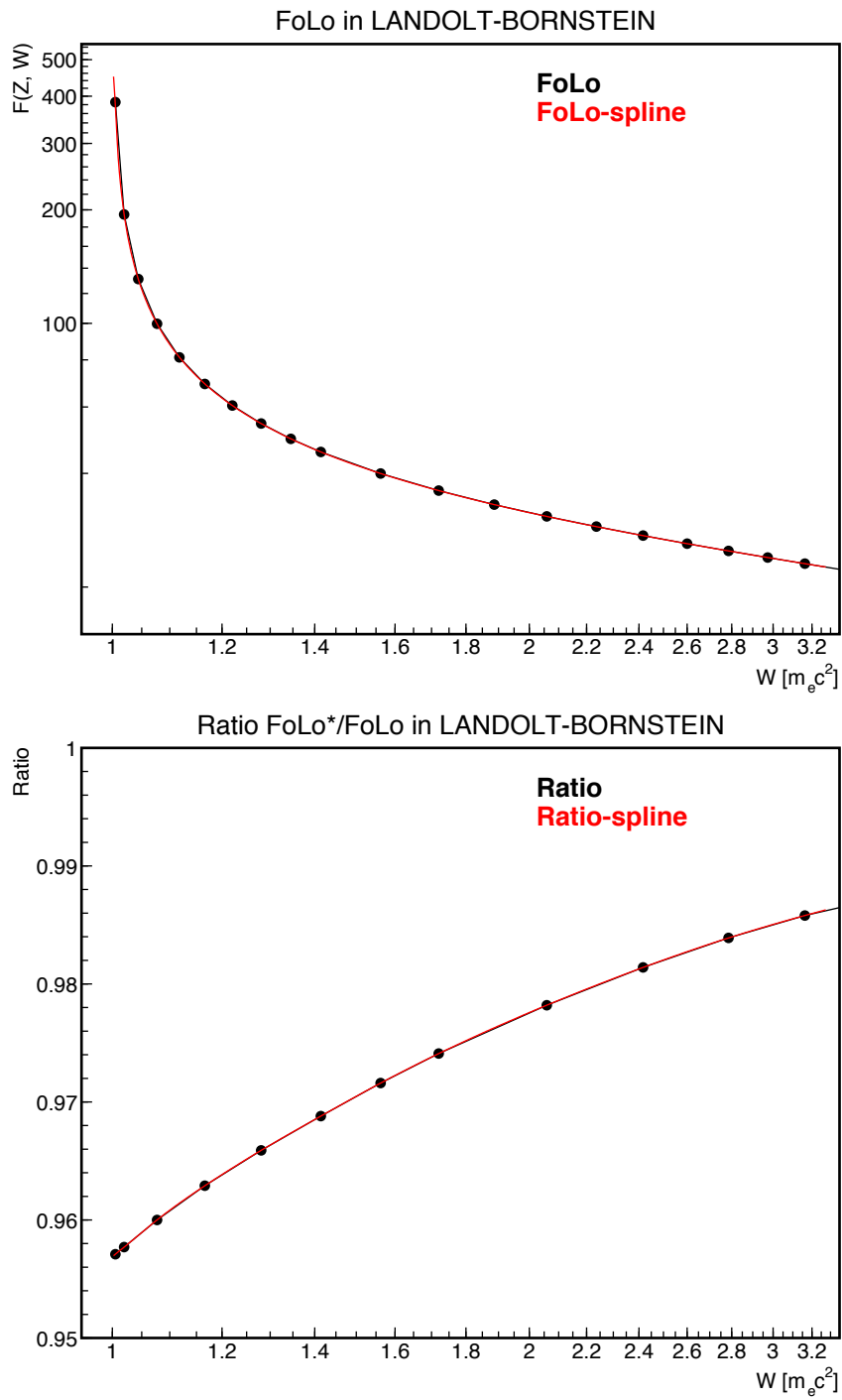
Figure A.1.: The Fermi function and the ratio of the screened to the unscreened for [210]Bi in LANDOLT-BÖRNSTEIN table.
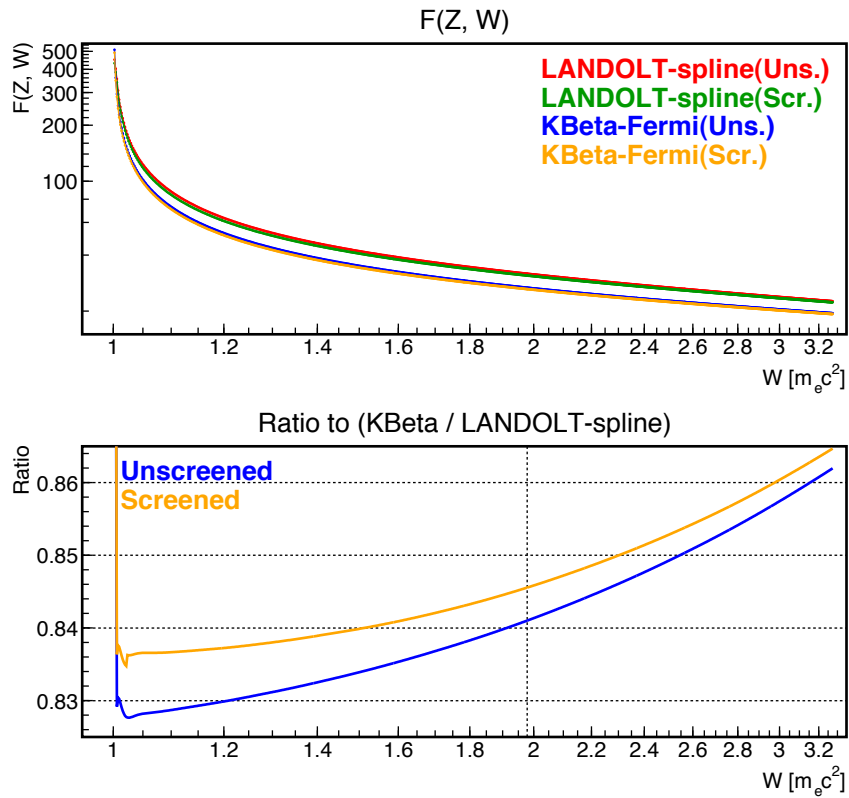
Figure A.2.: The Fermi function for ^{210}Bi in KBeta and in LANDOLT-BÖRNSTEIN and the ratio among them. The dotted line in the bottom graph indicates 0.5 MeV, which is the lower threshold for ^{7}Be solar neutrinos.

the difference in the gradient remains in the β spectrum, hence this important effect is considered later with the contribution of the difference of C(W).

Behrens (Behrens and Jänecke, 1969) gives some information on the Fermi function in (Dzhelepov and Zyrianova, 1956), which is used in the Daniel's experiment;

- (Dzhelepov and Zyrianova, 1956) includes corrections for finite size and for screening, however, the table there is not obtained from an exact solution of the Dirac equations, but is obtained by adding corrections to the Coulomb functions obtained for a point charge nucleus.

- It is pointed out in several literatures that the correction are not quite correct for higher electron momentum.

A.6. Shape Factor

The theoretical shape factor is generally described with following (Behrens and Bühring, 1982) as

$$C(W) = \sum_{k_e e, k_\nu, K} \lambda_{k_e} \left\{ M_K^2(k_e, k_\nu) + m_K^2(k_e, k_\nu) - \frac{2\mu_{k_e}\gamma_{k_e}}{k_e W} M_K(k_e, k_\nu) m_K(k_e, k_\nu) \right\}, \tag{A.22}$$

where k_x denotes the absolute eigenvalue of the angular momentum, M_K and m_k governs the lepton matrix element, λ_{k_e} and μ_{k_e} are the Coulomb functions and $\gamma_{k_e} = \sqrt{k_e{}^2 - (\alpha Z)^2}$

The shape factor for the allowed transition is then formed with a certain normalization,

$$C(W) = \left(1 + aW + \frac{\mu_1 \gamma_1 b}{W} + cW^2 \right), \tag{A.23}$$

where a, b and c are the function of matrix element and a and b are energy independent, while c and μ_1 are energy dependent, and γ_1 introduce before is the Z dependent constant.

On the other hand the shape factor for the 1st non-unique forbidden transition is formed with

$$C(W) = k \left(1 + aW + \frac{\mu_1 \gamma_1 b}{W} + cW^2 \right), \tag{A.24}$$

where k, a, b and c are the function of matrix element and as well as μ_1, are indeed W dependent parameters, however, k, a, b and c are usually treated as energy independent parameters since the variation of the parameters in the mean energy range is small.

Among experiments for the spectrum shape of ^{210}Bi, (Plassmann and Langer, 1954, Daniel, 1961, Frothmann and Wiesner and Löhken and Rebel, 1969) used the explicit formula for the 1st non-unique forbidden transition and re-evaluated by (Behrens and

Szybisz, 1976) as in Table A.6. While (Carles and Malonda, 1995, Carles, 2005) for ^{210}Bi used the approximated formula for the 1st non-unique forbidden transition as recent literatures by other authors for different nucleus, which is wrote down as,

$$C(W) = \left(1 + aW + cW^2\right),$$
(A.25)

and the coefficients are also tabulated in Table A.6. Although the coefficients are mostly

Table A.2.: Coefficient of ^{210}Bi shape factor

a	$\gamma_1 b$	c	author
-0.431 ± 0.011	1.42 ± 0.29	0.0334 ± 0.0068	Plassmann
-0.456 ± 0.050	0.301 ± 0.107	0.0540 ± 0.0027	Daniel
-0.431 ± 0.090	0.084 ± 0.078	0.0488 ± 0.0040	Frothmann
-0.46 ± 0.01		0.0586 ± 0.002	Carles (1995)
-0.47 ± 0.03		0.065 ± 0.009	Carles (2005)

consistent, the shape factors, and thus the ^{210}Bi spectrum is sensitive to the uncertainties of the coefficients. For example, the shape factors of the two experiments are compared in Figure A.6, where the ratio of two factors is shown. The ratio of mean factors itself varies 10 % or so, and the uncertainty of only a gives the ratio at least additional 5 % difference.

^{210}Bi spectra are generated for different experimental shape factors using LB and KBeta and the ratio to that with re-evaluated Daniel's experiment is shown in Figure A.6. The differences of ^{210}Bi spectrum without consideration of the uncertainty of the shape factors result in approximately ± 2 % in the mean energy range above 0.5 MeV. And the difference of Fermi function is smaller than the differences. This requires the ^{7}Be solar neutrino analysis an independent measurement of ^{210}Bi spectrum shape for the detector KamLAND.
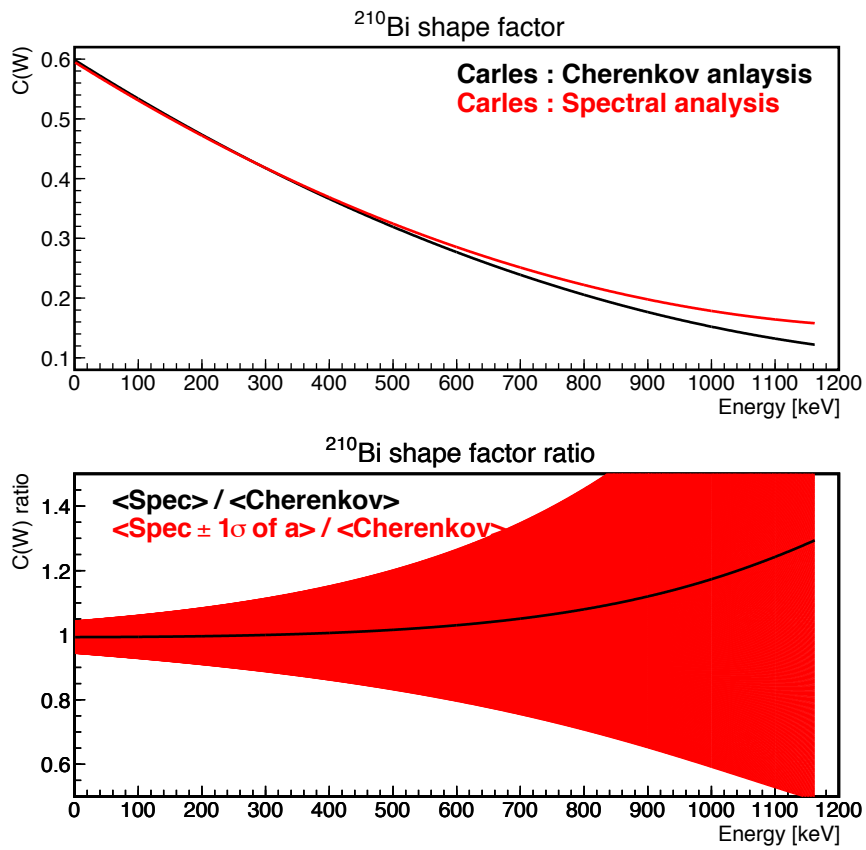
Figure A.3.: Comparison of ^{210}Bi shape factors of Carles's two experiments
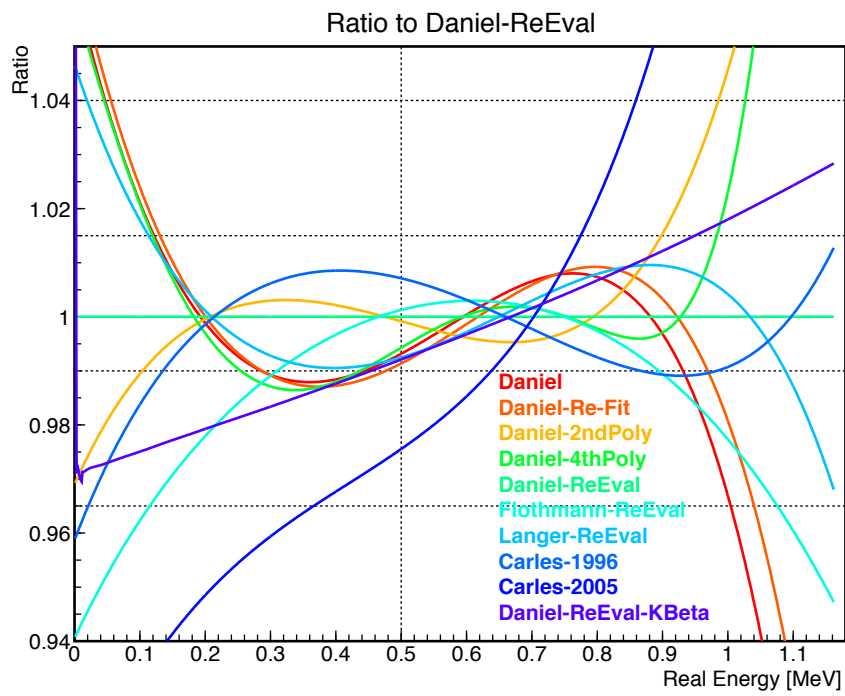
Figure A.4.: Comparison of ^{210}Bi spectra with different experimental shape factors.

Bibliography

Adelberger et al. Solar fusion cross sections. ii. the pp chain and cno cycles. *Reviews of Modern Physics*, 83(1):195–245, Apr. 12 2011.

Berger et al. The KamLAND full-volume calibration system. *Journal of Instrumentation*, 4:P04017, Apr. 27 2009.

Keefer. *FIRST OBSERVATION OF ^7BE SOLAR NEUTRINOS WITH KAMLAND*. PhD thesis, The University of Alabama, 2009.

Nakajima. *First Results from ^7Be Solar Neutrino Observation with KamLAND*. PhD thesis, Tohoku University, 2009.

Grant. *A MONTE CARLO APPROACH TO ^7BE SOLAR NEUTRINO ANALYSIS WITH KAMLAND*. PhD thesis, The University of Alabama, 2011.

Xu. Observation of ^{7}Be Solar Neutrinos with KamLAND. Master's thesis, Tohoku University, 2011.

NASA. Life Cycles of Stars. http://imagine.gsfc.nasa.gov/docs/teachers/lifecycles/LC_main_p8.html.

Basu and Antia. Helioseismology and solar abundances. *Physics Reports*, 457:217–283, Dec. 13 2008.

Serenelli, Haxton, and Penã-Garay. Solar models with accretion. i. application to the solar abundance problem. *Astrophysical Journal*, 743:24–43, Dec. 10 2011.

Serenelli, Basu, Ferguson, and Asplund. Ew solar composition: The problem with solar models revisited. *APJ*, 705:L123–L125, Oct. 6 2009.

Adelberger et al. Solar fusion cross sections. *Reviews of Modern Physics*, 70(4):1265–1291, Oct. 4 1998.

Angulo et al. A compilation of charged-particle induced thermonuclear reaction rates. *Nuclear Physics A*, 656:3–183, Feb. 2 1999.

Badnell et al. Updated opacities from the Opacity Project. *Monthly Notices of the Royal Astronomical Society*, 360:458–464, Mar. 1 2005.

Grevesse and Sauval. Standard solar composition. *Space Science Reviews*, 85:161–174, May 1 1998.

Asplund, Grevesse, Sauval, and Scott. The chemical composition of the sun. *Annual Review of Astronomy and Astrophysics*, 47:481–522, 2009.

Serenelli. Solar Models. http://www.ice.csic.es/personal/aldos/Solar_Models.html, 2013.

Stein. Bob Stein's Research Projects. http://www.pa.msu.edu/~steinr/research.html.

Trampedach et al. A grid of three-dimensional stellar atmosphere models of solar metallicity. i. general properties, granulation, and atmospheric expansion. *Astrophysical Journal*, 769(1):18–1–15, Mar. 6 2013.

VandenBerg et.al. M67: a constraint on Z_a and/or on diffusive processes in stellar interiors. *Memorie della Società Astronomica Italiana*, 79(2):759–761, 2008.

Asplund, Grevesse, and Sauval. The solar chemical composition. *Nuclear Physics A*, 777:1–4, Jun. 24 2005.

Pontecorvo. Mesonium and anti-mesonium. *Journal of Experimental and Theoretical Physics*, 6, 1957.

Maki, Nakagawa, and Sakata. Remarks on the unified model of elementary particles. *Progress of Theoretical Physics*, 28(5):870–880, Jun. 25 1962.

Gonzalez-Garcia. Neutrino masses and mixing: evidence and implications. *Reviews of Modern Physics*, 75:345–402, Mar. 26 2003.

Shi and Schramm. An update on the solar neutrino problem and the three-family msw effect allowing for astrophysical uncertainties. *Physics Letters B*, 283:305–312, Apr. 5 1992.

Beringer et al. and Particle Data Group. The review of particle physics. *Physical Review D*, 86:010001, 2013.

An et al. and Daya Bay Collaboration. Improved measurement of electron antineutrino disappearance at daya bay. *Chinese Physics C*, 37(1):011001–1–20, Nov. 15 2013.

Bahcall, Kamionkowski, and Sirlin. Solar neutrinos: Radiative corrections in neutrino-electron scattering experiments. *Physical Review D*, 51:6147–6158, Jun. 1 1995.

Carlos Pena-Garay and Aldo Serenelli. Solar neutrinos and the solar composition problem. 2008.

J. Hosaka et al. Solar neutrino measurements in super-Kamiokande-I. *Physical Review D*, 73:112001–1–33, Jun. 1 2006. doi: 10.1103/PhysRevD.73.112001.

J.P. Cravens et al. Solar neutrino measurements in Super-Kamiokande-II. *Physical Review D*, 78:032002–1–11, Aug. 6 2008. doi: 10.1103/PhysRevD.78.032002.

K. Abe et al. Solar neutrino results in Super-Kamiokande-III. *Physical Review D*, 83: 052010–1–19, Mar. 24 2011. doi: 10.1103/PhysRevD.83.052010.

Bellini et al. and Borexino Collaboration. Final results of borexino phase-i on low energy solar neutrino spectroscopy. *arXiv*, Aug. 2 2013.

Tajima. *Measurement of Electron Anti-Neutrino Oscillation Parameters with a Large Volume Liquid Scintillator Detector, KamLAND*. PhD thesis, Tohoku University, 2003.

Shimizu. *An Evidence for Spectral Distortion of Reactor Anti-Neutrinos and A Study of Three Flavor Neutrino Oscillation*. PhD thesis, Tohoku University, 2004.

Mitsui. Densities and Total Volumes of LS and BO. http://www.awa.tohoku.ac.jp/~mitsui/kamland_only/fill/final.html, Nov. 2002.

Winslow. *First Solar Neutrinos from KamLAND: A Measurement of the ^8B Solar Neutrino Flux*. PhD thesis, University of California, Berkeley, 2008.

Bolz and Tuve. *CRC handbook of tables for applied engineering science*. CRC Press, 1991.

Daniel. DAS β-SPEKTRUM DES RaE. *Nuclear Physics*, 31:293–307, Sep. 26 1961.

Carles and Malonda. Radionuclide standardization by cherenkov counting. *Applied Radiation and Isotopes*, 46(6):799–803, Jan. 18 1995.

Carles. Beta shapefactor determinations by the cutoff energy yield method. *Nuclear Instruments and Methods in Physics Research A*, 551:312–322, May. 16 2005.

Fujita, Yamada, Matumoto, and NAKAMURA. Parity nonconservation and the beta-spectrum of rae. *Progress of Theoretical Physics*, 20(3):287–307, Jun. 9 1958.

Kotani and Ross. The first forbidden β-decay. *Progress of Theoretical Physics*, 20(5): 643–689, Jul. 6 1958.

Zhang. *Precision Measurement of Neutrino Oscillation Parameters and Investigation of Nuclear Georeactor Hypothesis with KamLAND*. PhD thesis, California Institute of Technology, 2011.

Kozlov. The Krypton measurement system. In *KamLAND Collaboration Meeting*, 2010.

Kozlov. The Kr-85 activity in KamLAND LS. In *KamLAND Collaboration Meeting*, 2011.

Kozlov. The Ar-39 activity in KamLAND LS. In *KamLAND Hardware Meeting*, 2013.

Xu. Pileup Reconstruction. http://www.awa.tohoku.ac.jp/KamLAND/internal/analysis/Be7SolarNeutrino/reference/twinEvents.pdf, Jul. 25 2013a.

Xu. Measurement of Kr-85 Concentration by Pileup at KamLAND. In *2013 Fall Meeting of Japanese Physics Society*, 2013b.

Abe et al. and KamLAND Collaboration. Production of radioactive isotopes through cosmic muon spallation in KamLAND. *Physical Review C*, 81:025807, Feb. 23 2010.

Hagner et al. Muon-induced production of radioactive isotopes in scintillation detectors. *Astroparticle Physics*, 14:33–47, Nov. 17 1999.

Behrens and Jänecke. *Landolt-Börnstein - Group I Elementary Particles, Nuclei and Atoms Numerical Data and Functional Relationships in Science and Technology Volume 4: Numerical Tables for Beta-Decay and Electron Capture.* Springer-Verlag, 1969.

Konopinski and Uhlenbeck. On the Fermi Theory of β-RadioActivity II The "Forbidden" Spectra. *Physical Review*, 60:308–321, Jun. 24 1941.

Konopinski. *The Theory of Beta Radioactivity.* Oxford at the Clarendon Press, 1966.

Rose and Konopinski. *Alpha-, Beta- and Gamma-Ray Spectroscopy.* North-Holland Publishing Company, Amsterdam, 1965.

Dzhelepov and Zyrianova. *Vlianie elektriceskovo polja atoma na beta-raspad (The influence of the Atomic Electron Field on the β Decay).* Akademii Nauk SSSR, Moscow, 1956.

Bühring. Beta decay theory using exact electron radial wave functions. *Nuclear Physics*, 61:110–128, Jun. 2 1965.

Behrens and Bühring. *Electron Radial Wave Functions and Nuclear Beta-decay.* Clarendon Press, Oxford, 1982.

Plassmann and Langer. Beta spectrum of radium e. *Physical Review*, 96(6):1593–1598, Dec. 5 1954.

Frothmann and Wiesner and Löhken and Rebel. β-Spektroskopie mit Halbleiterdetektoren beim Zerfall von ^{32}P, ^{49}Sc, ^{204}Tl und ^{210}Bi (β-Spectroscopy of ^{32}P, ^{49}Sc, ^{204}Tl and ^{210}Bi using Solid State Detectors) . *Zeitschrift für Physik*, 225:164–194, Apr. 14 1969.

Behrens and Szybisz. *Shapes of beta spectra*, volume 6-1 of *Physics data / Physik Daten*. ZEAD, 1976.